Using Cepheid Variable Pulsation Properties to Trace Galaxy Age and Metallicity

Lawrence Antony Short

A thesis submitted in partial fulfilment of the requirements of

Liverpool John Moores University

for the degree of

Doctor of Philosophy.

December 2019

Declaration

The work presented in this thesis was carried out at the Astrophysics Research Institute, Liverpool John Moores University. Unless otherwise stated, it is the original work of the author.

While registered as a candidate for the degree of Doctor of Philosophy, for which submission is now made, the author has not been registered as a candidate for any other award. This thesis has not been submitted in whole, or in part, for any other degree.

Lawrence Antony Short

Astrophysics Research Institute

Liverpool John Moores University

IC2, Liverpool Science Park

146 Brownlow Hill

Liverpool L3 5RF

United Kingdom

JUNE 25, 2020

Abstract

Cepheid variable stars have long been used as distance indicators due to their strong period-luminosity relation. However, the period of a Cepheid is affected by its metallicity so any difference in metal-content between calibration Cepheids and Cepheids being used for distance measure would lead to a systematic error in the distance calculated. Metallicity measurements are traditionally achieved by spectroscopic analysis but this can lead to considerable uncertainties. Therefore, the first part of this thesis looks at using double-mode, or beat, Cepheids to measure metallicity. Specifically, to measure the metallicity gradient across the Triangulum galaxy, M33. Beat Cepheids can be used to trace metallicity because their period ratio is sensitive to metal abundance which is well described by pulsation models.

To find variable stars, image subtraction techniques are applied to observations of two separate datasets of M33. PSF fitting photometry is carried out on the data to produce calibrated light curves. The is also done to cross-calibrate the two datasets but an amplitude discrepancy arises in many of the Cepheid light curves. This amplitude problem is not caused by mismatching of the stars between the datasets, via either pixel matching or WCS coordinate transform. Nor is there any correlation with the Cepheid position in M33. Further investigation, beyond the scope of this thesis, into this issue is required.

The amplitudes are corrected using a scaling factor so that an Analysis of Variance routine can be applied on the light curves to find Cepheid periods. Cepheids are only kept if the ratio between their two strongest periods lies within an appropriate range. 3 beat Cepheids are found, on top of another 5 already known beat Cepheids, in M33. The metallicities of the beat Cepheids are determined by comparing the period ratios with beat Cepheids of known metallicity in the Milky Way and Magellanic Clouds. The galactocentric distances of the stars are determined by deprojecting their celestial coordinates with M33's inclination and position angles along with the distance. Therefore, the metallicity of M33 as a function of radius can be immediately obtained, yielding the metallicity gradient across the galaxy. Using this method the metallicity gradient of M33 is found to be steeper than measurements made by recent spectroscopic analysis of HII regions. This is more in line with what is expected from recent work deriving the Cepheid Period-Luminosity relation for M33.

There exists a period-age relation for Cepheid variable stars. The second part of the thesis aims to derive this empirically using observations of 6 stellar clusters in the Large Magellanic Cloud. The age for each cluster is taken from literature and were determined by Isochrone fitting. The same image subtraction techniques as used on the M33 data are used to find Cepheids and their periods in the LMC clusters. Cepheids are only considered to be cluster members if they fall within the half-light radius of the cluster and have proper motions matching their host cluster. The mean periods of the Cepheids in each cluster along with the cluster ages is then used to derive the period-age relation.

The period-age relation derived here shows a steeper gradient than those produced by models or previous empirical derivations. There is a large spread in periods of the Cepheids in any given cluster that increases inversely with cluster age. This effect cannot be replicated if the cluster's population is recreated with a single stellar model.

However, the period spread can be described using stellar models of multiple initial rotation rates.

Acknowledgements

This work has made use of observations made with the Isaac Newton Telescope (INT) operated on La Palma by the Isaac Newton Group at the Observatorio del Roque de los Muchachos of the Instituto de Astrofsica de Canarias. As well as observations made with MegaPrime/MegaCam, a joint project of the Canada-France-Hawaii Telescope (CFHT) and CEA/DAPNIA, which is operated by the National Research Council of Canada, the Institute National des Sciences de l'Univers of the Centre National de la Recherche Scientifique of France, and the University of Hawaii. Plus further observations made with the 2m Faulkes Telescope South at the Siding Spring node of the Las Cumbres Observatory in New South Wales, Australia. Initial capital and operational funding for the Faulkes Telescope South was provided by The Dill Faulkes Educational Trust. Faulkes Telescope South is now operated by Las Cumbres Observatory as a component of the Las Cumbres Observatory Global Telescope Network.

This work has made use of data from the European Space Agency (ESA) mission *Gaia* (`https://www.cosmos.esa.int/gaia`), processed by the *Gaia* Data Processing and Analysis Consortium (DPAC, `https://www.cosmos.esa.int/web/gaia/dpac/consortium`). Funding for DPAC has been provided by national institutions, mainly institutions participating in the *Gaia* Multilateral Agreement.

This work has made use of IRAF (Image Reduction and Analysis Facility). IRAF is

distributed by the National Optical Astronomy Observatories, which are operated by the Association of Universities for Research in Astronomy, Inc., under cooperative agreement with the National Science Foundation.

This research was supported by a studentship awarded jointly by the Science and Technology Facilities Council (STFC) and Liverpool John Moores University (LJMU).

“Hello, World!”

- Anonymous

Contents

List of Tables

List of Figures

Chapter 1

Introduction

1.1 Stars as Distance Indicators

Humanity has long looked up to the stars and wondered of our place in the Universe. For millennia a geocentric model was accepted with the Sun and planets orbiting the Earth. As telescopes improved with the advancement of lens manufacture, Galileo Galilei could begin to observe the Solar System and Galaxy in much greater detail. However, measuring the scale of our corner of the Galaxy remained elusive.

1.1.1 Stellar Parallax

During the Earth's orbit of the Sun nearby stars seem to follow a similar elliptical orbit while the more distant background stars appear to be fixed in place. Taking two measurements 6 months apart gives a baseline of 2 astronomical units (AU), where 1 AU is the average distance between the Earth and the Sun, making it possible to measure the angle, θ, that the star has appeared to move on the sky. This is twice the parallax angle and is inversely proportional to the distance to the star. Therefore, it

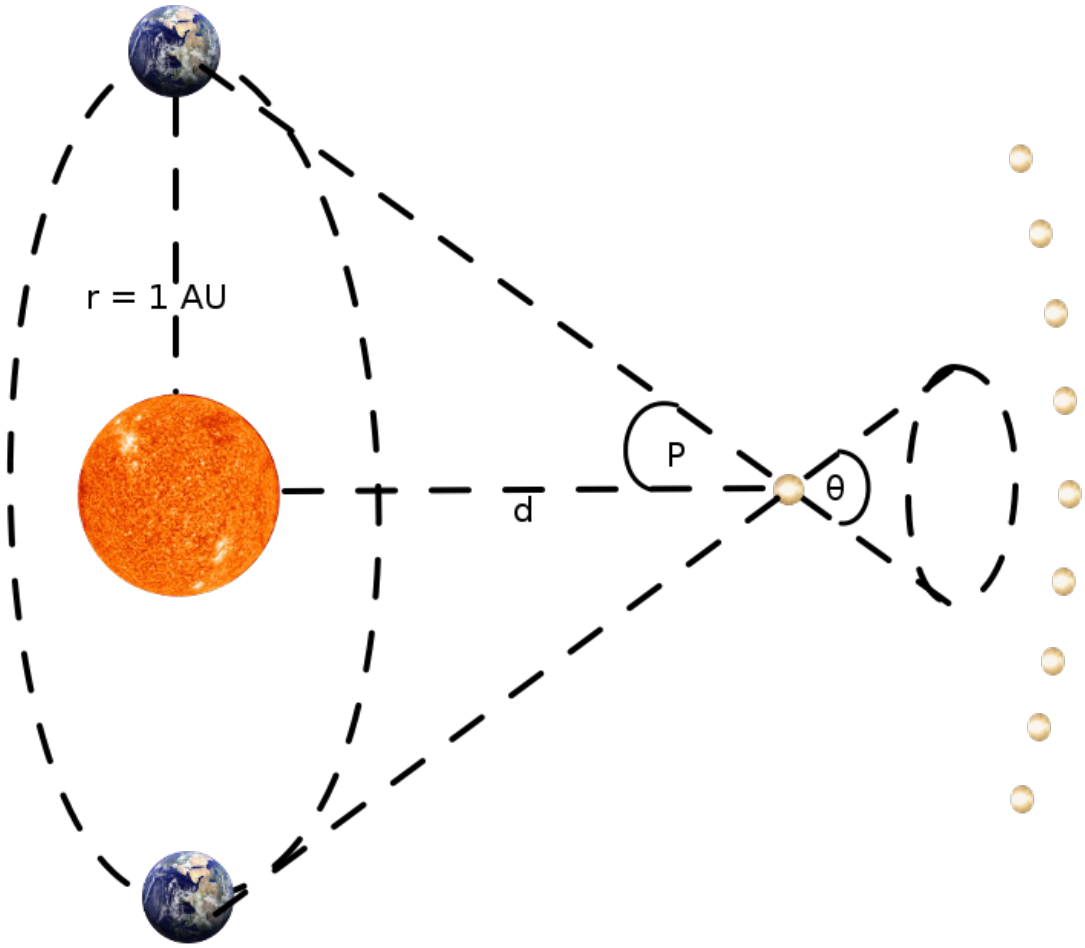

Figure 1.1: Determining stellar distance by trigonometric parallax. Where AU stands for astronomical unit and 1 AU is the distance from the Earth to the Sun. Produced for this thesis.

becomes a basic trigonometric problem as shown in Figure 1.1. Setting the distance between the Earth and Sun, r, to 1 AU, measuring the parallax angle, p, in units of arcseconds, as well as taking into account the small angle approximation, the distance to the star in question, d, is yielded in parsecs (pc) as in Equation 1.1. Where 1 parsec is the distance to a would be object with a parallax angle of 1 arcsecond (1”).

$$d = \frac{r}{\tan(\frac{\theta}{2})} \rightarrow \frac{1}{p} \tag{1.1}$$

Before parallax measurements could be made the distance to the Sun needed to be

accurately determined. In the early 18th century Edmond Halley surmised that by observing the transit of Venus across the Sun one could infer the size of the Solar System but Halley died well before the next transit of Venus was due to take place. The 1760's saw Venus transit the Sun twice leading to a global concerted effort to observe the transits from multiple locations around the world which allowed Jerome Lalande to determine a precise distance to the Sun. This meant that it would now be possible to measure the parallax angle of another star. Then in the following century breakthrough came when the first ever measurement of stellar parallax was conducted by Friedrich Bessel (1838) who successfully determined the distance to the nearby star 61 Cygni. However, ground-based parallax measurements are realistically limited to a precision of $\sim$0.01", even in good seeing conditions, limiting distance measurements to a few tens of pc. To increase precision, space-based measurements are needed.

Hipparcos

The $Hipparcos$ mission was launched by ESA in 1989 and until its termination in 1993 it measured precise positions and parallaxes of over a hundred thousand stars. $Hipparcos$ was able to measure down to a precision of a few milli-arcseconds meaning that distances of several hundred pc could be determined (ESA, 1997). The first release of $Hipparcos$ data also included trigonometric parallaxes for 223 classical Cepheids variables within the Galaxy (Feast and Catchpole, 1997). These measurements were used to calibrate the zero-point of the Cepheid Period-Luminosity (PL) relation which allows for distance measurements of tens of Mpc. The Cepheid Period-Luminosity relation or Leavitt Law is discussed in chapter section 1.1.2.

Gaia

ESA's follow-up to $Hipparcos$ is the $Gaia$ mission which was launched in December 2013 ($Gaia$ Collaboration et al., 2016). $Gaia$ is able to measure positions and parallaxes with a precision between 10 and 100 μarcseconds leading to distances up to ten thousand parsecs ($Gaia$ Collaboration et al., 2018). Due to the fact that $Gaia$ surveys the entire sky as well as possessing excellent astrometric precision it is able to measure positions and velocities of stars not only in the Milky Way but also in nearby galaxies such as the Magellanic Clouds meaning that cluster membership of Magellanic Cloud Cepheids could be determined from the $Gaia$ data releases, this will be discussed in detail chapter section 4.4.

However, parallax measurements are limited to distances in our Galaxy even with the most accurate astrometric methods available today. In order to measure to greater distances another method was needed. This came in the form of the correlation between the period and luminosity of Cepheid variable stars.

1.1.2 The Leavitt Law

Henrietta Leavitt (1908) had been given the task of finding variable stars[1] whilst working as a 'Computer' at the Harvard College Observatory. The 'Harvard Computers' were a group of women hired by the Harvard College Director, Edward Pickering, to analyse large quantities of astronomical data, many of whom went on to publish significant findings and make important contributions to the field of astronomy (Sobel, 2018). To find the variable stars Leavitt used a 'blink comparator' which rapidly flashes between two images causing any objects that vary in magnitude to appear as

[1] A variable star is a star whose brightness or magnitude increases and decreases on a regular period of time that can easily be measured, hence the name variable.

'blinking' points. Leavitt identified several thousand of these objects and started to wonder if there was a relationship between the length of the period and the luminosity, which is the star's intrinsic brightness or its absolute magnitude (M). Unfortunately it is not possible to tell the absolute magnitude of a star just by looking. Instead only the apparent magnitude (m), how bright an object seems to someone observing, can be determined. In order to calculate the distance to an object something called the 'distance modulus', μ, is used. This is how distance d, in parsecs, to an object is measured by calculating the difference between the apparent magnitude and absolute magnitude of a celestial object as in Equation 1.2.

$$\mu = m - M = 5\log_{10}(d) - 5 \tag{1.2}$$

For this reason Leavitt looked at a specific type of variable star called a Cepheid that inhabited the Small Magellanic Cloud (SMC) as all of its stars are roughly at the same distance. She then plotted the apparent magnitude of 25 Cepheid Variables against the logarithm of the length of their period, as shown in Figure 1.2, and found a linear relation that is known as the period-magnitude or period-luminosity (PL) relation but is now commonly referred to as the 'Leavitt Law' (LL) (Leavitt and Pickering, 1912). The absolute magnitude of Galactic Cepheid variables was known, so by assuming this value was universal, a method of calibrating the distance to any population containing a Cepheid variable had been found by using the distance modulus equation.

Type Ia Supernova Calibration

In order to measure out to even further distances standard candles brighter than Cepheids are required. This is where Type Ia Supernovae (SNe) enter the picture as they are bright enough that they can be observed at distances of Gpc and the maximum lumi-

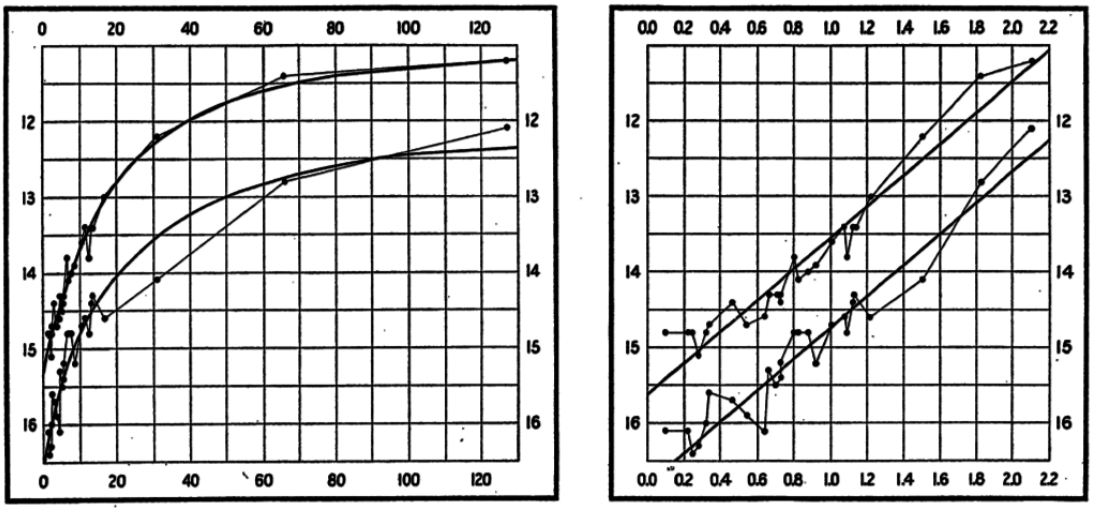

Figure 1.2: Small Magellanic Cloud (SMC) Cepheid period-magnitude relation taken from the paper by Leavitt and Pickering (1912), the panel on the left shows the apparent magnitude on the y-axis with the period of the Cepheids in days on the x-axis and the panel to the right has the same y-axis but the x-axis shows the logarithm of the period.

nosity of their light curves was thought to be ubiquitous. However, it was found that not all SNe reach the same peak brightness but a correction can be applied so that they can be used as standard candles. This is known as the Phillips (1993) relation which is determined from the rate of decline of SNe Ia light curves. Furthermore, for them to be useful they need to be calibrated. This is achieved by observing SNe in relatively nearby galaxies that also contain observable Cepheids so that their distance modulus (eq. 1.2) is known from the Leavitt Law (Sandage et al., 1992).

So far only a snapshot of distance measurement astronomy has been presented, the following section briefly introduces a few other methods. Figure 1.3 shows how these different methods are related and where Cepheids fit in.

1.1.3 Cosmological Distance Ladder

Hertzsprung-Russell Diagram

The main tool for studying stars is the Hertzsprung-Russell Diagram (HRD) or Colour-Magnitude Diagram (CMD), where the effective surface temperature (T_{eff}) or colour of a star is plotted against its luminosity or absolute magnitude. Stars of different types (i.e. stars in different evolutionary stages due to age or mass) each occupy special regions on a HRD or CMD. An array of a star's characteristics, its mass, structure, spectral class etc. can be understood by identifying the position of a star on these diagrams. One of the key regions on is the main-sequence[2] (MS) which can be fitted with isochrones[3] in order to infer their distance modulus (eq. 1.2). Another useful position is the tip of the red giant branch[4] (TRGB) as it has been found that the absolute bolometric magnitude[5] varies by only $\sim$0.1 magnitudes independent of age and chemical composition (Lee et al., 1993; Salaris and Cassisi, 1997).

Variable Star Methods

As well as Cepheids other types of variable star exhibit a PL relation such as RR Lyrae (RRL) and Mira variables, variable stars will be discussed in more detail in section 1.2. The PL relation is not the only way to infer distances from variable stars. Another method was developed by Walter Baade (1926) and Adriaan Wesselink (1946), they showed that from the magnitude changes of a Cepheid due to its pulsation, it is possible to obtain the change in the star's diameter. The Baade-Wesselink method[6] relies on the fact that variable stars physically expand and contract over the course of their pulsation

[2]Core Hydrogen burning stars.
[3]Modelled curves on the HRD showing a population of stars at a constant age and composition.
[4]The brightest point on the red giant branch marking the onset of Helium fusion in the core.
[5]The magnitude of the star taking into account electromagnetic radiation at all wavelengths.
[6]Sometimes referred to as the 'pulsation parallax'.

period. This means that not only does the star's brightness change but also its radial velocity, which can be measured via spectroscopic methods allowing for the star's radius to be determined. This is achieved by calculating the change in radius from the time integration of its velocity curve and fractional radial changes from periodic variations in the star's spectrum and brightness (Di Benedetto, 1997). The spectrum also yields the effective temperature of the star therefore its luminosity is obtained as:

$$L = 4\pi R^2 \sigma T_{eff}^4 \tag{1.3}$$

where σ is the Stefan-Boltzman constant[7]. The luminosity is related to absolute magnitude and the star's apparent magnitude is determined from the flux (F) measured from Earth. It is possible to estimate a direct distance from these two measurements via:

$$d = \sqrt{\frac{L}{4\pi F}}. \tag{1.4}$$

Galaxies

Distant galaxies in which individual stars cannot be resolved can also be used for distance measurement. If a distant galaxy is observed with a certain angular resolution and split into even resolution elements, each section would contain an average number of unresolved stars with an average luminosity. However, each resolution element will not actually contain the same number of stars so Poisson fluctuations occur in the flux measurements of each section across a galaxy. These surface brightness fluctuations (SBF) scale inversely with distance and so the more distant a galaxy the smoother it appears to be (Tonry and Schneider, 1988). The Tully-Fisher relationship uses the properties of a spiral galaxy in order to estimate its distance. The main idea being that

[7] $\sigma = 5.67 \times 10^{-8} W m^{-2} K^{-4}$

as galaxies are self-gravitating systems they would follow the virial theorem. In this scenario that means that the more mass in a system i.e. the more massive a galaxy, the faster the stars would orbit its galactic centre. The higher a star's velocity the larger the width of its spectral lines, therefore, a direct link between spectral line width and virial mass can be made. The other key assumption is that the luminosity of a galaxy scales with mass. Once the luminosity of a galaxy is determined the distance can be inferred as with previous methods (Tully and Fisher, 2009). However, both of these approaches are very much reliant on local distance calibration i.e. via the Leavitt Law.

The Hubble Constant

The ultimate goal of distance measurement is to understand the true scale and age of the Universe. Edwin Hubble (1929) set the ball rolling by discovering that galactic distances are related to their recession velocities inasmuch as the further away a galaxy is the faster it is moving away from us. By plotting the distance to other galaxies in the Local Group and beyond (determined from Cepheids) against velocity measurements Hubble calculated an expansion rate for the Universe in units of velocity per distance, now referred to as the Hubble constant (H_0). Therefore, the inverse of H_0 is in units of time and is known as the Hubble time, or age of the Universe. Since then, great efforts have been made to improve upon the value of H_0. The most recent and probably most famous attempts were made by NASA's *WMAP*[8] (Komatsu et al., 2011) and the ESA's $Planck$ mission (The $Planck$ Collaboration, 2006), whose chief objectives were to observe properties of the Cosmic Microwave Background[9] (CMB) in order to reduce the uncertainty on H_0. One way is the Sunyaev-Zel'dovich (SZ) effect, in which a fraction of CMB photons are scattered by high-energy gas in galaxy clusters causing a

[8] Wilkinson Microwave Anisotropy Probe

[9] The now cooled remnant of the first radiation that could travel freely about the Universe.

shift in their wavelength (Zeldovich and Sunyaev, 1969). As well as the gravitational lensing of CMB photons by massive structures as predicted by Albert Einstein's (1915) theory of general relativity.

The Hubble Constant Discrepancy

There exists an open problem in Astrophysics in that there is a stark difference between the measurements of H_0 from different methods. With measurements of the CMB using the methods discussed in the previous paragraph within the context of ΛCMB cosmology, the latest value of the rate of expansion of the Universe from the Planck Collaboration et al. (2018) is H_0 = 67.4 $\pm$ 0.5 Km s^{-1} Mpc^{-1}. However, using a method involving 19 Cepheid calibrated SNe Ia host galaxies Riess et al. (2016) measured a value for H_0 at 73.24 $\pm$ 1.74 Km s^{-1} Mpc^{-1}. The error bars on the values from these two methods do not overlap, presenting a difference at a level greater than 3σ. This discrepancy could be down to unforeseen systematic errors or some unknown physics (Freedman, 2017), in any case this remains a fascinating area for research.

Even these final rungs of the cosmological distance ladder need to be calibrated. This is why having an accurate Leavitt Law that takes into account all variables is so important. Every step on the ladder is fortified by the previous one, although now it is more like a climbing frame with multiple connections stretching between different methods of measuring distance to various astrophysical phenomena. The calibration link between the distance tracers is presented in Figure 1.3.

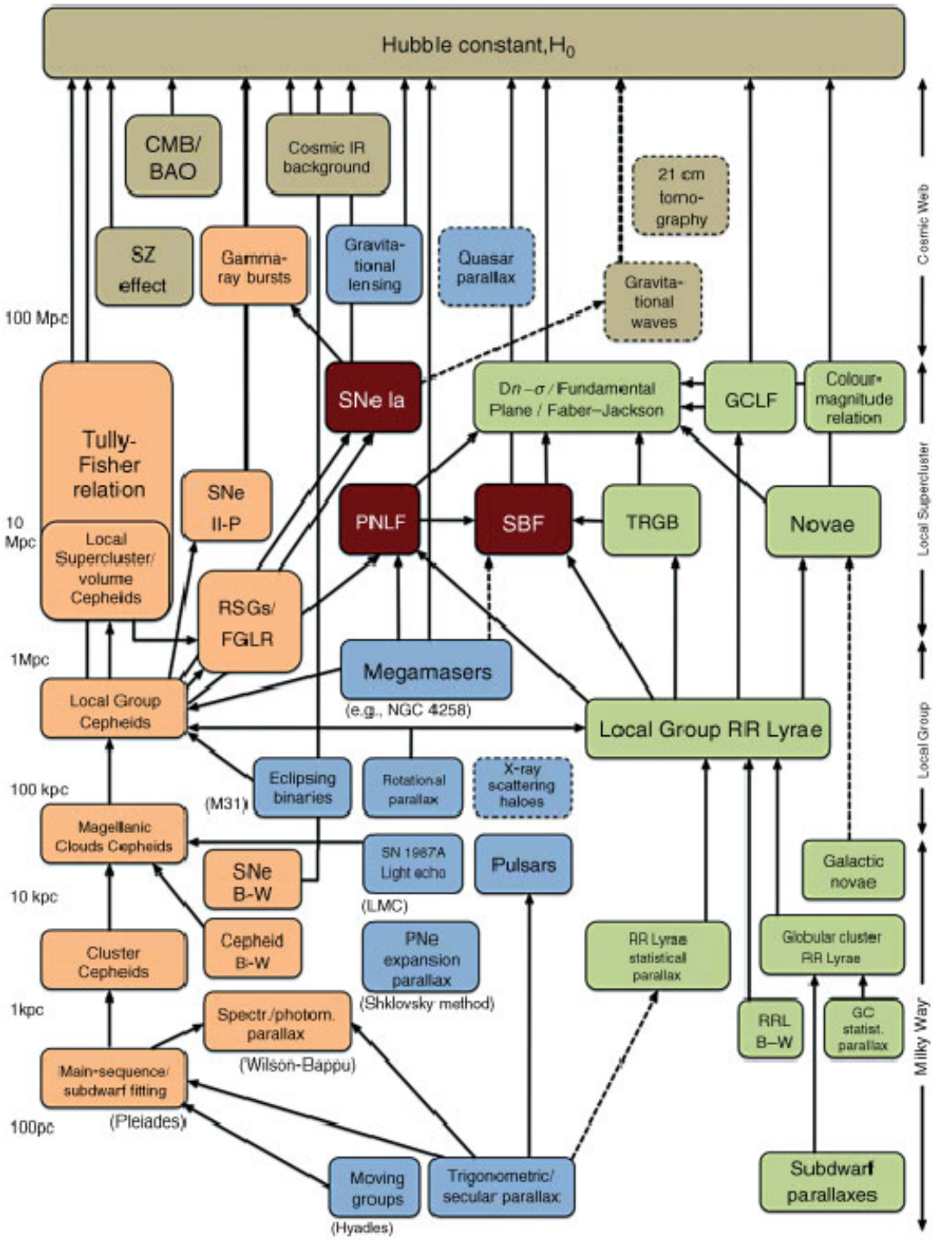

Figure 1.3: Cosmological distance ladder taken from de Grijs (2011). A schematic showing the most effective method of measurement at each distance bin. The yellow boxes to the left show methods based on young (Population I) stars, with boxes highlighted green to the right for older (Population II) stars and deep red boxes between that use both. The blue boxes up through the middle represent geometric methods and the light brown at the top are not directly linked to stellar populations.

1.2 Variable Stars

1.2.1 Why do Stars Pulsate?

Arthur Eddington (1917, 1918) was the first to propose pulsation theory. Typically a compression of the stellar envelope leads to an increase in density and temperature causing a decrease in opacity so that heat energy escapes at a greater rate allowing the star to remain in equilibrium. However, this does not happen with variable stars. Instead, during a compression phase there is an increase in opacity of the stellar envelope blocking the release of energy, this is occurs near the surface, in the Helium and Hydrogen ionization zones. Eventually, enough pressure is built up that the envelope is pushed out and then decreases in opacity which starts the cycle all over again. This driving force behind the pulsation that leads to periodic changes in luminosity is known as the 'κ-mechanism' where the kappa (κ) represents radiative opacity.

1.2.2 The Instability Strip

Variable stars lie in a narrow region on the HRD called the instability strip (IS) where stars become pulsationally unstable. Towards the blue side of the IS the amount of material in the stellar envelope above the ionization zones decreases until there is no longer enough mass to significantly drive pulsations, this defines the hot blue edge of the IS (Baker and Kippenhahn, 1962, 1965). As the effective temperature decreases, envelope convection begins stopping the mechanism from efficiently driving pulsation giving rise to the cooler red edge of the IS (Deupree, 1977).

1.2.3 Cepheid Variable Stars

Cepheid variable stars are mainly split into two groups, the younger Population I Cepheids (Type I) and the older Population II Cepheids (Type II).

Type I

Type I, or classical, Cepheids typically have a period range of 1-50 days but some longer period Cepheids have been observed. They are very bright evolved B-stars going through the phase of core Helium burning and considered to be of the intermediate mass range covering $\sim$4-12 solar masses. As they evolve away from the RGB they can experience several blue loops (but usually just one) causing them to pass through the IS at least twice. Pretty much all observed classical Cepheids will be in this blue loop phase, however, all stars actually pass through the IS as they expand to the base of the RGB when their core Hydrogen has been exhausted. This first crossing of the IS is extremely rapid, so it would be highly unlikely to catch a star pulsating during this stage of evolution.

When the Hydrogen burning in the core ceases, an inert Helium-core is left behind and Hydrogen burning moves to the shell. Hydrogen-shell burning becomes narrower and narrower and fresh Helium is supplied to the shell causing the hydrostatic equilibrium to be lost and the core begins to contract. While the Helium core contracts, the star's shell expands and cools as the star shoots through the instability strip, on its first crossing, this is known as the sub-giant-branch (SGB) phase. Eventually, the outer convective envelope of the star reaches deeper into the star's interior and the transport of energy from the remaining narrow band of Hydrogen-shell burning to the star's surface increases. This causes the luminosity of the star to increase and it climbs the RGB. At the tip of the RGB the Helium-core has contracted enough to ignite. At the

onset of the Helium burning the star's luminosity decreases slightly before the temperature begins to increase and the star moves blueward through the instability strip for the second time. The star will reach a temperature limit and, with most of the core-Helium exhausted, the star will cool again passing through the instability strip for the third time. This describes the process of the three instability strip crossings for type I Cepheids.

The main factor dictating the pulsation properties of a Cepheid is the size of the Helium-core. This can be affected by several different physical mechanisms such as mixing-processes, opacity, stellar rotation and mass-loss. One of the mixing-processes is known as convective core overshooting where during the MS Hydrogen-core burning, material from the shell is mixed into the core. This causes the core to be larger than it would be at the end of the MS lifetime if no overshooting had taken place. Events referred to as dredge-up phases occur during the RGB phase in which processed material is carried from the core to the surface. The first-dredge up happens at the base of the RGB when the convective zone deepens and a second occurs later after the blue loop. The amount of material dredged-up alters the size of the core and changes the chemical composition at the surface, changing the opacity. The opacity of a star is dictated by the distribution of iron-group elements and determines the limits of the instability strip (Bono et al., 2000; Salmon et al., 2012). Stellar rotation causes the MS lifetime to increase because the mixing process supplies the core with fresh Hydrogen during the core Hydrogen burning phase. Therefore, at a given age there will be a spread in Cepheid periods because stars that were rotating would be more massive than those that were not. As stellar rotation affects the relationship between a Cepheid's period and age this issue is discussed in more detail in Chapter 4. Strong stellar winds can cause some intermediate and high mass stars to experience significant mass-loss. This affects the size of the star and therefore its evolutionary path altering the luminosity

and temperature at which it crosses the instability strip, changing its pulsation.

Type II

Type II Cepheids are old ($\sim 10Gyr$), low mass ($< 1M_{\odot}$) metal-poor stars with pulsation periods similar to those of there Type I counterparts. They were once Horizontal Branch (HB) stars but they no longer burn Helium in their cores and have evolved to a region of the HRD slightly brighter than RRL, see Figure 1.4.

Anomalous Cepheids

There also exists a mysterious form of variable star bearing the title of Cepheid, the anomalous Cepheid. They generally have shorter periods than other Cepheids ($\sim$0.3-2 days) and cross the IS at a luminosity brighter than that of RRL. Like Type II Cepheids they have similar metal-content to that of RRL but unlike Type II Cepheids they are of larger mass (Caputo et al., 2004).

For the purposes of this thesis only classical (Type I) Cepheids are important as both Type II and anomalous Cepheids are too faint to be seen in M33 and too old to be present in the Large Magellanic Cloud (LMC) clusters being used.

1.2.4 Pulsation Modes

Fundamental

In the fundamental case a single node is present in the in the centre of the star causing a single pulsation to occur through the Cepheid's shell. Fundamental light curves typically show a sawtooth like shape.

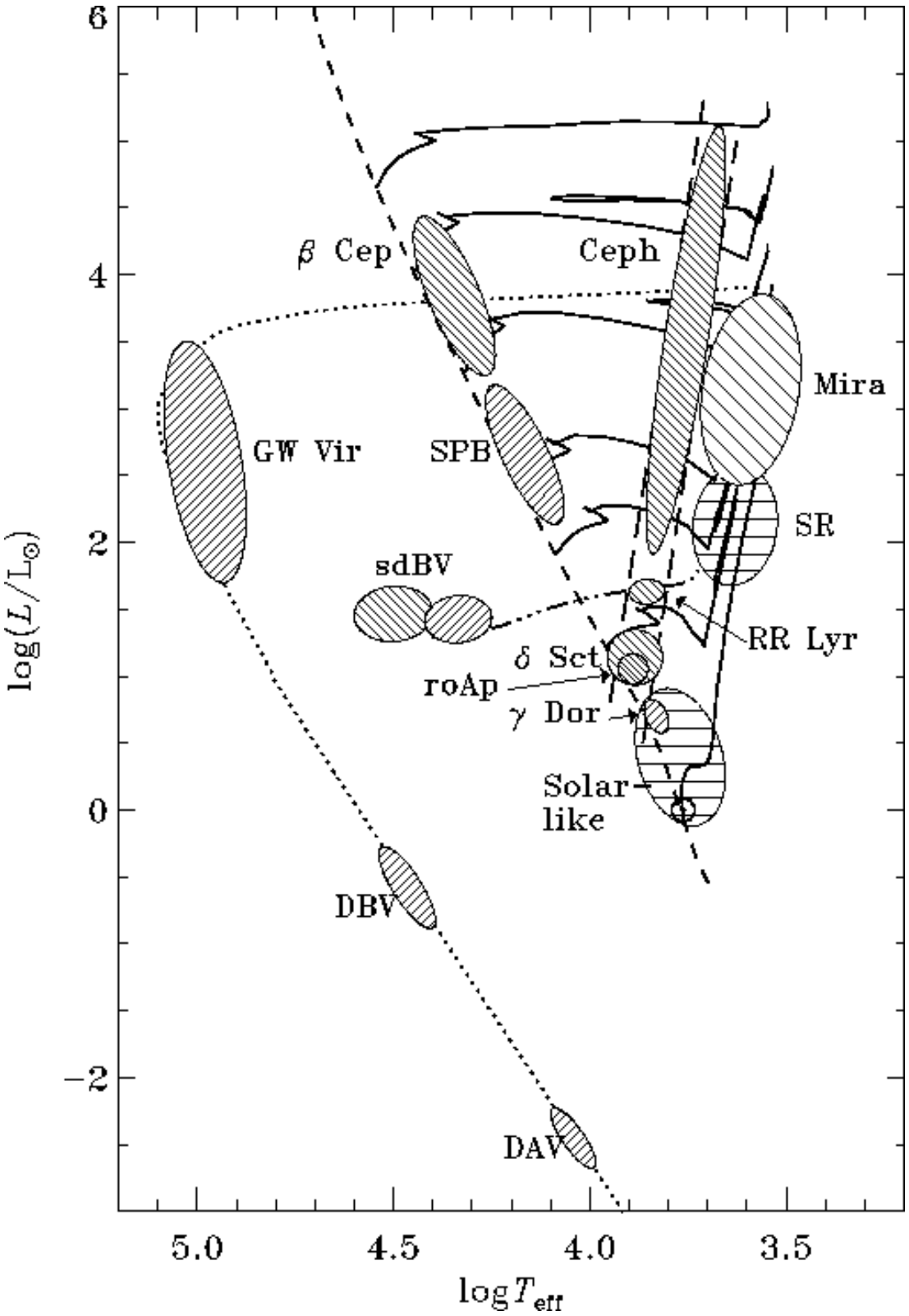

Figure 1.4: Hertzsprung-Russell Diagram showing the position of the IS and the areas where different types of variable star lie, see text for details. Taken from Christensen-Dalsgaard (1998).

Hertzsprung progression

The shape of the fundamental mode light curves is affected by the pulsation period as can be seen in Figure 1.5 by the presence of a bump moving along the curves as the period is increased see. This is known as the Hertzsprung progression.

Overtone

Towards the hotter blue edge of the IS multiple ionisation zones can start to appear within the star's shell. This can cause multiple nodes to occur leading to shorter sinusoidal overtone pulsations. A range of SMC first (1O) and second (2O) overtone mode Cepheid light curves (Soszyński et al., 2010) can be seen in Figure 1.6.

Beat Cepheids

The topology of the IS is determined by the mode of pulsation of the variables. Cepheid variable stars typically have two modes of pulsation being either fundamental (P_0) or first overtone (P_1) but there also exists a third much rarer kind of variable that pulsate in the second overtone mode. Fundamental pulsators inhabit the red side of the IS with the first and second overtones towards the blue side. Sections separating the different types of pulsator in the IS are blurred and in the transition places variable stars pulsating in dual modes are found. Cepheids have been found that pulsate simultaneously in the fundamental and first overtone modes as well as those that pulsate in both the first and second overtones, these double-mode Cepheid variables are also known as 'Beat Cepheids'. The period ratios between the two different pulsation modes in beat Cepheids can be used to study different stellar parameters. For an example of a beat Cepheid's light curve folded by its two distinct periods see Figure 1.7.

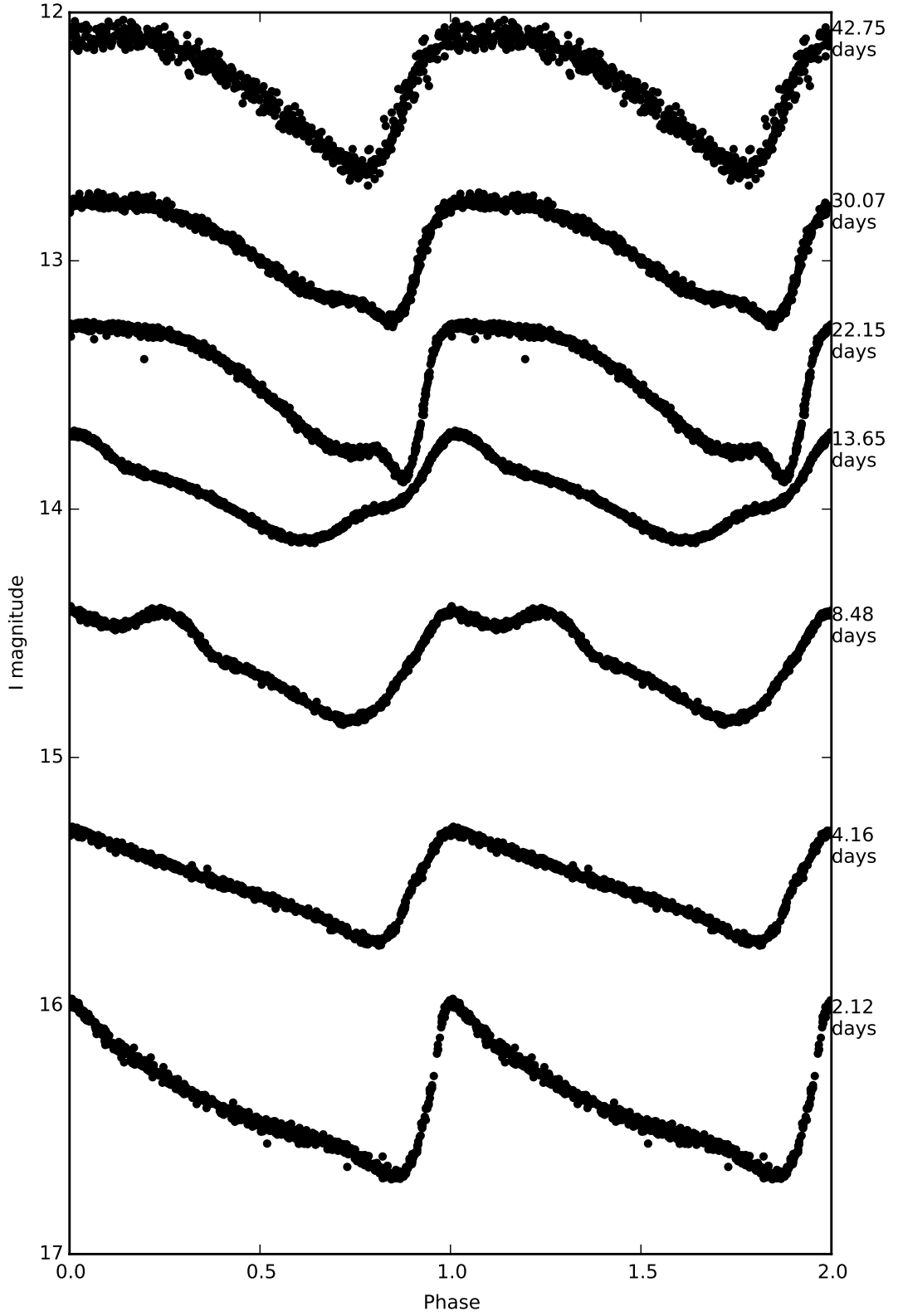

Figure 1.5: Light curves of classical Cepheid variable stars pulsating in the Fundamental mode with increasing periods (indicated to the right of the figure). The Hertzsprung progression can be seen in the light curves with periods of 8.48 days and above. The data is for OGLE-III Cepheids in the SMC by Soszyński et al. (2010)

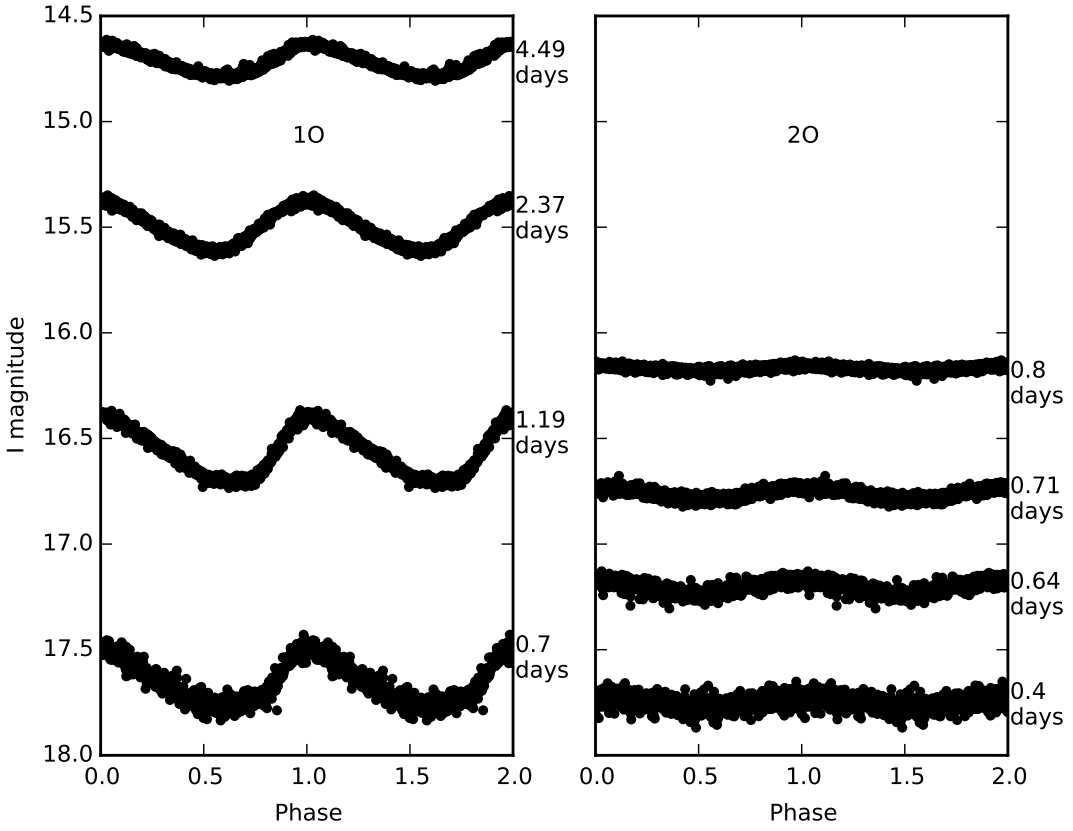

Figure 1.6: Light curves of classical Cepheid variable stars pulsating in the first and second Overtones. The right-hand panel shows the first overtone (1O) Cepheids and the left-hand panel shows the second overtone (2O) pulsators with periods indicated on the right of each panel. The data is for OGLE-III Cepheids in the SMC from Soszyński et al. (2010)

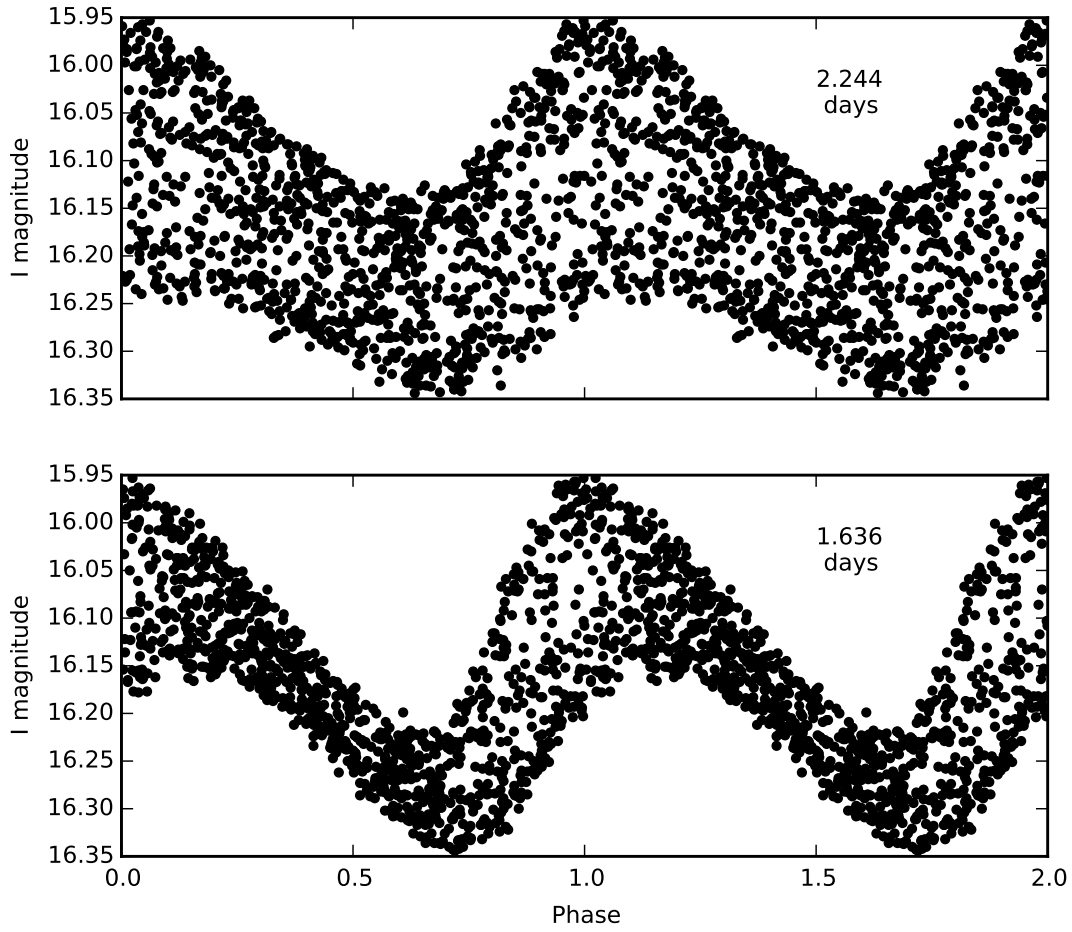

Figure 1.7: Light curve of a Cepheid variable star pulsating in two modes simultaneously split into component periods. The fundamental component in the upper panel and first overtone underneath. The periods are indicated by each light curve. The data is for OGLE-III Cepheids in the SMC from Soszyński et al. (2010)

1.3 Variable Stars as Tools for Astronomy

Metallicity Dependence

Pulsation properties are affected by the chemical composition of a star. This is defined by three parameters, the Hydrogen mass fraction, X, the Helium mass fraction, Y, with the third parameter, Z, representing the proportion of all the heavier elements present which in astronomy are grouped together as metals, where X+Y+Z=1. The metal-content is also known as the metallicity of a star. If the period of a Cepheid is affected by metallicity and the metal-content of Cepheids being used in a PL distance measurement differ from calibrating Cepheids then there exists a systematic error in the distance determination. Scowcroft et al. (2009) found a discrepancy in the calculated distance moduli from the Leavitt Law in Cepheids in different parts of the Triangulum galaxy, M33. This was deemed to be due to there being a steep metallicity gradient across M33.

Figure 1.8 shows the discrepancy in the zero-points of the Leavitt Laws from two different regions of M33, deemed to be caused by the Cepheids in the inner field of M33 having a much higher metallicity than those in the outer field. This suggests that a Cepheid's pulsation properties depend upon metallicity. If this is the case then Figure 1.8 suggests that at a given pulsation period, metal-rich Cepheids are brighter than the metal-poor ones. Therefore, the metallicity of each Cepheid in any given sample needs to be known in order to correct for this. The best way would be to measure the metallicity of each star directly, which can be done using spectroscopy.

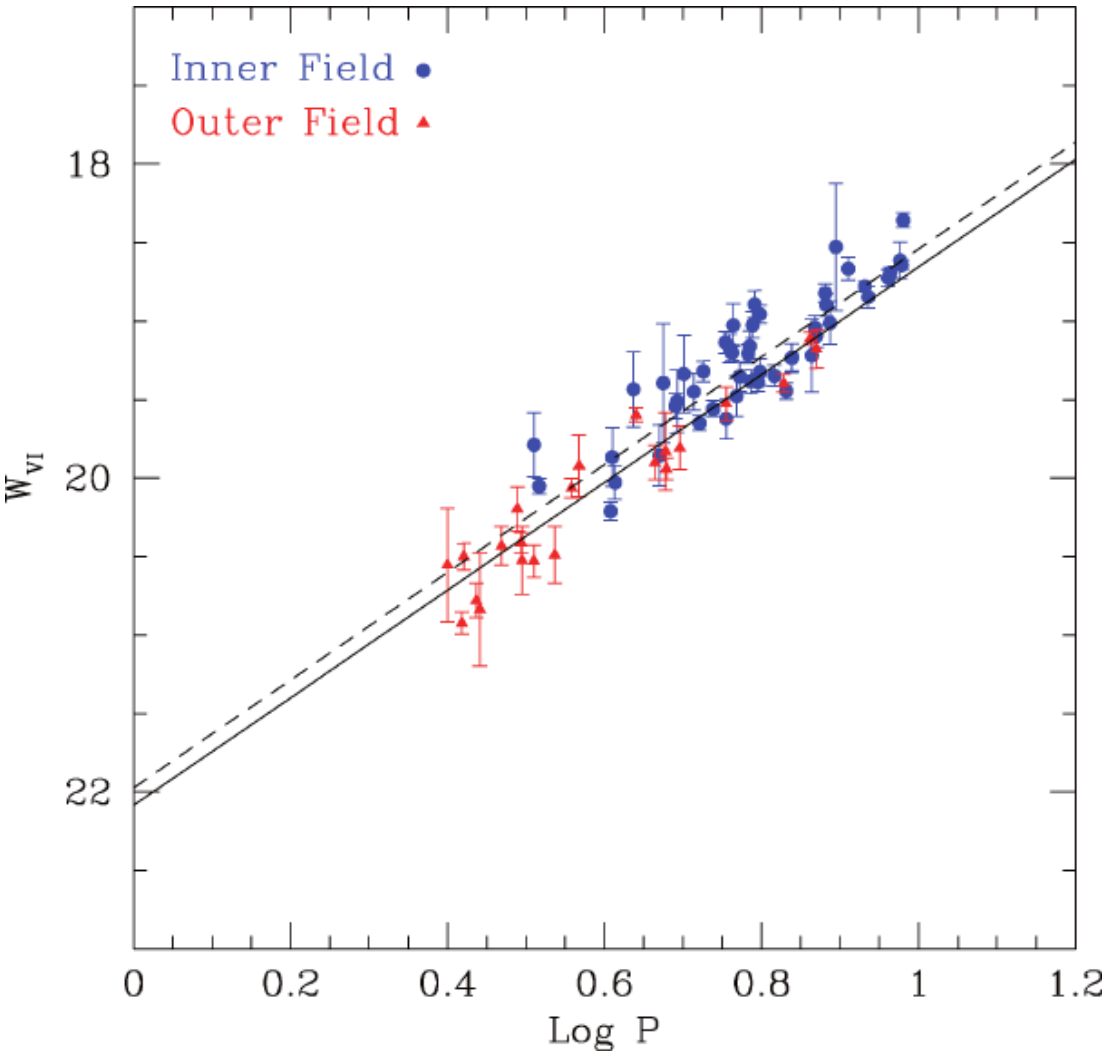

Figure 1.8: Figure from (Scowcroft et al., 2009). Wesenheit magnitude Leavitt Law Plot for inner and outer fields of M33. The two slopes are identical but there is a discrepancy in the zero points.

1.3.1 Measuring Metallicity with Variable Stars

Spectroscopy

To obtain accurate metallicity measurements high-precision spectroscopy is required but with modern instruments this can only be achieved for nearby stars (within the Galaxy or bright stars in the Magellanic Clouds). Romaniello et al. (2005) used high-precision spectroscopy to determine the metallicity of 37 Cepheids in the Milky Way and Magellanic Clouds to asses the influence of metallicity on the Leavitt Law. They found that the required metallicity correction to a PL relation increases with iron content and that the stars become fainter as the metallicity increases until solar metallicity, where there appears to be a flattening or turnover. However, this was only done using Cepheids with a narrow spread in metallicity. To test this in other galaxies at a wider range of metallicities one needs to look at greater distances, such as M31 or M33. The problem with this is that the resolving power, of even the largest telescopes, is not enough to yield true metal-abundances at extragalactic distances. In fact, in order to spectroscopically determine the metallicity of Cepheids at the distances of M31 or M33, at the required resolution, one would need to be able to achieve a signal-to-noise ratio (SNR) 10x greater that what is possible today. One way to get around this is to use spectroscopy to measure the metallicity of HII regions and assign that metallicity to any Cepheids in the vicinity. However, this is no substitute for measuring the metallicity of a star directly.

Thankfully, beat Cepheids are a reliable proxy for determining metallicity. They can be used to trace metallicity because the period ratio, P_1/P_0, is sensitive to metal abundance. Furthermore, this is well described by pulsation models.

Table 1.1: Beat Cepheids in M33

ID	α (J2000.0)	δ (J200.0)	P_0 (days)	P_1 (days)	P_{10}
A	01 34 59.72	30 52 25.2	4.7050	3.3851	0.720
B	01 32 56.82	30 41 33.8	3.9776	2.8611	0.719
C	01 34 33.43	30 51 15.6	3.8271	2.7141	0.709
D	01 33 54.63	30 35 19.8	6.1764	4.3331	0.702
E	01 34 03.97	30 38 08.4	6.1879	4.3348	0.701

Petersen Diagram

Jørgen Otzen Petersen (1973) devised a way to constrain the masses of beat Cepheids by plotting the ratio of the fist overtone and fundamental periods (P_1/P_0) of a beat Cepheid against the logarithm of the fundamental period (log(P_0)). Plotting beat Cepheids on a Petersen diagram can also be used to determine metallicity (Moskalik et al., 1992) as the P_1/P_0 ratio exhibits a strong dependence on metallicity as previously mentioned. Beaulieu et al. (2006) uncovered 5 beat Cepheids pulsating in the fundamental and first overtone modes from the CFHT M33 variability survey conducted by Hartman et al. (2006). The 5 beat Cepheids are presented in Table 1.1 along with their coordinates, periods (P_0 and P_1), and their period ratios (P_1/P_0).

Beaulieu et al. (2006) created a set of stellar equilibrium models using a pulsation code that takes into account parameters of mass M, luminosity L, effective temperature T_{eff} and metallicity Z. They used this to compute mass-luminosity (M-L) plots for the 5 beat Cepheids over a range of T_{eff} that covered the width of the IS with a selection of different metallicities. By superposing modelled evolutionary M-L relations by Bono et al. (2000) they were able to garner the metallicity of each of the beat Cepheids from where the M-L tracks crossed. The Z values derived by Beaulieu et al. (2006) are given in the final column of Table 1.2.

They also plotted the beat Cepheids on a Petersen diagram with comparison to linear fits of Galactic, SMC and LMC beat Cepheids (Figure 1.9) leading to similar metal-

Table 1.2: Beaulieu et al. (2006) metallicities of beat Cepheids in M33

ID	P_{10}	Distance (kpc)	Z
A	0.720	3.5	0.004
B	0.719	3.1	0.005
C	0.709	2.3	0.011
D	0.702	1	0.0125
E	0.701	1	0.0135

licity estimates. Stars A and B fall near the dashed line of the SMC which has a metallicity of Z=0.004. Stars C, D and E fall between the solid line of the Milky Way, Z=0.020, and the dotted line of the LMC, Z=0.008. These values are consistent with the values in Table 1.2.

Buchler and Szabó (2007); Buchler (2008) computed a series of convective models for which both F and O1 modes would become linearly unstable. Figure 1.9 shows a Petersen diagram by Beaulieu et al. (2006) presenting beat Cepheids in our own Galaxy along with those in the SMC, LMC and M33 with Buchler's (2008) tracks superposed. Further use of Buchler's (2008) Petersen diagram metallicity tracks was made by Lee et al. (2013) when they used them to measure the metallicity of beat Cepheids in M31, see Figure 1.10.

1.3.2 Further Considerations in Estimating Cepheid Distances

Theoretical Metallicity Effects

The effect of metallicity on the Leavitt Law as determined by Scowcroft et al. (2009) and Romaniello et al. (2005) seem to be in contradiction. Other empirical relations such as Macri et al. (2006), Storm et al. (2011) or Mager et al. (2013) are inline with Scowcroft et al. (2009), in that at a given period, higher metallicity Cepheids are brighter than their low metallicity counterparts. However, the findings of Romaniello

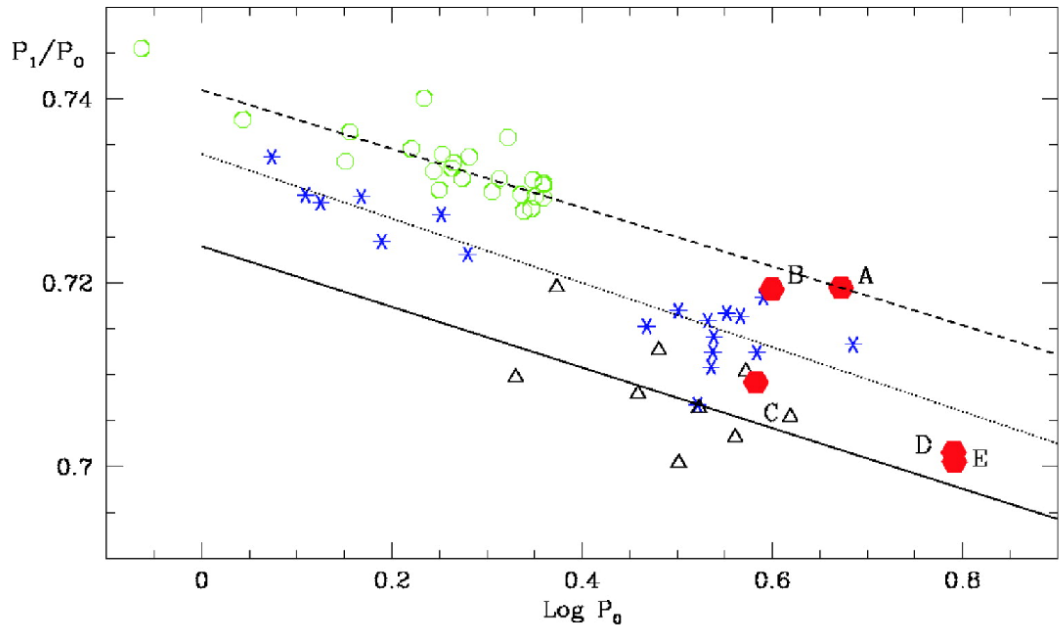

Figure 1.9: Figure from Beaulieu et al. (2006). Petersen Diagram for beat Cepheids pulsating in the fundamental and first overtone modes in our Galaxy (open triangles), the LMC (stars), the SMC (open circles), and M33 (filled hexagons). The linear fits are displayed for our Galaxy (solid line), the LMC (dotted line), and the SMC (dashed line).

et al. (2005) back-up what is found with stellar pulsation models. For example Caputo et al. (2000) and Marconi et al. (2005) both found from their models that increasing metallicity, at a fixed period, Cepheids become fainter. They also find that as metallicity increases the instability strip moves to cooler temperatures i.e. shifts to redder colours with Marconi et al. (2005) also noting a narrowing of the instability strip.

The use of the Leavitt Law to determine Cepheid distance as been discussed in detail, but as well as luminosity, a variable star's pulsation period is tightly correlated with mass and effective temperature. A relationship between a star's mass and luminosity comes out of stellar evolution theory. Also, the effective temperature of a star is indicated by its colour. Therefore, at fixed chemical composition, the brightness of a Cepheid will be a function of its period and effective temperature. For this reason a colour index (CI) term can be added to the PL relation to create a period-luminosity-colour (PLC) relation as in Equation 1.5 (Bono et al., 1999), where $\langle M_j \rangle$ is the mean

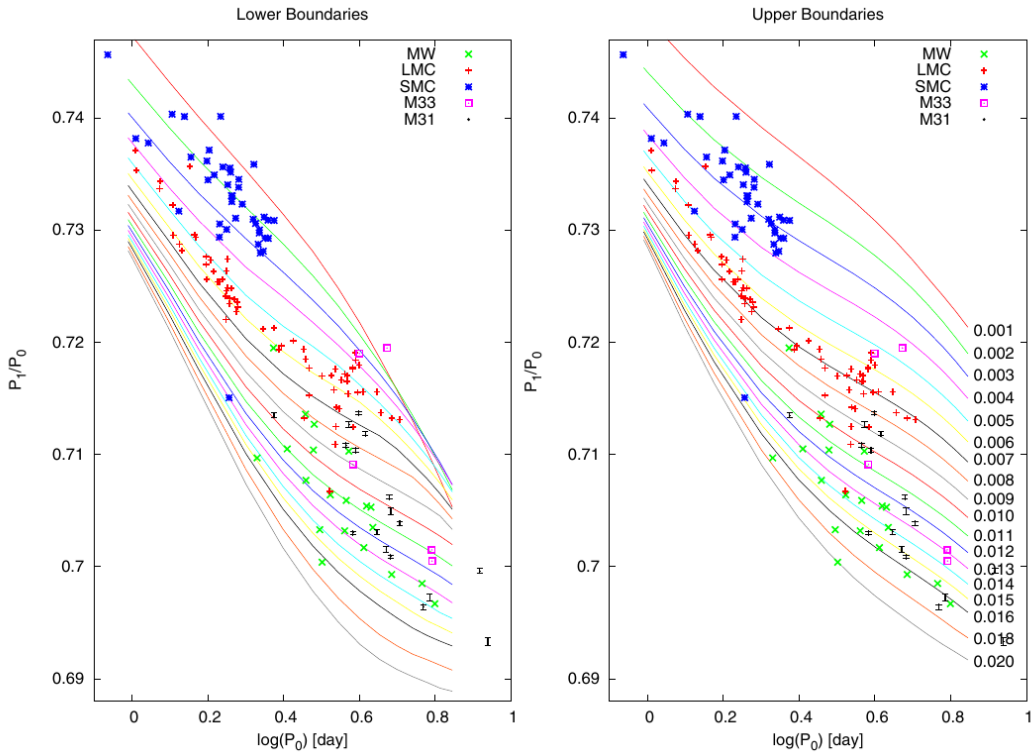

Figure 1.10: Figure from Lee et al. (2013). Updated Buchler (2008) Petersen Diagram by Lee et al. (2013) for beat Cepheids pulsating in the fundamental and first overtone modes in our Galaxy (green crosses), the LMC (red pluses), the SMC (blue crossed pluses), M33 (open violet squares) and M31 (black error bars). The lines show where where both F and O1 modes are linearly unstable at different metallicities.

magnitude across the given bandpass and P is the period.

$$\langle M_j \rangle = \alpha + \beta \log P + \gamma(CI) \tag{1.5}$$

Using their convective pulsation models Bono et al. (1999) also find that at a fixed period metal-rich Cepheids are predicted to be fainter than metal-poor ones. Furthermore, they found that by adopting infrared magnitudes and colors the amplitude of the metallicity effect is greatly reduced. They also checked the distance modulus to the LMC while ignoring its metallicity by using the predicted PL and PLC relations with 3 different chemical abundances. In doing this, they showed that estimates based on the infrared PLC relation were independent of the chosen metallicity, this was not the case in the optical regime. For the PL relation, the distance modulus decreased with increasing metallicity.

Extinction & Reddening

In order to truly understand the effect of metallicity one must remove the effect of interstellar dust. This issue manifests by changing the observed magnitude of a star, extinction, or shifting the observed colour, reddening. The reddening law, Equation 1.6, describes the relationship between extinction, A_X, and reddening, $E(X-Y)$, where X and Y represent the required passbands. $E(X-Y)$, or $E(B-V)$ in this case, is also known as the colour excess (CE).

$$R_V = \frac{A_V}{E(B-V)} \tag{1.6}$$

To include the effects of interstellar dust the distance modulus equation, introduced

earlier as Equation 1.2, needs updating with an extinction term, Equation 1.7.

$$\mu = m - M = 5\log_{10}(d) - 5 + A_V \tag{1.7}$$

In Equation 1.6 the value of R_V is not constant as it depends upon the interstellar medium, making it line-of-sight dependant, but it is typically assumed to have a value 3.1. Lets say that a galaxy has a distance modulus of $\mu = 24.5$ and E(B-V) is 0.1 with R_V at 3.1. Therefore, A_V would be 0.31 making the distance, d, $689\ kpc$. Altering E(B-V) by just 0.05 and propagating through moves the galaxy by nearly $50\ kpc$. However, an elegant solution to the reddening problem is to construct the reddening-free Wesenheit index, W (Madore, 1982; Madore and Freedman, 1991, 2009). This is defined as:

$$\begin{aligned} W &= V - R_V \times (B - V) \\ &= V_0 + A_V - R_V \times (B - V)_0 - R_V \times E(B - V) \\ &= V_0 - R_V \times (B - V)_0 \end{aligned} \tag{1.8}$$

By using the final form of Equation 1.8 it is possible to create period-Wesenheit relations to estimate Cepheid distances whilst circumventing the issues of extinction and reddening. Scowcroft et al. (2009) used a reddening-free Wesenheit index to create the PL relation shown in Figure 1.8, specifically in the form:

$$W_{vi} = V - 2.55(V - I) \tag{1.9}$$

1.3.3 Period-Age Relation

As well as the aforementioned PL relation Cepheids also have a Period-Age (PA) relation. Theory suggests that the more massive a star the earlier the star will leave the main-sequence and evolve to the Cepheid region of the CMD's IS. The relationship between a Cepheid variable star's age and the length of its period has long been theorised (Kippenhahn and Smith, 1969; Bono et al., 2005; Anderson et al., 2016). Figure 1.11 shows how stellar evolutionary tracks of increasing mass pass though the IS at younger ages with larger periods. PA relations can be derived observationally by determining the ages of Cepheids using another method, for example, Cepheids that are hosted by a stellar cluster whose age can be determined by isochrone fitting. Empirical PA relations have been derived from Cepheids in young and massive clusters in the LMC by Efremov (1978, 2003) whose LMC PA relation is included here as Figure 1.12. Having a robust Cepheid PA relation means that once the period of any Cepheid is found its age can be immediately determined. This means that the star formation history of any region that contains Cepheids can be studied simply. The Cepheid PA relation also presents the opportunity to test and constrain stellar models.

The key benefits in estimating the Cepheid ages from the PA relation are that they the observable parameter on which they rely, the period, is only marginally affected by systematic errors. The age estimates from the PA relation are based on individual objects, therefore, they supply an accurate age gradient across a galaxy as stellar clusters are outnumbered by Cepheids. Empirical PA relations however, are subject to drawbacks. Uncertainties in the distance moduli and reddening of clusters used cause uncertainty in the PA relation derived from them. There also tends to be a range in periods of the Cepheids in any single cluster. It tends to be assumed that the temperature width of instability strip is negligible when deriving Cepheid ages from a PA relation.

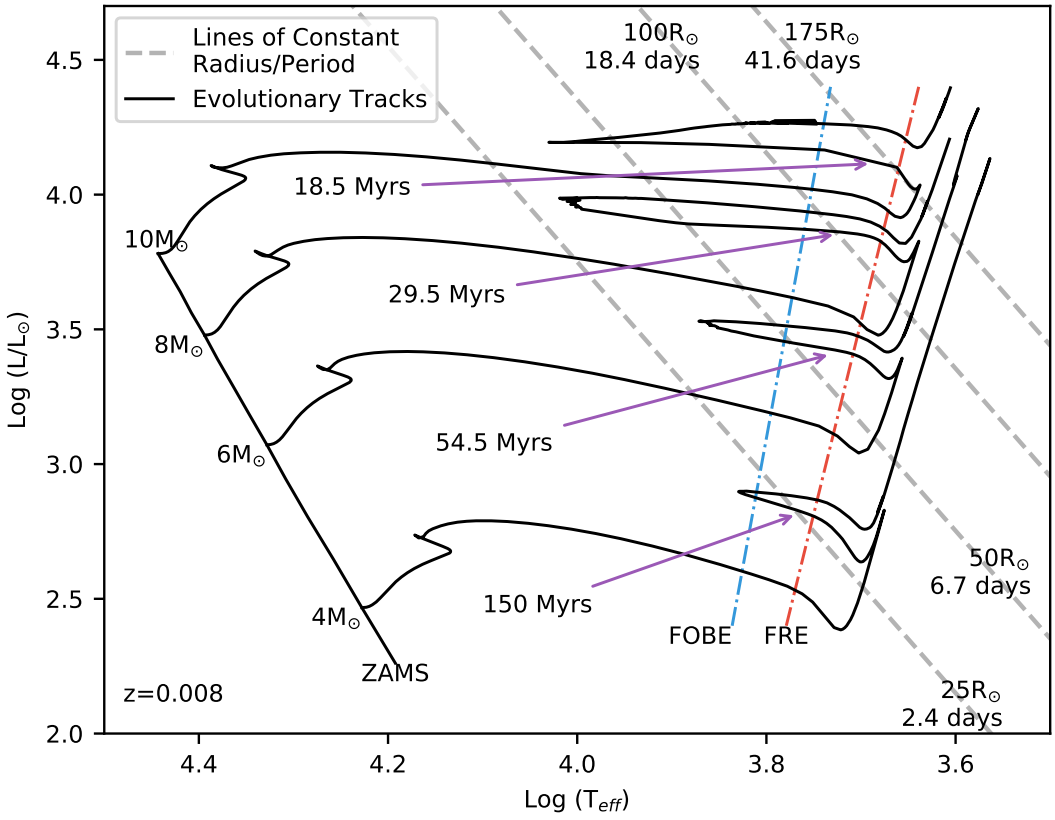

Figure 1.11: Hertzsprung-Russell Diagram with evolutionary tracks for stars of increasing mass showing how the instability strip period increases as age decreases. The solid black lines represent evolutionary tracks for stars of metallicity z=0.008 with masses indicated to the left of each track. The tracks were created using the BaSTI web tools (Pietrinferni et al., 2004). The period value for each stellar radius was determined using an equation from (Gallenne et al., 2017). The dash-dot blue and red lines show the positions of the first overtone blue edge (FOBE) and fundamental red edge (FRE) of the instability strip (Bono et al., 2005).

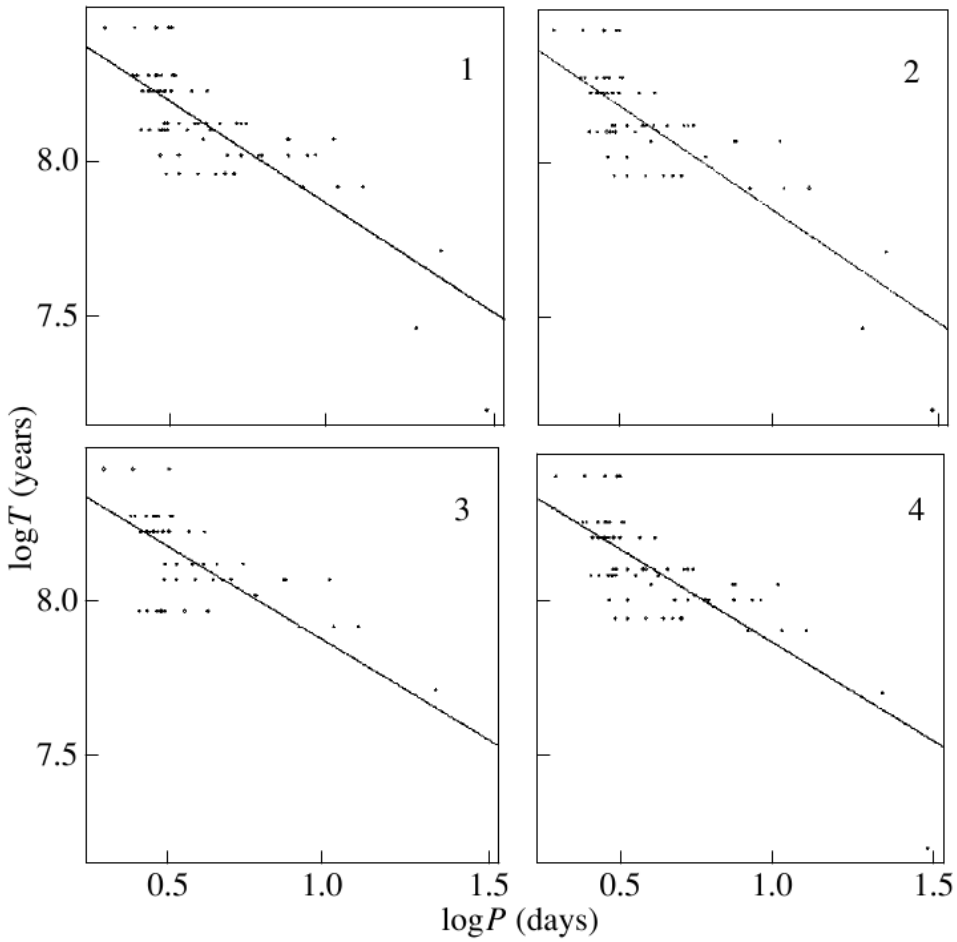

Figure 1.12: Different versions of the period-age relation for LMC clusters by Efremov (2003). See text for details.

Period-Age-Colour Relation

A period-age-colour (PAC) relation should be used to estimate Cepheid ages because then the individual Cepheid positions inside the instability strip is accounted for (Bono et al., 2005). The main drawback with this is that if the PAC relation was to be derived empirically with an incorrect reddening correction then one would have a PA relation with unnecessary error added. Also, Bono et al. (2005) found that only when the uncertainty of the reddening correction is smaller than 0.08 mag for $B - V$ colours and smaller than 0.07 mag for $V - I$ colours do the the ages derived from the PAC relation become more precise than ages derived from the PA relation.

Stellar Rotation

One thing that can affect the evolution of a star is its initial rotation rate. Rotation causes stars' main-sequence lifetimes to increase due to the mixing process supplying the core with fresh Hydrogen during the core Hydrogen burning phase. This means that Cepheids whose progenitors have faster initial rotation rates will show longer periods than those with slower initial rotation rates at the same age. This affects the PA relation by causing an increase in the spread of periods observed in Cepheids from a single cluster. Therefore, rotation rates should be considered when using the PA relation. The effect of rotation on Cepheid periods will be investigated in Chapter 4 using the rotation models from the SYCLIST web tool for Geneva stellar models (Georgy et al., 2013a,b). The models are parameterised by the following equations:

$$\omega_{ini} = \frac{\Omega}{\Omega_{crit}} \tag{1.10}$$

$$\Omega_{crit} = \sqrt{\frac{GM}{R^3_{e,crit}}} \tag{1.11}$$

Where ω_{ini} is the ratio of the star's initial angular velocity (Ω) to the critical angular velocity (Ω_{crit}). The critical limit is defined as where the outward forces due to rotation and radiation pressure become strong than gravity (Maeder and Meynet, 2000). Ω_{crit} is defined in Equation 1.11 where $R^3_{e,crit}$ is the equatorial radius when the star is rotating at the critical rate (Georgy et al., 2013b). Figure 1.13 shows how the initial rotation rate of stars influences at which point during their evolution they cross the IS and how this affects the pulsation period.

1.4 Stellar Populations

1.4.1 Stellar Clusters

Stellar clusters are ideal stellar laboratories as all of the stars are born from the same gas cloud. Therefore, all of the stars are of the same chemical composition and roughly the same age.

As previously mentioned the younger a Cepheid the longer its period. Therefore Cepheids in young clusters will have longer periods than Cepheids in old clusters, hence clusters are perfect for studying the Cepheid PA relation as they are considered to be simple stellar populations.

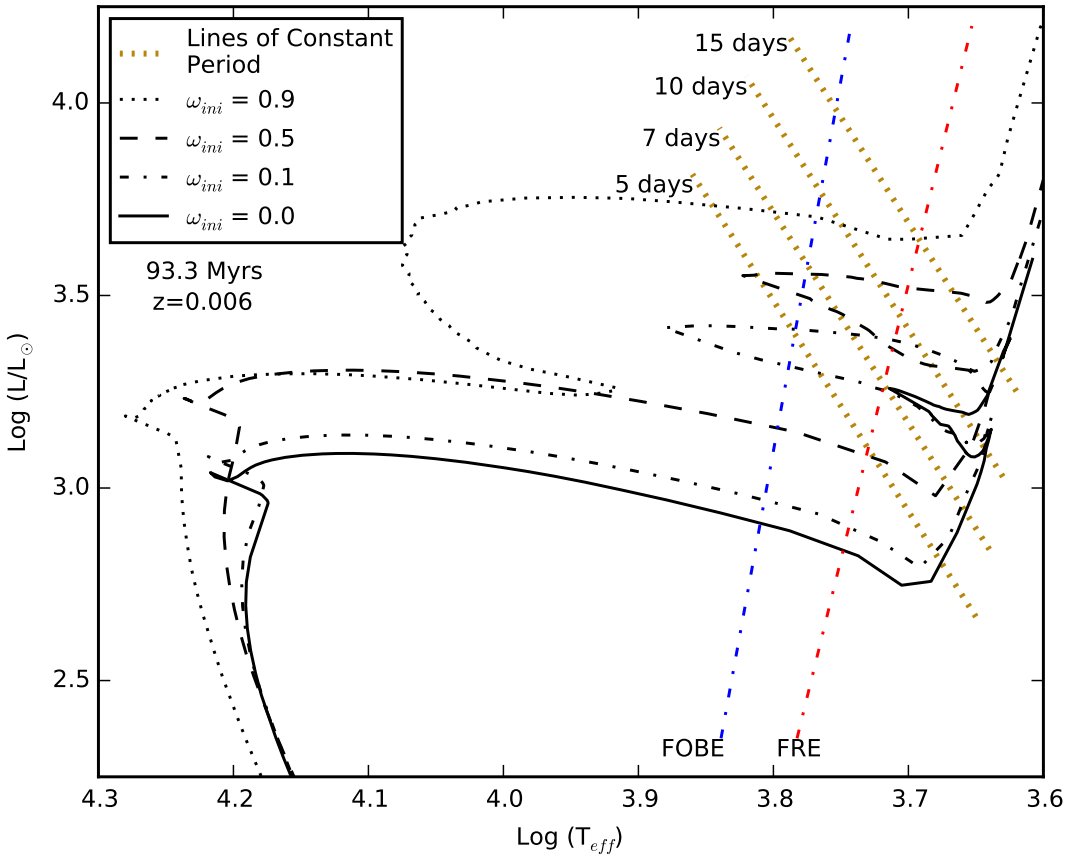

Figure 1.13: Hertzsprung-Russell Diagram showing the effect of a star's initial rotation rate on where it crosses the instability strip. Lines of constant period and instability strip boundaries are the same as in Figure 1.11. The black lines show isochrones created using the SYCLIST web tool for Geneva stellar models of different initial average rotation rates (ω_{ini}) (Georgy et al., 2013b).

1.4.2 Measuring Cluster Ages

One method of measuring the age of a stellar clusters is isochrone fitting. An isochrone is a curve that can be placed on a CMD or HRD that represents a simple stellar population inasmuch as that all of the stars represented by the curve are of the same composition, age and rotation rate. By plotting several isochrones upon a CMD of a stellar cluster the age of the cluster can be determined by figuring out which isochrone fits the data the best. Figure 1.14 shows how the age of stellar cluster M4 can be determined with the use of isochrones.

The ages of any Cepheids in a cluster are known. Therefore, if one has multiple Cepheids from different clusters of various ages one can empirically derive the Cepheid PA relation.

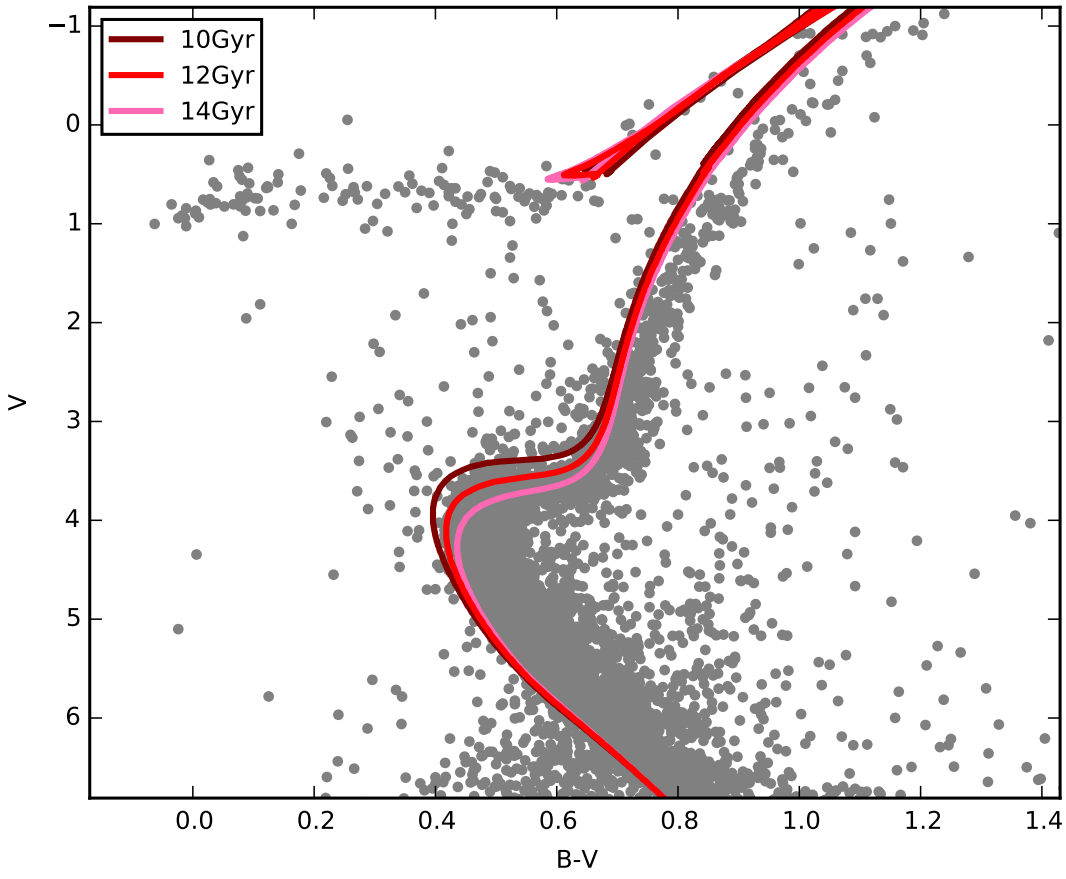

Figure 1.14: Colour-Magnitude Diagram of Galactic globular cluster M4 with isochrones to demonstrate how a stellar cluster's age can be determined. M4 photometry by Stetson et al. (2014). The isochrones were created using the BaSTI web tools (Pietrinferni et al., 2006). See text for details.

Chapter 2

Image Subtraction Processing and Calibration of M33 Data

2.1 M33

M33 (the Triangulum galaxy) is a spiral galaxy and is the third largest galaxy in the Local Group behind the Andromeda galaxy (M31) and the Milky Way. M33 is a relatively close galaxy, it has been well studied with many parameters known, for example, it is known to exhibit a metallicity gradient as does the Milky Way and M31 but these galaxies present observational difficulties. M33 has multiple observational advantages over other galaxies in the Local Group. Large parts of the Milky Way are obscured from our view by itself as we are a part of it. Therefore, to study galaxies observationally we need to look elsewhere. Nearby satellite galaxies such as the Magellanic Clouds show a flat metallicity distribution. To study more complex systems we are left with the large spiral galaxies of M31 and M33. M31 is the largest and closest spiral galaxy but has a inclination angle of 77° (Athanassoula and Beaton, 2006) to Earth

which means that observations are plagued by crowding as well as increased extinction and reddening. M33 as an inclination angle of 53° (Scowcroft et al., 2009) making it more 'face-on' so we observe less crowding and we can assume that any Cepheids we observe are at pretty much the same distance. M33 is also a good laboratory for young stellar tracers as it has a fairly high star-formation-rate (SFR), in fact, it is forming stars at a higher rate than M31 (Corbelli et al., 2009). Different methods of measuring M33's metallicity gradient yield different results. We will present here our reduction and calibration of M33 data in order to find beat Cepheids and use them to explore M33's metallicity gradient.

2.2 Data

2.2.1 Canada France Hawaii Telescope

Hartman et al. (2006) conducted a variability survey on the Triangulum galaxy, also known as M33, using the Canada France Hawaii Telescope (CFHT) on 27 nights over 17 months beginning August 2003 in which they identified over 36000 variable objects. CFHT is a 3.6m telescope in Hawaii and uses a one square degree imager called MegaCam[1]. This instrument is comprised of 36 CCDs with each being 2048×4162 pixels at 0.187 arcsec pixel^{-1}. The observations are in Sloan-like g', r' and i' band filters. Figure 2.1 shows a composite colour mosaic stack of the CFHT observations of M33. The images were initially processed as part of the Queue Service Observing mode using the `ELIXIR` pipeline which performs bias, dark frame, flat-field and fringe corrections.

[1]Based on observations obtained with the MegaPrime/MegaCam, a joint project of Canada-France-Hawaii Telescope (CFHT) and CEA/DAPNIA, at the CFHT which is operated by the National Research Council (NRC) of Canada, the Institut National des Science de l'Univers of the Centre National de la Recherche Scientifique (CNRS) of France, and the University of Hawaii.

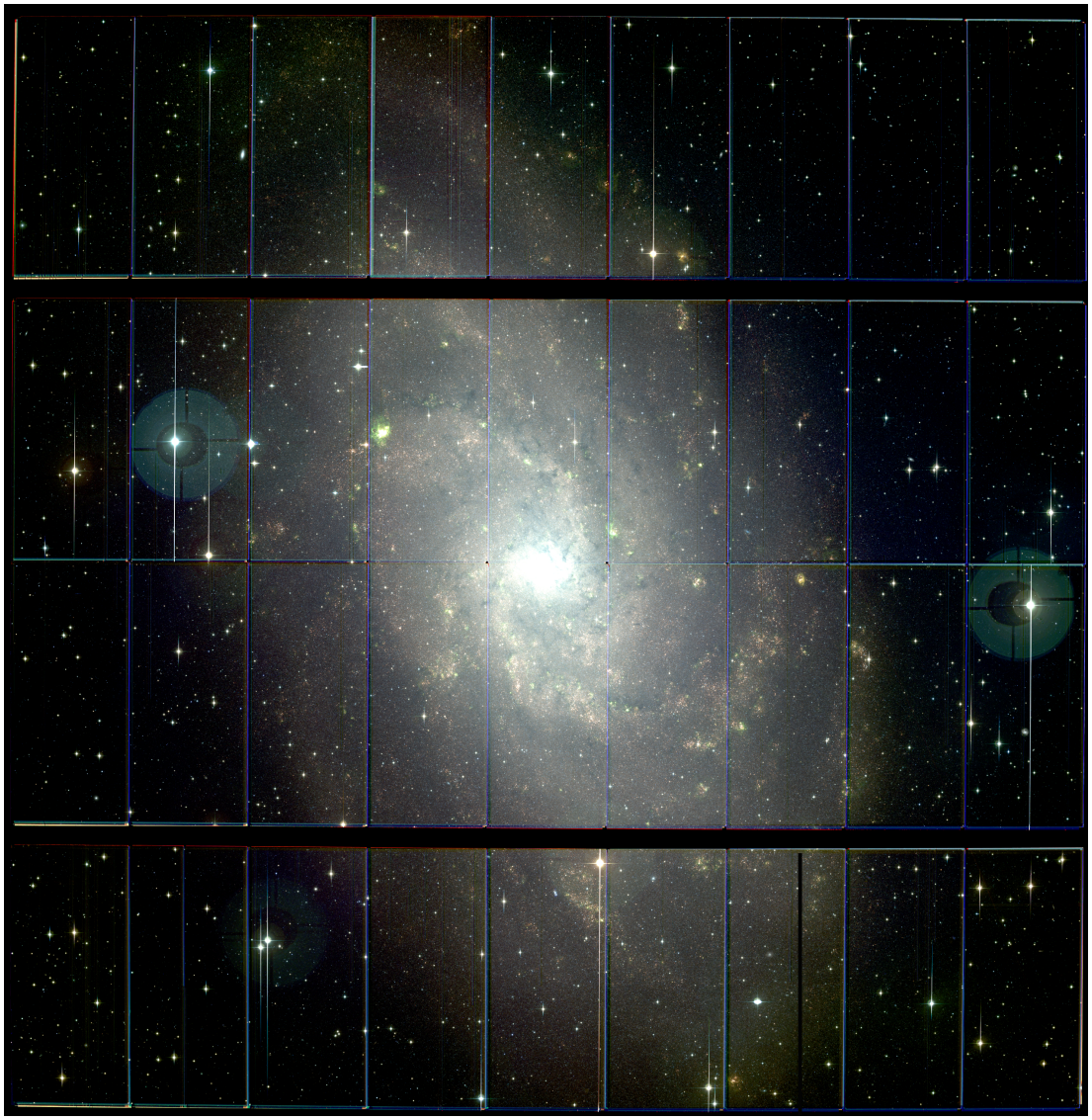

Figure 2.1: Colour mosaic of M33 created using the CFHT images (Hartman et al., 2006).

Hartman et al. (2006) produced an initial catalogue of variable point sources using image subtraction techniques. This works by creating a reference image by averaging the best seeing images for each filter/chip combination. A transformation of the PSF, flux and background between the reference and the individual images was found using software know as `ISIS` (Alard and Lupton, 1998; Alard, 2000). The transformed images are subtracted in turn from the reference image resulting in residual images containing dark and light spots indicating objects that have changed in brightness. To detect any variable objects, the residual images are divided by the square root of the original, then the absolute values of the pixels are co–added. This gives an image clearly showing the variables, with the flux of the point-sources proportional to the significance of the variability, producing a catalogue of $\sim$36000 objects. Light curves were obtained by performing PSF photometry on the residual images. Cepheids were then identified from the positions of these sources on the CMD reducing the catalogue to $\sim$3000 Cepheid candidates.

2.2.2 Isaac Newton Telescope

The Isaac Newton Telescope (INT) is a 2.5m telescope at the Observatorio del Roque de los Muchachos, La Palma[2]. The wide field camera consists of four 2048$\times$4096 pixel CCDs, orientated as in Figure 2.2, with a scale of 0.333 arcsec pixel^{-1}. To cover the entire galaxy four pointings were required, a mosaic image of the four pointings of the four chips is shown in Figure 2.3 where the overlap regions can also be seen. The data was taken on 13 nights spread between 3 observing runs over 19 months beginning February 2008 producing $\sim$45 epochs in total. The images were initially

[2]Based on observations made with the Isaac Newton Telescope operated on the island of La Palma by the Isaac Newton Group in the Spanish Observatorio del Roque de los Muchachos of the Instituto de Astrofsica de Canarias

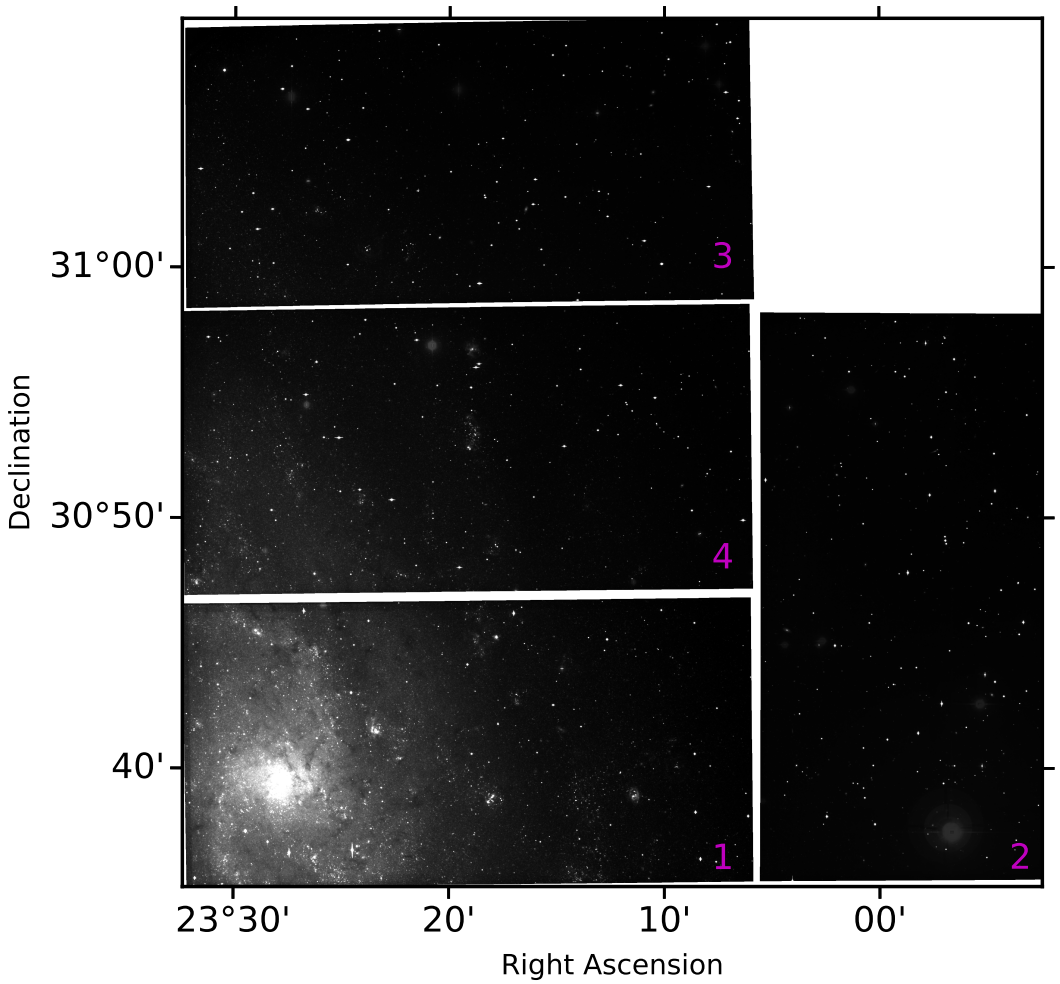

Figure 2.2: Configuration of INT chips

processed by David Bersier using the IRAF[3] (Image Reduction and Analysis Facility) CCDPROC package, performing bias, dark frame, flat-field and fringe corrections.

Together, the CFHT and INT data gives ∼80 epochs in the r' band and ∼40 in both the g' and i' bands.

[3]IRAF is distributed by the National Optical Astronomy Observatories, which are operated by the Association of Universities for Research in Astronomy, Inc., under cooperative agreement with the National Science Foundation.

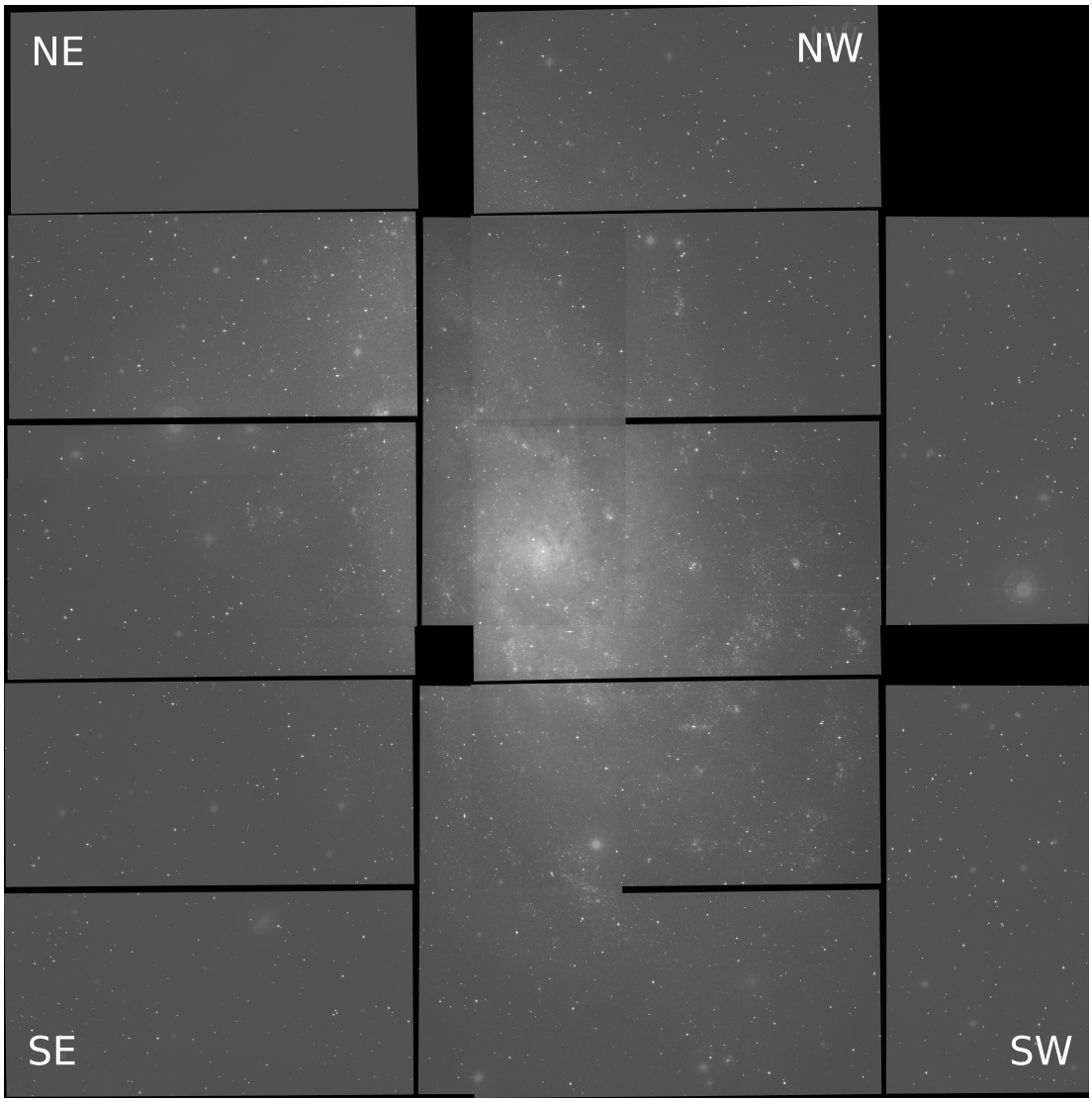

Figure 2.3: Mosaic of r'-band INT Templates

2.3 Calibration

A large portion of the work for sections 2.3 and 2.4 was carried out by Kevin Tsang and is also presented in his thesis. The calibration of the INT data with SDSS catalogues (Alam et al., 2015) using PSF fitting photometry with `SExtractor` and `PSFex` (Bertin and Arnouts, 1996) was done by Kevin Tsang, as well as the calibration of the INT and CFHT, bringing the two datasets onto the same photometric scale. The creation of the INT templates and the comparison of Kevin Tsang's calibration to calibration using `IRAF` was done by the royal we, as well as the image subtraction and calibration of light curves presented from section 2.5 onwards.

To calibrate the M33 data, images were taken of the SDSS field Stripe 82 during the INT observing run in order to work out the response of the CCDs at the INT. Standard star catalogues of these fields were downloaded from the Sloan Digital Sky Survey (SDSS) data release 12 (dr12) (Alam et al., 2015) from http://skyserver.sdss.org/dr12/. Images from the night of October 7, 2009 were chosen as the night with the best seeing.

The stars in each of the INT standard field images are detected using the `DAOFIND` task of the `DAOPHOT` package (Stetson, 1987) within `IRAF`. The `DAOPHOT` (Stetson, 1987) parameters that were changed from default values within `IRAF` are presented in Table 2.1. The coordinates of these stars are found by getting the World Coordinate System (WCS) information for the image using the on-line tool http://nova.astrometry.net. For the parameters and uncertainties associated with the astrometric solution see Appendix B. Using the WCS data the standard star images can be matched to stars in the downloaded SDSS catalogues (Alam et al., 2015). Aperture photometry is then run on the INT images using the `IRAF` task `PHOT`. A configuration file then needs to be created which includes the transformation equations to match the photometry done on the INT images with the known magnitudes of the stars from the SDSS catalogue (Alam et al.,

Table 2.1: Non-default IRAF DAOPHOT (Stetson, 1987) parameters used for comparison with Kevin Tsang's photometry.

FWHMPSF	2.5
SIGMA	20.35
EPADU	2.8
READNOISE	6.4
ANNULUS	25.
DANNULUS	25.
SMAXITER	10
SNREJECT	50

2015). The FITPARAMS task is used to solve the transformation equations which take into account the zero-point (Z_p), the airmass (A) and a colour-term (C) as in the form of Equation 2.1 where m1 and m2 are the coefficients of the fit. The fit is then inverted producing a calibrated catalogue of stars from the INT images. In this case that fit is presented in the upper panel of Figure 2.4 as the black circles.

$$m_{Inst} = m_{SDSS} + Z_p + (m1 \times A) + (m2 \times C) \tag{2.1}$$

When the field is crowded with many stars close together the photometry becomes more difficult as it may be hard for software to differentiate one star from another. Another issue is that if one tries to perform aperture photometry, in which you place an aperture centred on an object and subtract the average surrounding sky count per pixel from the pixel count of the object, it might not be possible to use an aperture small enough to centre on just one object. Fortunately, software exists to deal with these issues such as the DAOPHOT (Stetson, 1987) package which includes a FIND feature for locating all the stars on a CCD chip and is especially designed for crowded field PSF fitting photometry. PSF fitting works by fitting Gaussians over the field to reduce the effects of star blurring so that magnitudes can be determined for all the stars in the chip, even the ones that appear to have merged together.

Table 2.2: Kevin Tsang's calibration solutions for the INT chips for Equation 2.2.

Filter	Z	k	c	d	e	RMS
Chip 1						
g'	-30.411	0.166	-0.143	-0.589×10^{-5}	1.847×10^{-5}	0.034
r'	-30.053	0.089	-0.007	-2.524×10^{-5}	2.571×10^{-5}	0.027
i'	-29.593	0.056	-0.059	-3.365×10^{-5}	2.288×10^{-5}	0.032
Chip 2						
g'	-30.063	0.166	-0.134	-1.511×10^{-5}	-1.595×10^{-5}	0.036
r'	-29.722	0.089	0.001	2.990×10^{-5}	-1.667×10^{-5}	0.031
i'	-29.242	0.065	-0.067	2.382×10^{-5}	-2.453×10^{-5}	0.034
Chip 3						
g'	-30.273	0.166	-0.147	-6.734×10^{-5}	2.628×10^{-5}	0.047
r'	-30.103	0.089	-0.005	0.155×10^{-5}	1.826×10^{-5}	0.027
i'	-29.683	0.056	-0.094	-0.804×10^{-5}	1.914×10^{-5}	0.028
Chip 4						
g'	-30.207	0.166	-0.142	-0.155×10^{-5}	1.719×10^{-5}	0.028
r'	-29.902	0.089	0.001	0.212×10^{-5}	1.892×10^{-5}	0.027
i'	-29.500	0.056	-0.067	-1.842×10^{-5}	2.149×10^{-5}	0.030

Other software exists for performing PSF fitting photometry such as `SExtractor` and `PSFEx` (Bertin and Arnouts, 1996). Using this software Kevin Tsang performed PSF photometry on the same data to produce transformation equations in that included a zero-point (Z_p) as well as colour (Col), airmass (l) and position terms (X & Y) in the form of Equation 2.2. The values and uncertainties associated with Equation 2.2 for each chip and filter are presented in Table 2.2. The fit was inverted to produce a calibrated catalogue of stars from the INT images. In this case that fit is presented in the upper panel of Figure 2.4 as the grey circles.

$$m_{Inst} = m_{SDSS} + Z_p + (k \times l) + (c \times Col) + (d \times X) + (e \times Y) \tag{2.2}$$

A direct comparison between the `IRAF` and the `SExtractor/PSFEx` (Bertin and Arnouts, 1996) fits is shown in the lower panel of Figure 2.4. Both methods produce similar results, however the PSF method produces a tighter correlation with the SDSS data (Alam et al., 2015) especially at the fainter end.

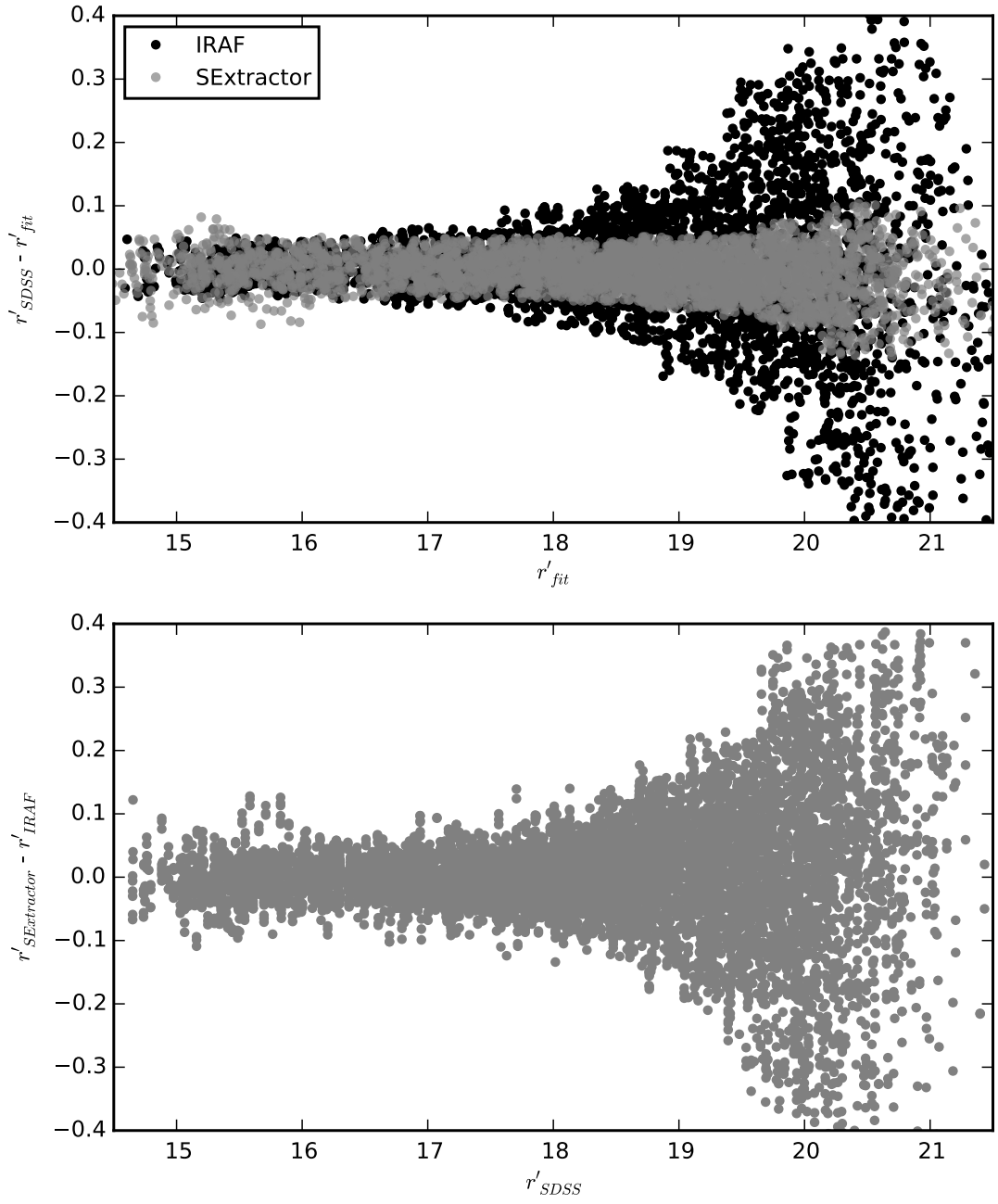

Figure 2.4: Comparison of r'-band Photometry performed on the INT data of Stripe 82 taken on the night of October 7, 2009 between the `Daophot` (Stetson, 1987) package within `IRAF` and `SExtractor` (Bertin and Arnouts, 1996).

Table 2.3: Numbers of images that went into building the templates for each chip of the INT M33 data in each filter along with the average seeing for the templates. The pointing regions are as shown in 2.3.

Chip	No. of g' images	FWHM (arcsec)	No. of r' images	FWHM (arcsec)	No. of i' images	FWHM (arcsec)
NE						
1	4	1.22	14	1.14	3	1.14
2	4	1.44	14	1.23	3	1.18
3	3	1.17	20	1.09	3	1.14
4	4	1.28	13	1.10	3	1.07
NW						
1	5	1.14	15	1.13	3	1.07
2	4	1.24	17	1.30	3	1.40
3	4	1.15	17	1.13	3	1.20
4	4	1.14	18	1.13	3	1.10
SE						
1	3	1.14	20	1.14	4	1.01
2	3	1.22	21	1.22	5	1.04
3	3	1.11	19	1.11	3	1.00
4	3	1.13	20	1.13	4	1.00
SW						
1	3	1.04	16	1.12	4	0.99
2	3	1.14	15	1.21	4	1.07
3	3	1.12	9	1.06	3	1.05
4	3	1.06	12	1.08	3	1.04

2.4 Templates

2.4.1 Image Stacking

Template images were built from the INT data to be used as the reference frames for image subtraction as well as for photometric calibration. To build the templates we identified which of the images in each set had the best seeing as well as the least elongated or skewed stars. We created a Python script which subtracts a background flux level from each of the images, registered them to the most central image, based on their WCS information, and measured the average full width half maximum (FWHM) of the stars in each frame as well the average roundness of each of the stars. On a

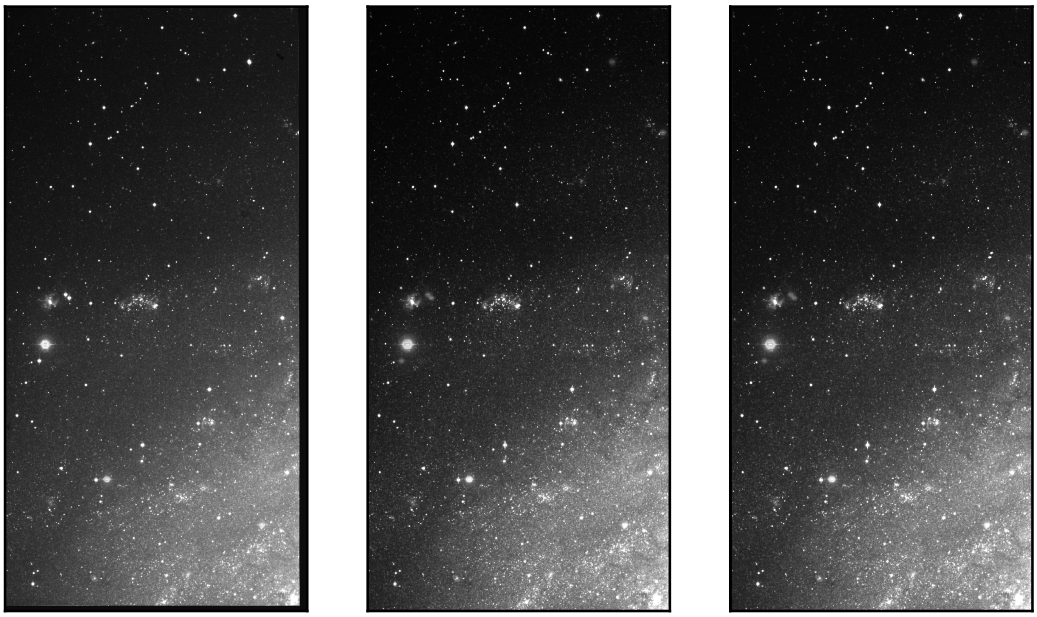

Figure 2.5: Sample of best 'seeing' images used produce one of the INT templates

CCD chip each star can be fitted by a Gaussian-function, the FWHM is the radius which corresponds to half the value of the height of the Gaussian. To calculate which images provided the roundest stars, the average elongation of the stars in each image was taken into account. The elongation is calculated by taking a ratio of the number of pixels across the longest and shortest axes of each star. The closer this value is to 1 the better. The images whose average FWHM and average elongation that were within 2-σ of the best image were averaged together to produce the templates. Figure 2.5 shows a sample of some of the best quality frames that went into producing the template for the NW region r'-band chip 4. The number of images that went into each of the template in each filter as well as the average FWHM can be found in Table 2.3.

2.4.2 Template Calibration

The sources in the templates for the M33 INT data are very crowded so aperture photometry is not possible. Therefore another method is needed for the calibration. The

photometry on the templates was done by Kevin Tsang via PSF fitting photometry using `PSFex` and `Sextractor` (Bertin and Arnouts, 1996) and using the transformation equations calculated from the SDSS fields, Equation 2.2.

Using the Stripe 82 solutions for the INT chips, Kevin Tsang transformed the instrumental magnitudes of the single-epoch INT M33 images the standard system. Kevin Tsang then calibrated PSF magnitudes from the INT templates against the calibrated single-epoch M33 magnitudes. The CFHT stacks are comprised of mosaic frames each containing 36 sub-images from the 36 CCD chips which do not necessarily behave the same. Therefore, Kevin Tsang seperated the stars in the CFHT stacks into 36 groups corresponding to the position of each chip. They were then calibrated separately using the INT template magnitudes for reference. Figure 2.6 shows two of Kevin Tsang's CMDs, the one on the left is produced using stars from the calibrated CFHT catalogue and the one on the right from INT template stars. Some SDSS data (Alam et al., 2015) is available for the outer regions of M33, Figure 2.7 shows that comparisons between the SDSS data (Alam et al., 2015) and the calibrated CFHT stack are in agreement. Therefore, we can be confident in saying that the photometry and calibration procedures are accurate.

Figure 2.8 shows the positions of the Cepheids from the Hartman et al. (2006) list on the CMD and, as we can see, the majority of Cepheids are located approximately between the g' - r' values of -0.2 - 1.4 mag. Kevin Tsang found that several of the Cepheids had anomalous g' - r' colours placing them outside the confines of the blue and red edges of the instability strip in Figure 2.8 removing $\sim$500 candidate Cepheids.

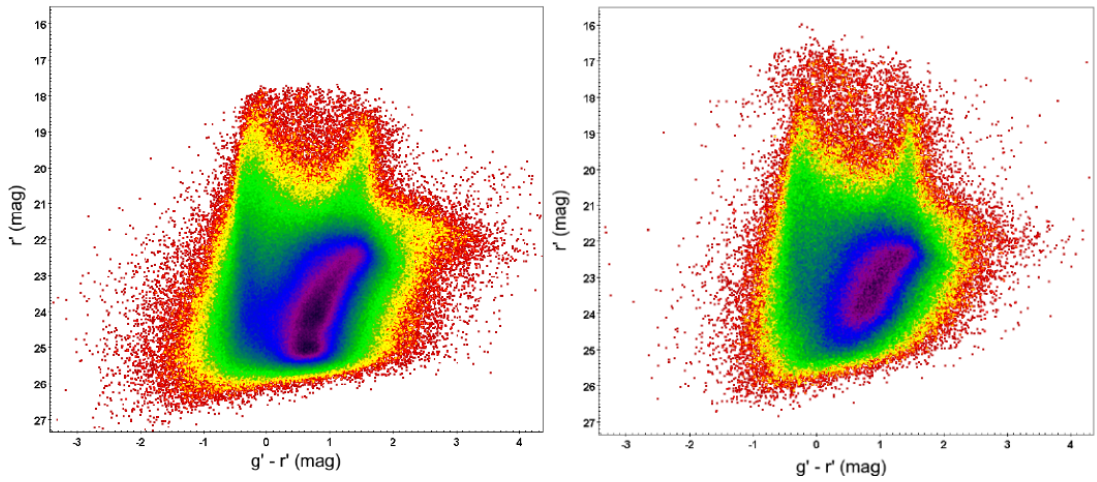

Figure 2.6: r' versus g' - r' CMDs produced by Kevin Tsang where colour indicates stellar density, with red representing the least dense regions and violet representing the most dense regions. *Left-hand panel:* Stars from the CFHT stack catalogue. *Right-hand panel:* Stars from the INT template catalogue. The CFHT catalogue goes $\sim$1 mag deeper that the INT catalogue.

2.5 Image Subtraction

To find the variable sources in our datasets we use image subtraction methods. This involves the pixels of one image being subtracted from another to leave behind only the objects that have changed in brightness. To do this images need to be both astrometrically and photometrically aligned. Astrometric alignment of the images entails making sure that the same stars in each frame are centred on the same pixel which we implemented using `IRAF`. To register the images to one another the `GREGISTER` package in `IRAF` was used, which transforms the pixel positions of the stars in one image to another from transformation equations produced by the package `GEOMAP`. `GEOMAP` produces these equations from the transformation calculated by the package `XYXYMATCH`. `XYXYMATCH` calculated this transformation using the 'triangles' algorithm which matches all the possible triangles that can be formed from the point-sources in each image. Once aligned, we filtered out images with the best astrometric 'seeing' to be averaged together to build a reference image with a good signal-to-noise ratio. The images taken on different nights were then individually subtracted from

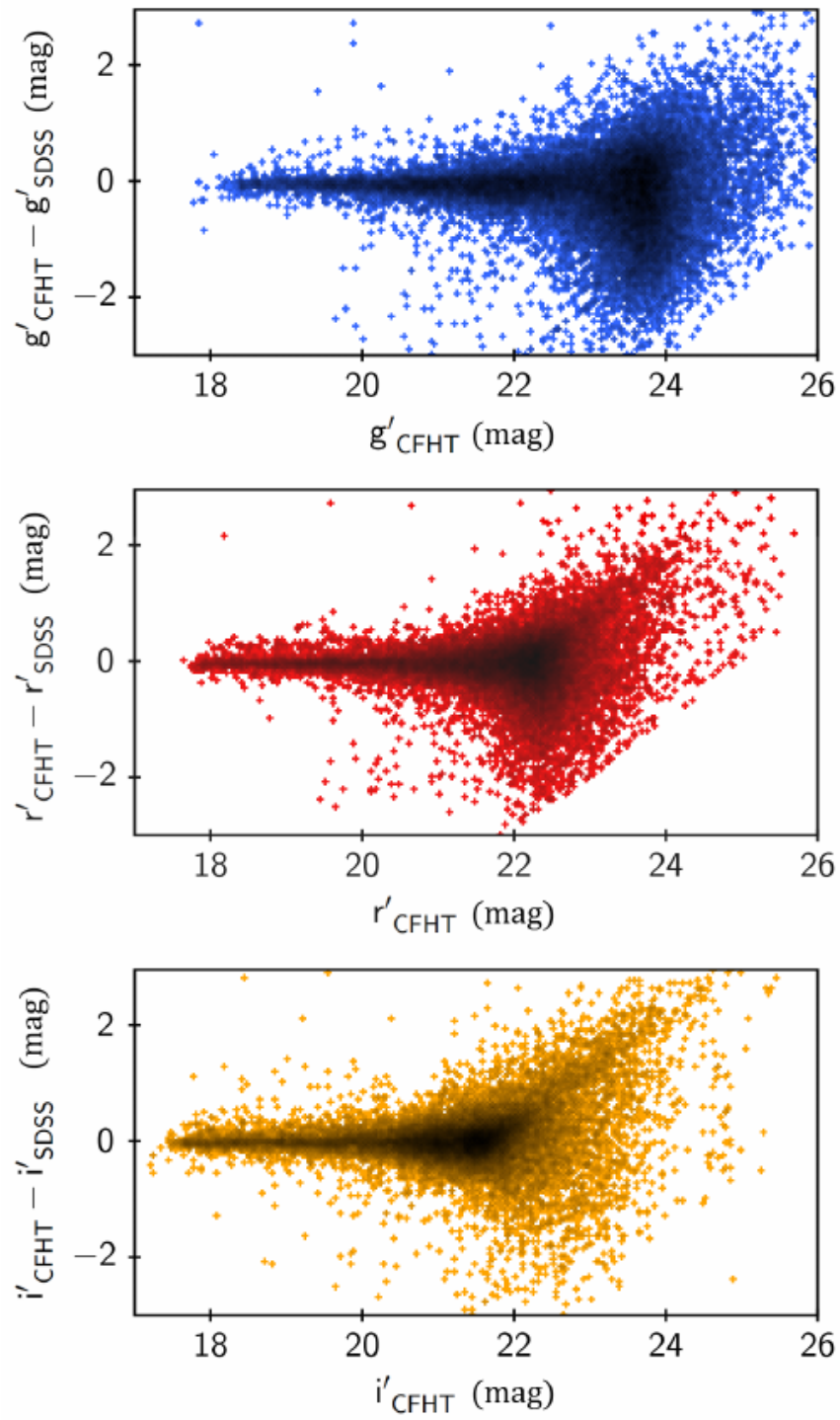

Figure 2.7: Comparison between Kevin Tsang's calibrated CFHT magnitudes and magnitudes from the SDSS catalogue (Alam et al., 2015). Plot produced by Kevin Tsang.

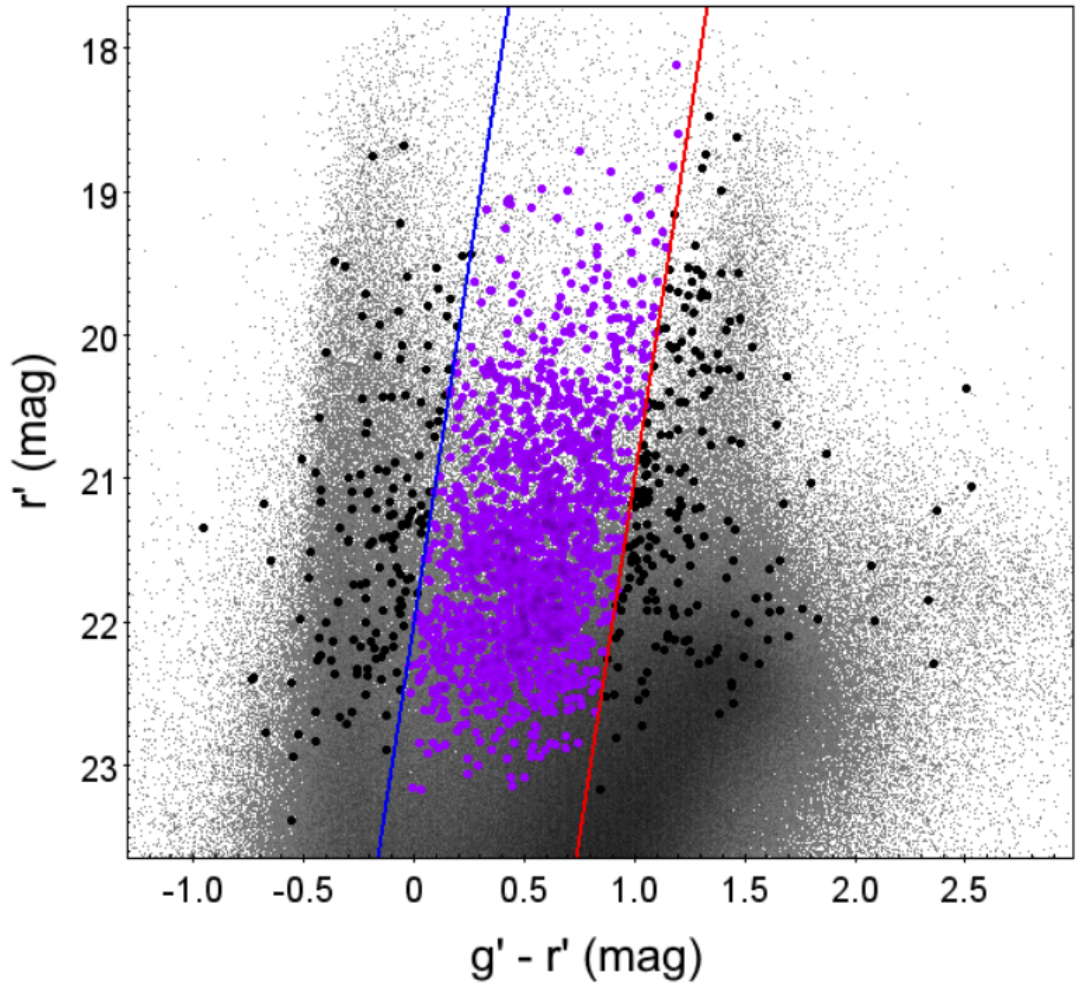

Figure 2.8: CMD produced by Kevin Tsang of M33 stars (gray points), Cepheids with anomalous g' - r' colours (black points) and Cepheids with acceptable g' - r' colours (magenta points). The blue and red lines mark the approximate edges of the instability strip.

Table 2.4: Non-default HOTPANTS (Becker, 2015) parameters used for image subtraction.

[-r rkernel]	11	convolution kernel half width
[-nrx xregion]	1	number of image regions in x dimension
[-nry yregion]	2	number of image regions in y dimension
[-nsx xstamp]	20	number of each region's stamps in x dimension
[-nsy ystamp]	20	number of each region's stamps in y dimension
[-ko kernelorder]	2	spatial order of kernel variation within region
[-bgo bgorder]	2	spatial order of background variation within region

the reference image using the image subtraction software HOTPANTS (High Order Transform of PSF And Template Subtraction) (Becker, 2015), based on the ISIS image subtraction package described by Alard and Lupton (1998); Alard (2000). The images were taken on different nights so are subject to different atmospheric conditions, for this reason the images need to be photometrically aligned before applying image subtraction so that only the variable objects are left behind. HOTPANTS photometrically aligns the two images by estimating the size of the Gaussians needed to make up a convolution kernel from the sizes of the PSFs on the images input by the user. Using this kernel one image is then convolved so that the photometry matches the other before the pixels are subtracted. The HOTPANTS (Becker, 2015) parameters that were changed from default values for the image subtraction are presented in Table 2.4. Once subtracted all of the non-variable objects should have been removed with only those that have changed brightness in the time between remaining. Any bad or saturated pixels left over were simply ignored. Figure 2.9 shows a sample of subtracted frames of the INT images covering 3 epochs. One can clearly see variable sources changing in brightness between each epoch.

2.5.1 Photometry on Subtracted Frames

The absolute values of the subtracted images were co-added so that they could be put through SExtractor (Bertin and Arnouts, 1996) in order to identify the positions of

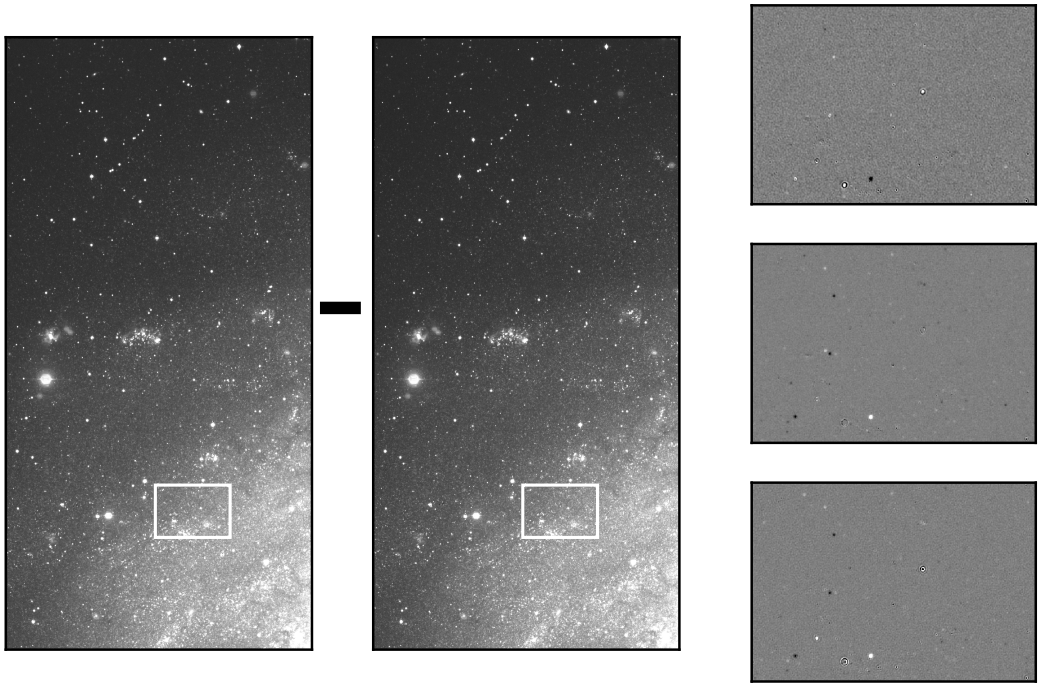

Figure 2.9: Sample of subtracted frames of the INT images covering 3 epochs. One can clearly see variable sources changing in brightness between each epoch.

all the variable objects in each frame. Using this catalogue, aperture photometry was performed on each of the subtracted images in `IRAF` to obtain the flux difference from the template for each and every epoch. An example of a flux difference light curve for a Cepheid folded with a period of 4.95 days is given as Figure 2.10.

The flux differences are then added to the base flux values measured by Kevin Tsang of the stars in the templates giving an equivalent flux value of the star at each epoch producing full flux light curves.

2.6 Calibrating the Light Curves

The flux light curves can now be converted to magnitude light curves using the transformation equations produced by Kevin Tsang as previously described, Equation 2.2.

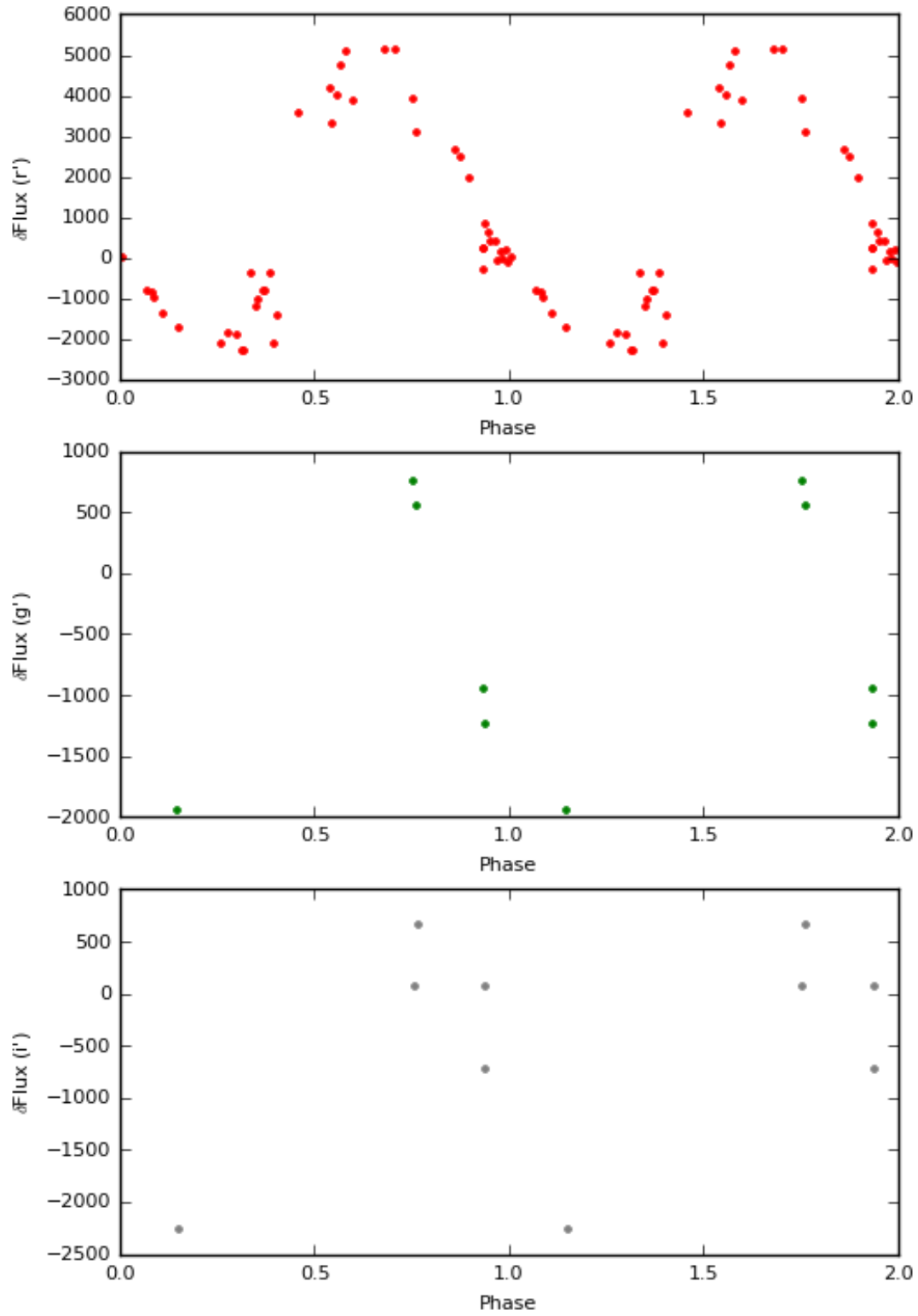

Figure 2.10: Flux difference light curves for an M33 Cepheid folded with a period of 4.95 days in filters r', g' and i'.

The now magnitude calibrated light curves can be merged with the CFHT light curves produced by Hartman et al. (2006). The two sets of light curves are matched by the WCS information for both the CFHT and INT templates and reduced to those that appear in the Cepheid candidate list as described in section 2.2.1.

2.6.1 Cross-Calibration

The CFHT light curves are on a magnitude scale but were not fully calibrated so the magnitudes should be considered to be instrumental. The mean magnitudes of the light curves are taken and used to work out the magnitude offset for each object between the two datasets. Each CFHT chip was calibrated separately by Kevin Tsang. The offset is applied to the CFHT light curves to bring them on to the same magnitude level as the INT light curves. Figure 2.11 shows the now calibrated magnitude folded light curve for the same Cepheid as in Figure 2.10 for each filter, r', g' and i'.

2.6.2 Amplitude Discrepancy

A substantial proportion of the cross-calibrated light curves show a discrepancy in the amplitudes between the INT and CFHT data. An example of this problem is given as Figure 2.12 where the folded light curves of a Cepheid give an amplitude difference between the two datasets of $\sim$0.3 mags.

To test the possible cause of this we checked whether the there had been a mismatching of the the stars between the CFHT and INT data. However, the WCS transformations between the two templates match well as shown in Figure 2.13 with no obvious indication that there was a mismatching of coordinates.

We also checked if the amplitude differences were caused by either each star's position

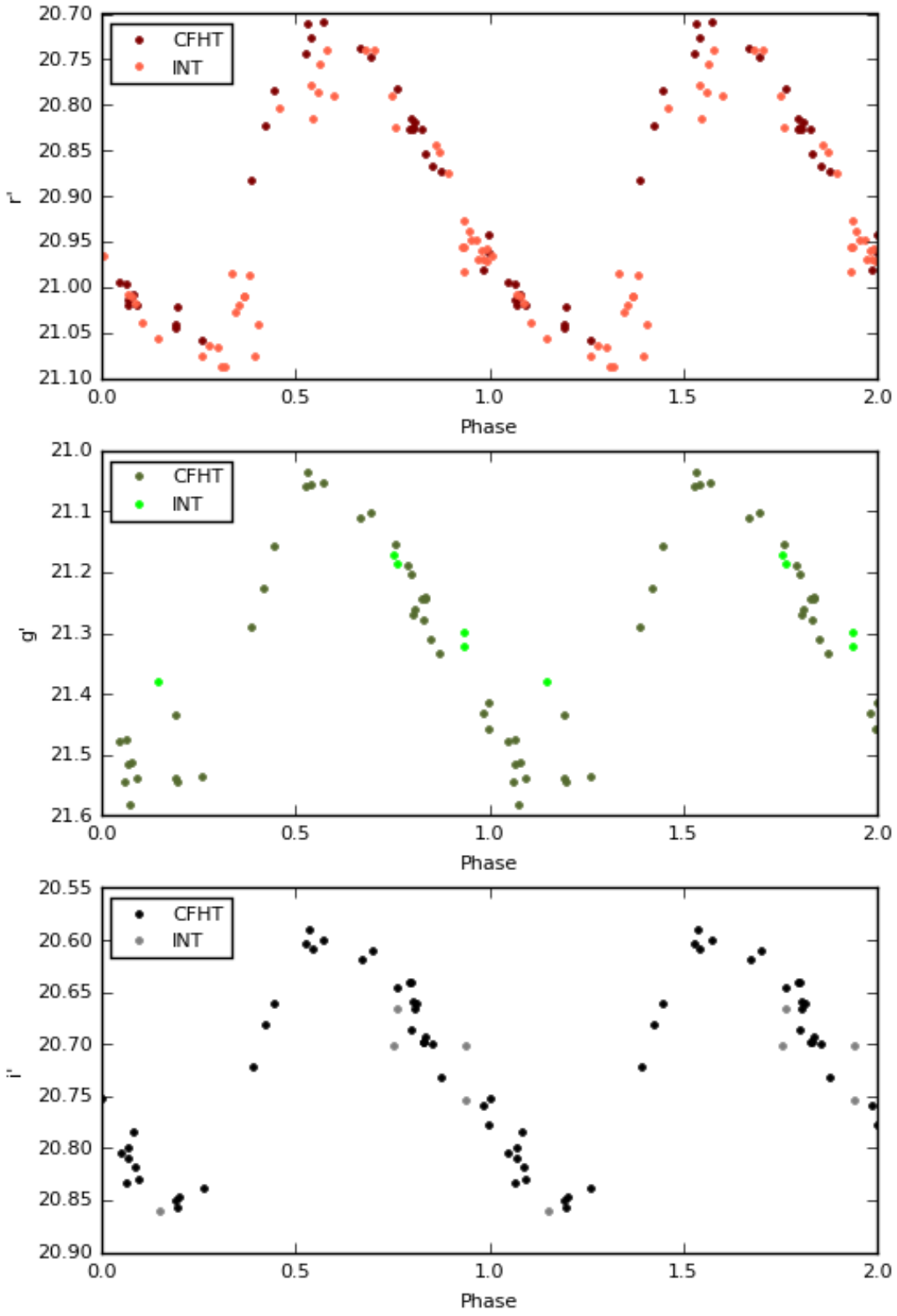

Figure 2.11: Light curves for the same Cepheid in Figure 2.10 with cross-calibrated INT and CFHT magnitudes.

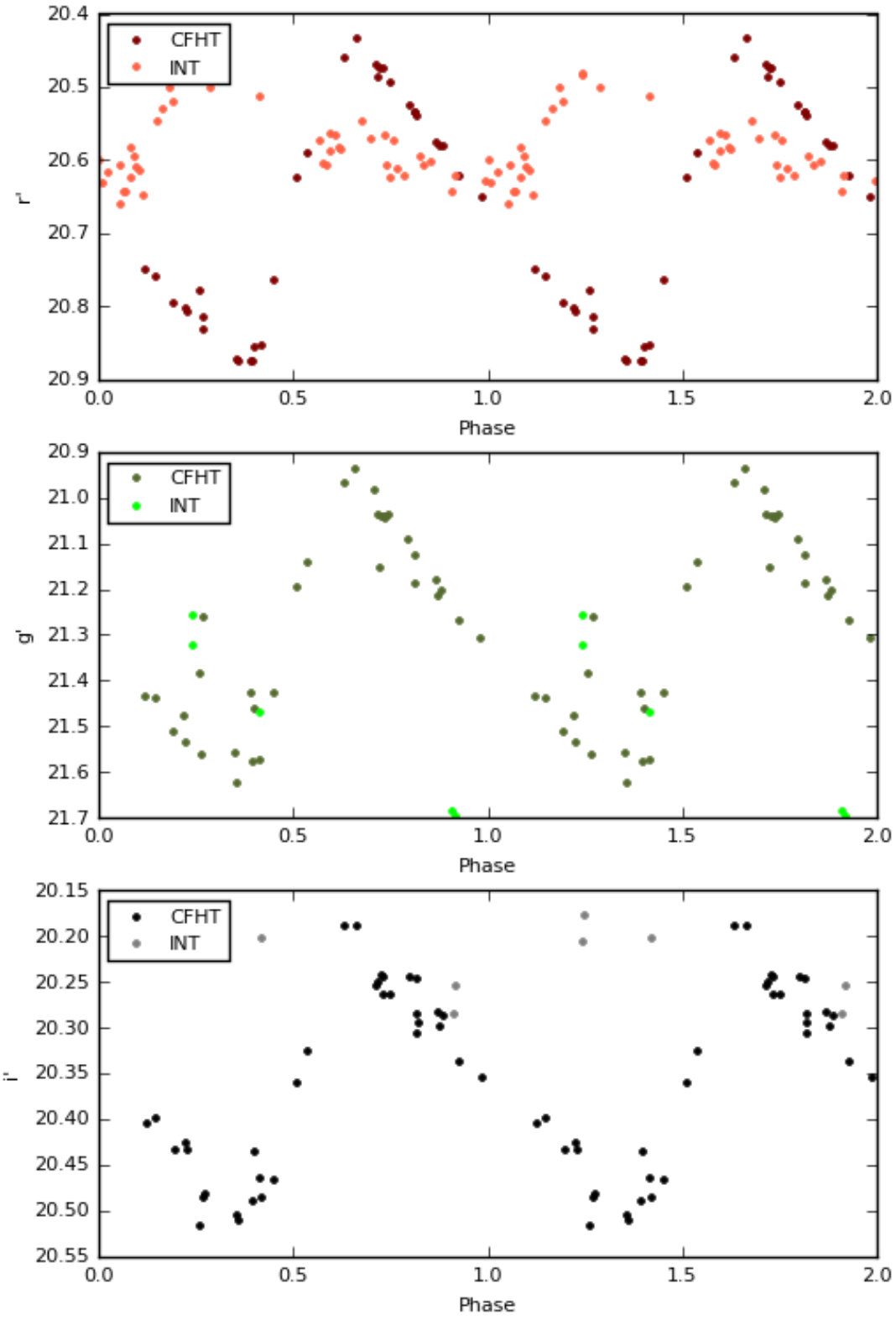

Figure 2.12: Calibrated Light curves showing amplitude difference.

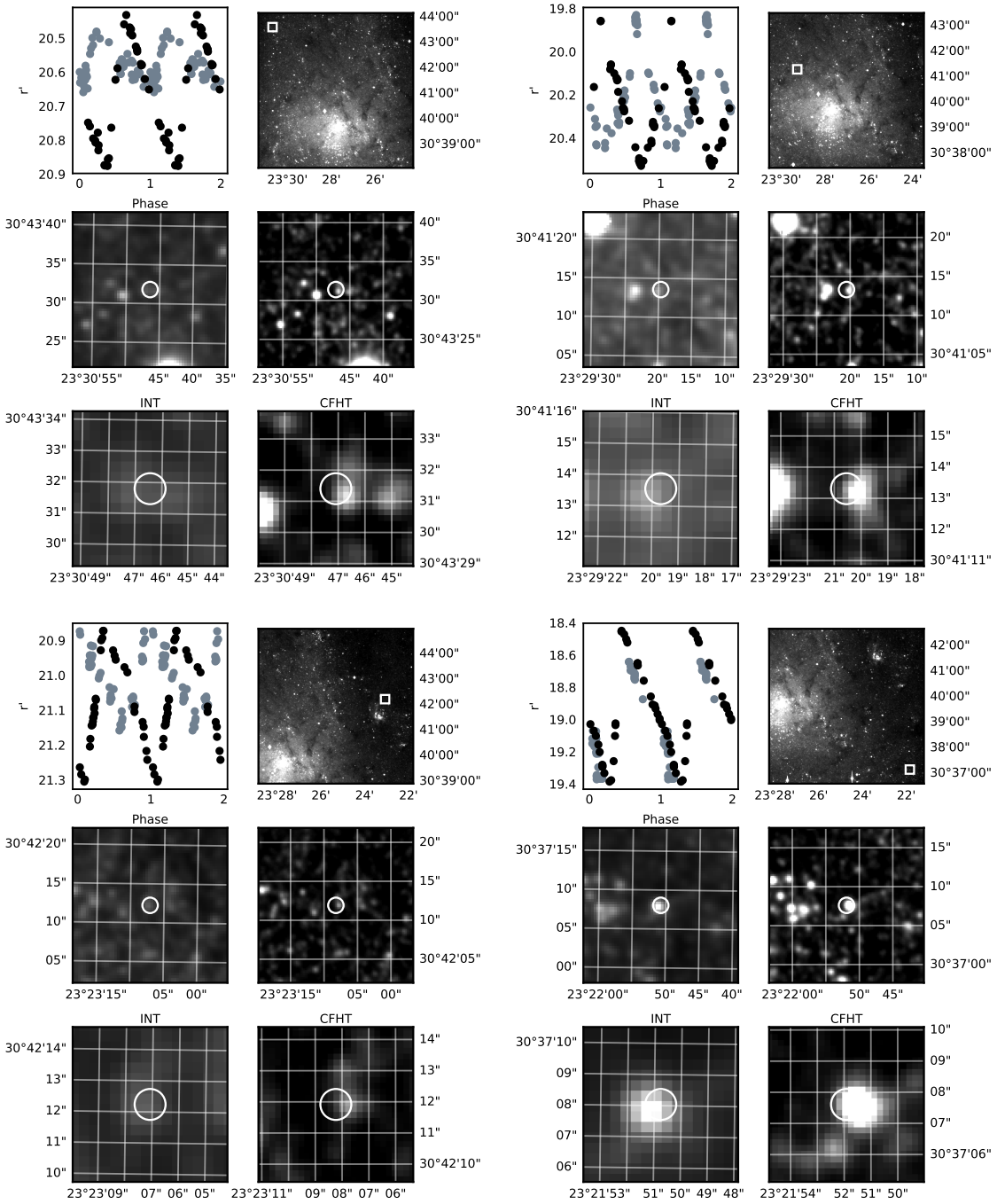

Figure 2.13: Comparison of the WCS coordinate matching between the INT data and the CFHT data. Each quadrant shows a light-curve of a Cepheid with the black spots indicating the CFHT data and the grey spots indicating the INT data. The position of each Cepheid in M33 is shown and zoomed in centered on where the source was detected for both the INT and CFHT data.

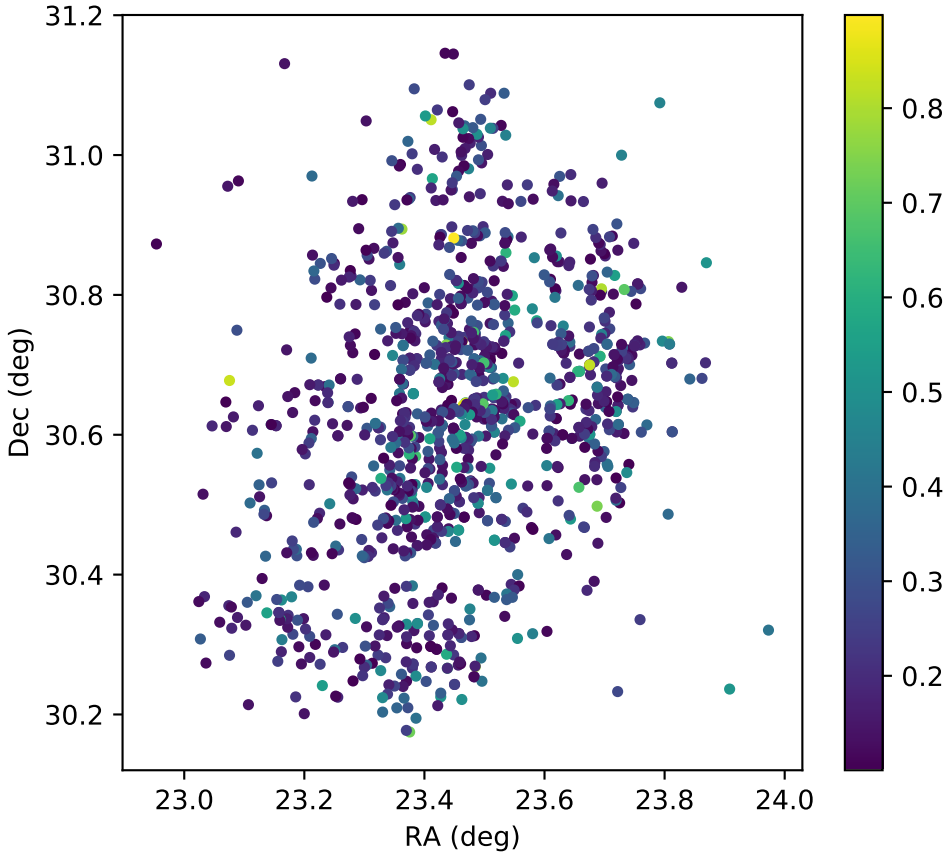

Figure 2.14: Figure showing the positions of the Cepheids that present an amplitude discrepancy between the CFHT and INT data. The colourbar indicates the amplitude difference in mags.

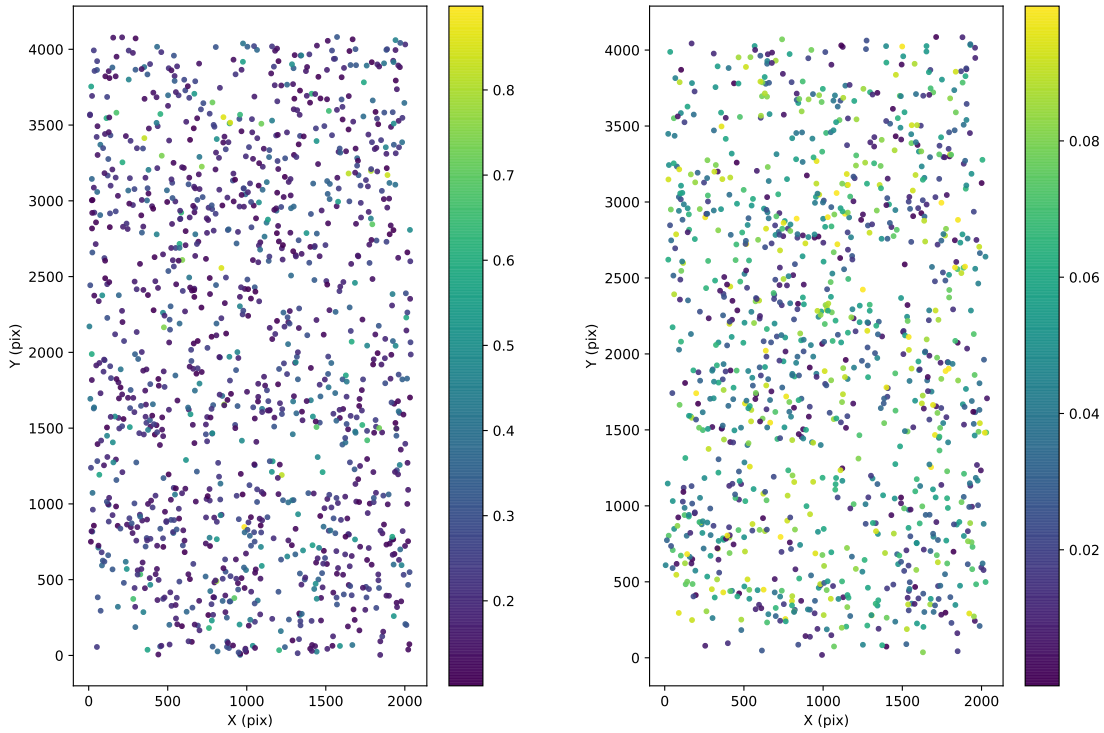

Figure 2.15: Figure showing the INT pixel coordinates for all chips of the Cepheids that present an amplitude discrepancy between the CFHT and INT (the left-hand panel) data as well as those that do not (the right-hand panel). The colourbar indicates the amplitude difference in mags.

in M33 or on each chip. Figure 2.14 shows the positions of the matched Cepheids in M33 that show amplitude differences with the colour scale indicating the r'-band amplitude difference in mags. There does not seem to be any correlation with position in M33.

Figure 2.15 shows the pixel INT pixel coordinates for all chips and all regions in the for Cepheids that present an amplitude discrepancy (the left-hand panel) as well as those where there is no significant amplitude difference in the Cepheid light curves between the INT and CFHT data (the right-hand panel). The distribution of Cepheids in INT chip pixel coordinates is the same for both the problem Cepheids and those that are fine.

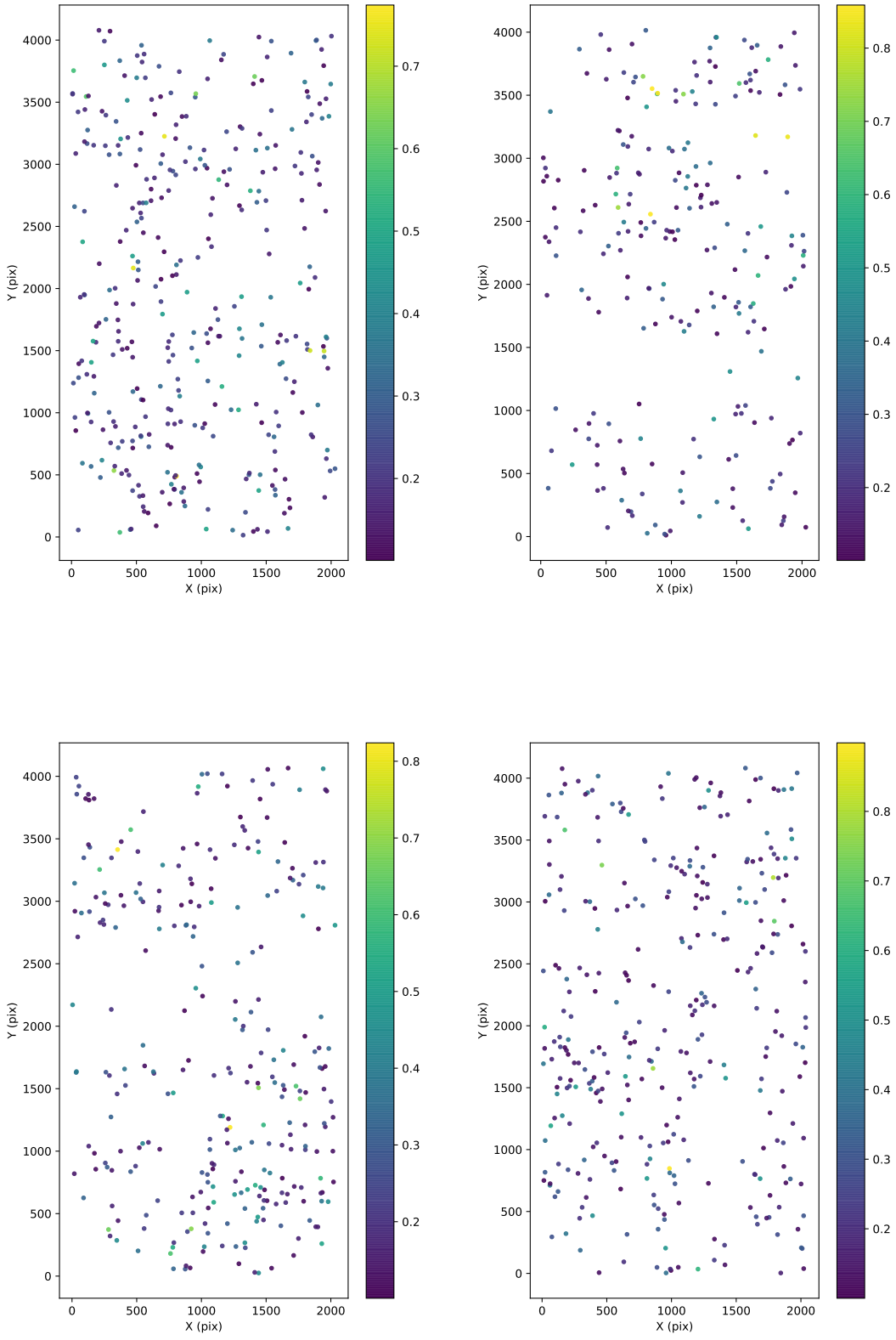

Figure 2.16: Figure showing the INT pixel coordinates for each of the INT chips in turn of the Cepheids that present an amplitude discrepancy. Top-left: Chip 1. Top-right: Chip 2. Bottom-left: Chip 3. Bottom-right:Chip 4. The colourbars indicate the amplitude difference in mags.

Splitting the the INT pixel coordinates into the four separate chips also does not shed any light on the issue. Figure 2.16 shows the INT pixel coordinates of the matched Cepheids for each of the four chips separately with the colour scale indicating the r'-band amplitude difference in mags.

One of the parameters that `HOTPANTS` uses is called `stamps`, the number of stamps in the x and y directions on the chip dictate the sub-regions of each image for which the software calculates a convolution kernel. When performing image subtraction on the INT data the chips were split into two regions along the y-axis, making each frame two 2048×2048 pixel frames. The number of stamps was set to 20 along both the x and y axes making each stamp region 104.2×104.2 pixels. Figure 2.17 shows the pixel coordinates of the matched Cepheids within the sub-stamp-regions for each of the four chips separately with the colour scale indicating the r'-band amplitude difference in mags. There does not seem to be any correlation between the amplitude discrepancy and position inside a sub-stamp-region.

In short, position in M33 or any particular chip is not the cause of the problem. We can also be confident that it is not caused by a WCS problem.

The amplitude discrepancy problem remains unsolved. Therefore, a workaround was devised so that the project could continue. The ratio of the amplitudes were calculated for each light curve. The amplitudes of the CFHT and INT light curves were calculated for each object by finding the difference between the brightest and faintest point. Then the ratio of these values for the INT and CFHT light curves were used as our scaling factors. This ratio was then used to scale the amplitudes of the INT light curves so that they matched the CFHT light curves. This was done by multiplying the magnitudes in each INT light curve by the corresponding amplitude ratio. Figure 2.18 shows the now scaled folded light curve of the same Cepheid as shown in Figure 2.12.

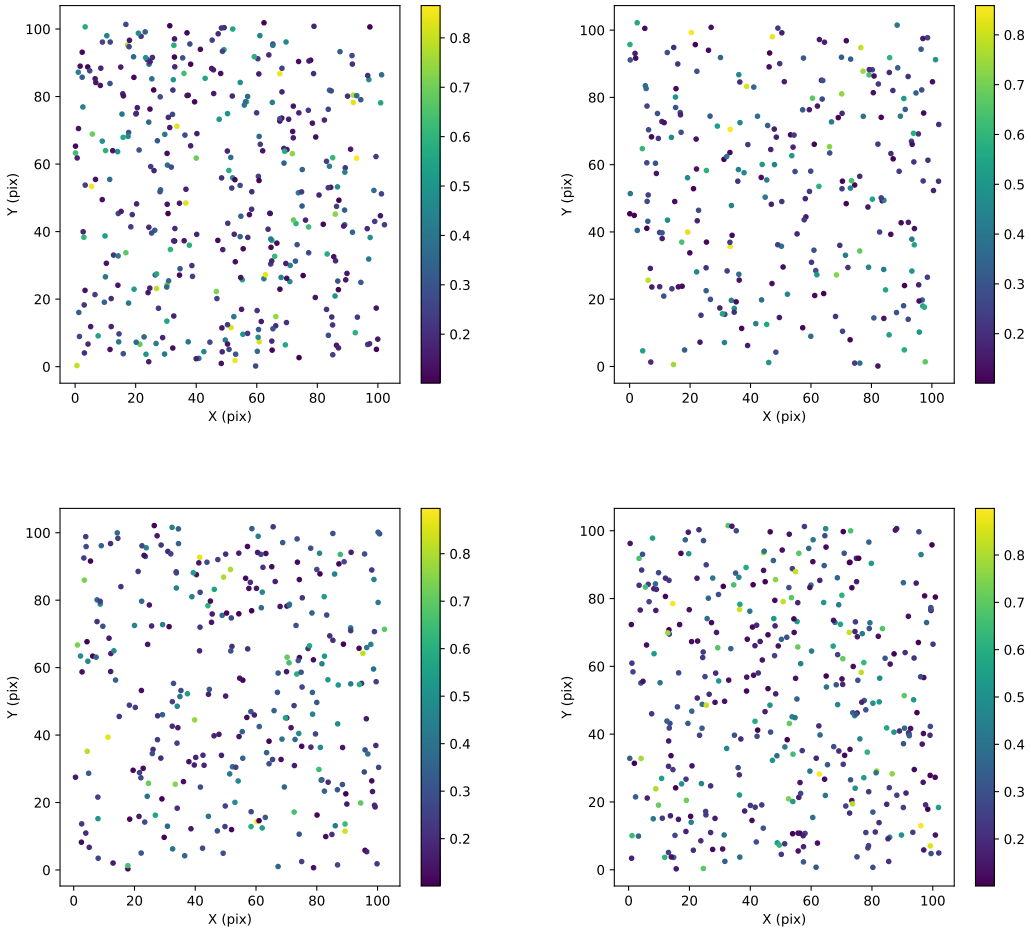

Figure 2.17: Figure showing the INT image subtraction sub-stamp-region pixel coordinates for each of the INT chips in turn of the Cepheids that present an amplitude discrepancy. Top-left: Chip 1. Top-right: Chip 2. Bottom-left: Chip 3. Bottom-right:Chip 4. The colourbars indicate the amplitude difference in mags.

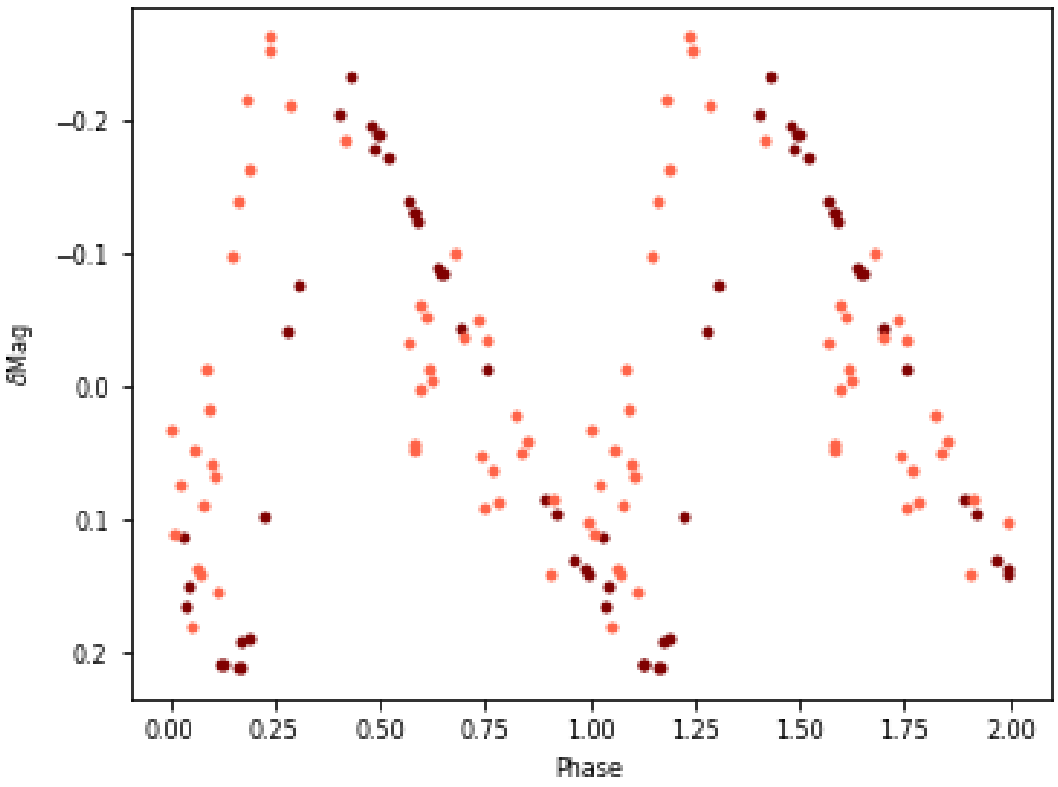

Figure 2.18: Calibrated Light curves showing how amplitude scaling corrects for the discrepancy of the same Cepheid as in Figure 2.12.

Chapter 3

Beat Cepheids in M33

3.1 Beat Cepheids

As discussed in section 1.3.1, Beaulieu et al. (2006) found 5 beat Cepheids from the Hartman et al. (2006) catalogue of variable stars in M33. They used the period ratios of these stars to determine their metallicity thus yielding an M33 metallicity gradient of $\frac{d \log Z}{d\rho} = -0.2$ dex kpc^{-1} or $\frac{d[O/H]}{d\rho} = -0.16$ dex kpc^{-1}. It is extremely difficult to find secondary periods with so few epochs as were available from the CFHT variability survey. Combined with the INT data the number of data-points available have more than doubled meaning that it should be easier to search for Cepheids with more than one period.

Figure 3.1 shows the light curves for the 5 beat Cepheids, labelled A - E, folded by each period from Beaulieu et al. (2006).

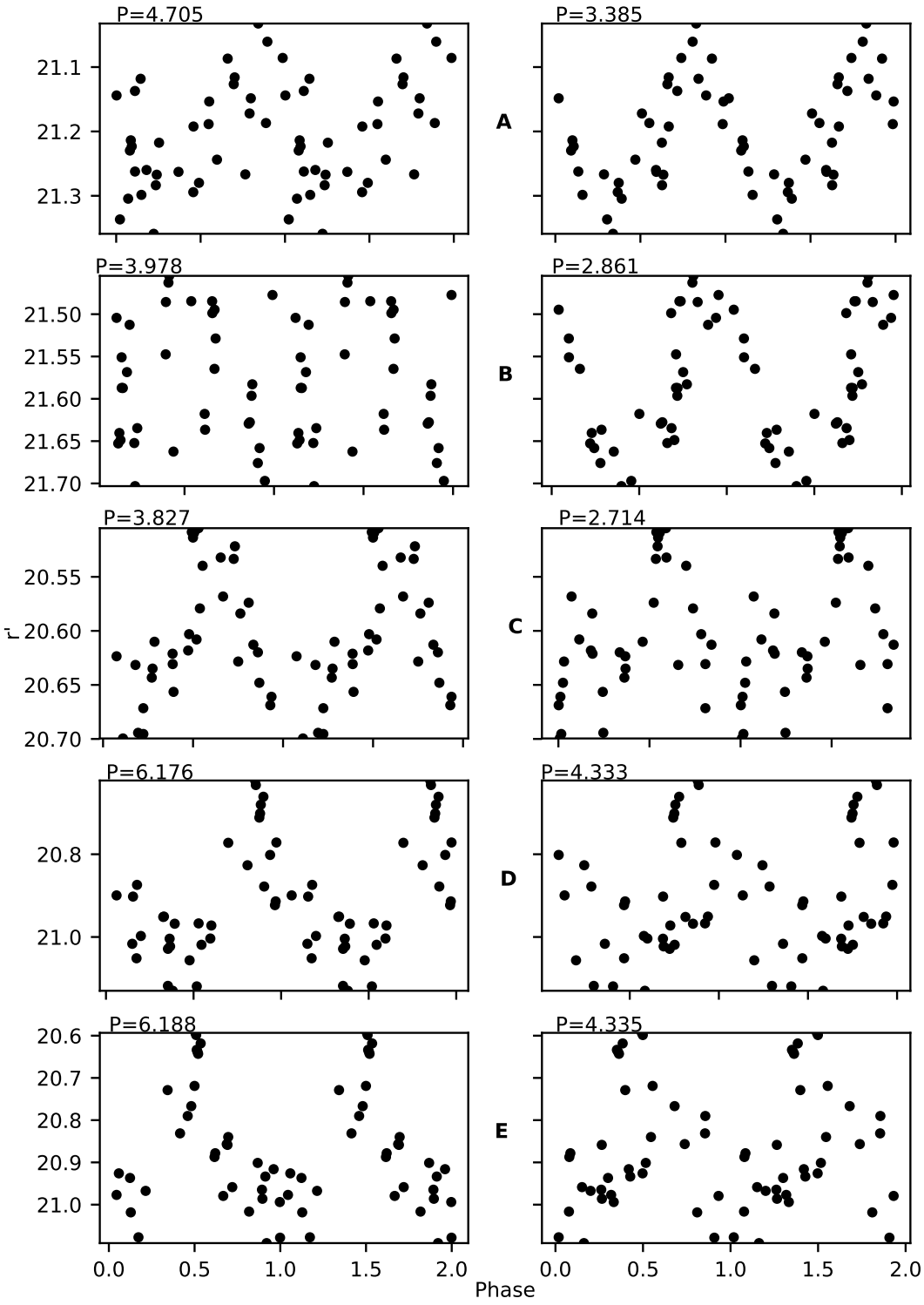

Figure 3.1: Light Curves of the 5 Beat Cepheids in M33 detected by Beaulieu et al. (2006).

3.1.1 Period Search

An Analysis of Variance (AoV) period search was applied to the combined INT and CFHT light curves described in Chapter 2 limited to those that were in the Cepheid candidate list discussed in section 2.2.1. The AoV technique was implemented using `VARTOOLS` (Hartman and Bakos, 2016) based on the method developed by Schwarzenberg-Czerny (1989) and is built upon original code by Devor (2005). This method works by fitting a model that is a discrete set of step functions to the light curve and outputs a periodogram showing peaks representing the most probable periodic signal. When searching for multiple periods, after the first period is found the light curve is 'whitened', as in, the best-fit periodic signal is subtracted from the light curve, the periodogram is recomputed and then the highest peak in the second periodogram is determined to be a subsequent period.

The AoV routine was used on all of the merged INT and CFHT light curves for the stars that are present in the candidate Cepheid list. The period value represented by the top peak from the pre-whitened periodogram of the first pass was taken to be the first period. Then, the periods were extracted from the whitened periodogram of the second pass for the top 3 peaks and only those which would produce a period ratio of somewhere between 0.66 and 0.78 were kept. Of the 3019 candidate Cepheids, 2576 were matched to INT light curves and 302 of those potentially presented more than one period which would produce a suitable period ratio for a Cepheid pulsating in both the fundamental and first overtone modes. Of those 302, 3 Cepheids show promise as to actually being beat Cepheids. Figures 3.2-3.4 show the light curves of the 3 beat Cepheids folded by each period along with the periodograms showing the peaks representing the period values.

Empirical evidence would suggest that Cepheids are more frequent in low metallicity

Table 3.1: Beat Cepheids in M33 from Beaulieu et al. (2006) labelled A - E and from this work labelled BC1 - BC3.

Label	CFHT ID	RA (J2000.0) (hms)	Dec (J2000.0) (dms)	P_0 (days)	P_1 (days)	P_1/P_0
A	120975	01 34 59.73	+30 52 25.2	4.70497	3.38510	0.7195
B	160511	01 32 56.82	+30 41 33.8	3.97755	2.86107	0.7190
C	133288	01 34 33.43	+30 51 15.6	3.82707	2.71407	0.7091
D	234885	01 33 54.63	+30 35 19.8	6.17640	4.33313	0.7015
E	237301	01 34 03.97	+30 38 08.4	6.18792	4.33481	0.7005
BC1	310187	01 34 20.04	+30 20 19.9	3.02646	2.21359	0.7314
BC2	150017	01 33 05.41	+30 52 03.1	2.88962	2.08356	0.7210
BC3	320829	01 33 55.93	+30 18 45.0	3.64967	2.66287	0.7296

environments. In fact, a higher proportion of stars in the low metallicity Magellanic Clouds are Cepheids compared to galaxies with higher mean metallicities such as the Milky Way, M31 and M33. Furthermore, it has been observed that there exists a higher number of Cepheids in the lower metallicity SMC (Z=0.004) than the LMC (Z=0.008) (Lemasle et al., 2017; Udalski et al., 2015), even though it is less massive. The occurrence of beat Cepheids also seems to increase at low metallicity at the same rate as other Cepheids so one would expect to find more beat Cepheids in low metallicity environments. The three new beat Cepheids presented here are all towards the edge of the galaxy where the metallicity is lower and would seem to back this point up. However, with so few beat Cepheids found using this dataset compared to what is expected, we are reluctant to draw any statistical conclusions from this sample.

3.2 Metallicity Gradient Across M33

3.2.1 Period Ratio

The period ratio of a beat Cepheid can be used to determine its metallicity. By using metallicities of stars in the Milky Way and Magellanic Clouds determined by other

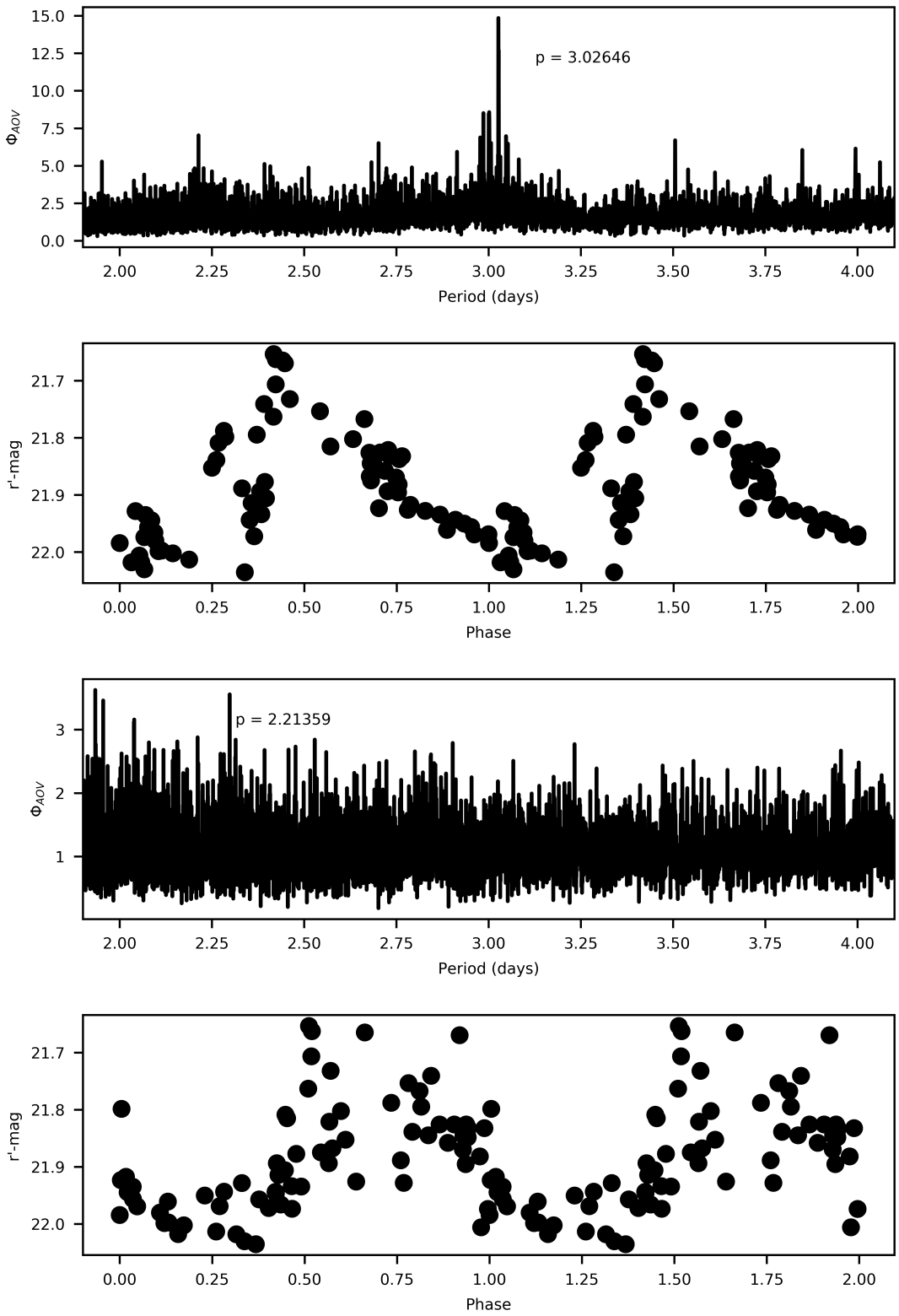

Figure 3.2: Light curves and periodograms for the M33 beat Cepheid designated BC1 in Table 3.1. The first and third panels show periodograms the with periods represented by the peaks that were used to fold the light curves in the second and fourth panels.

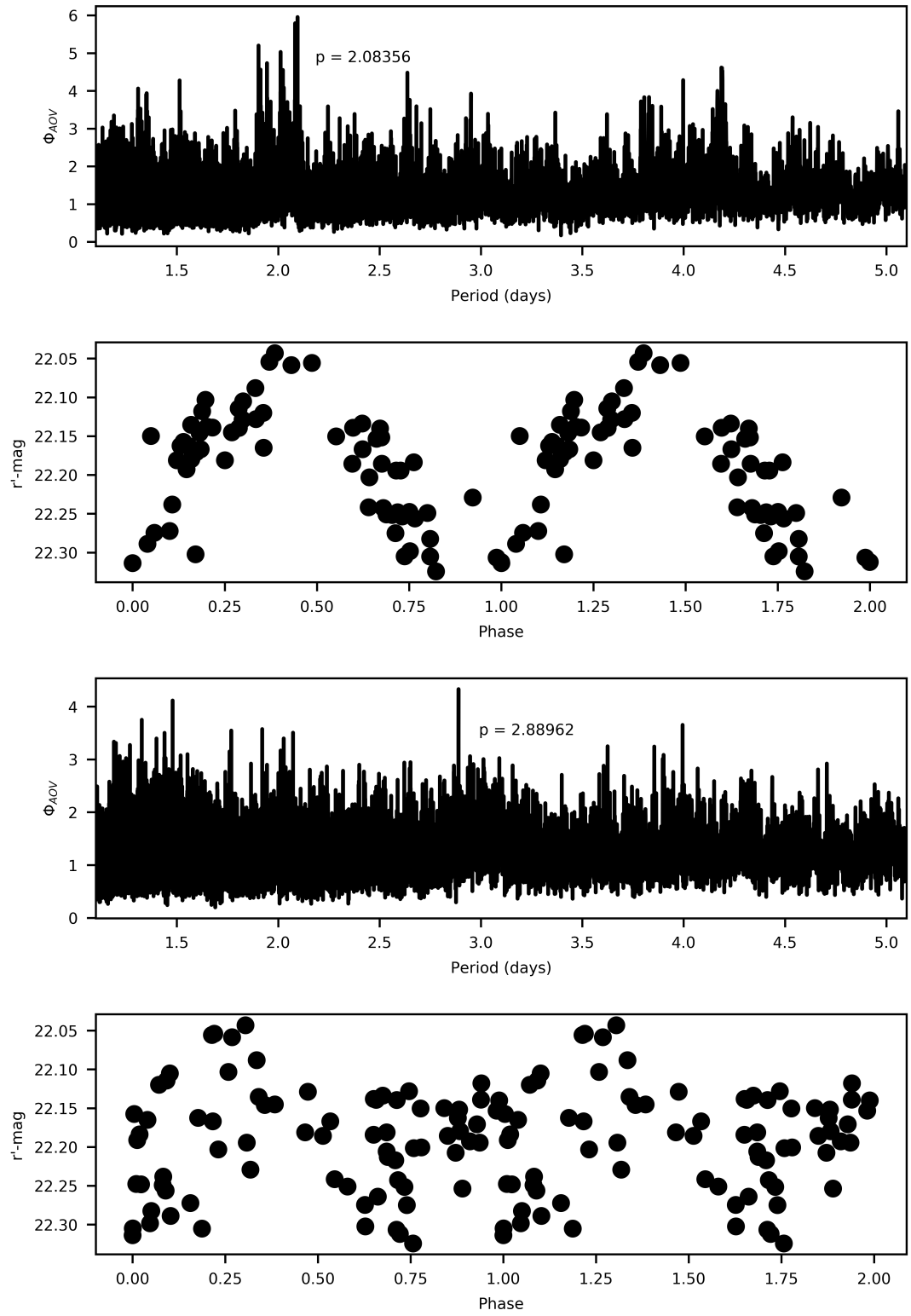

Figure 3.3: Light curves and periodograms for the M33 beat Cepheid designated BC2 in Table 3.1. The first and third panels show periodograms the with periods represented by the peaks that were used to fold the light curves in the second and fourth panels.

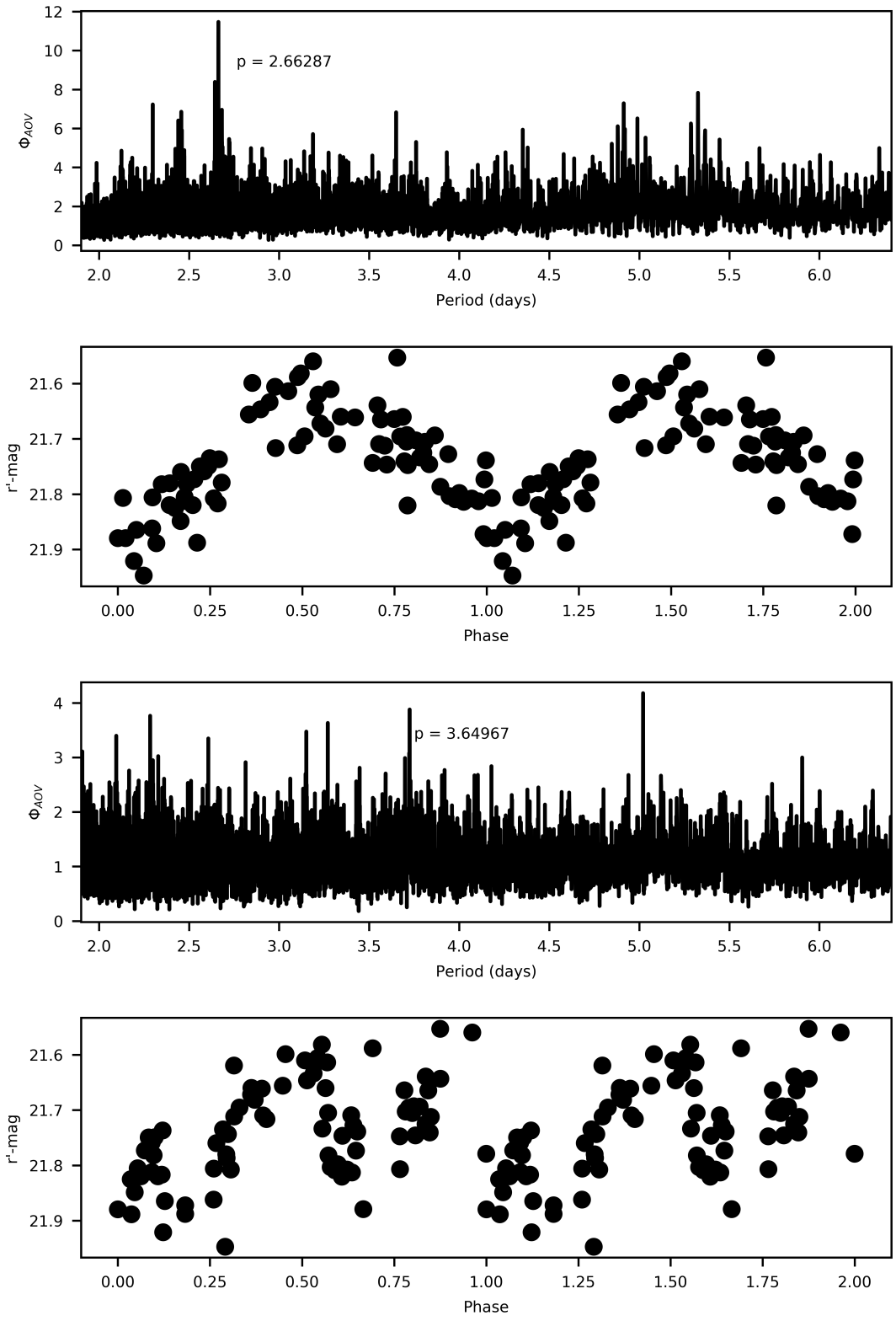

Figure 3.4: Light curves and periodograms for the M33 beat Cepheid designated BC3 in Table 3.1. The first and third panels show periodograms the with periods represented by the peaks that were used to fold the light curves in the second and fourth panels.

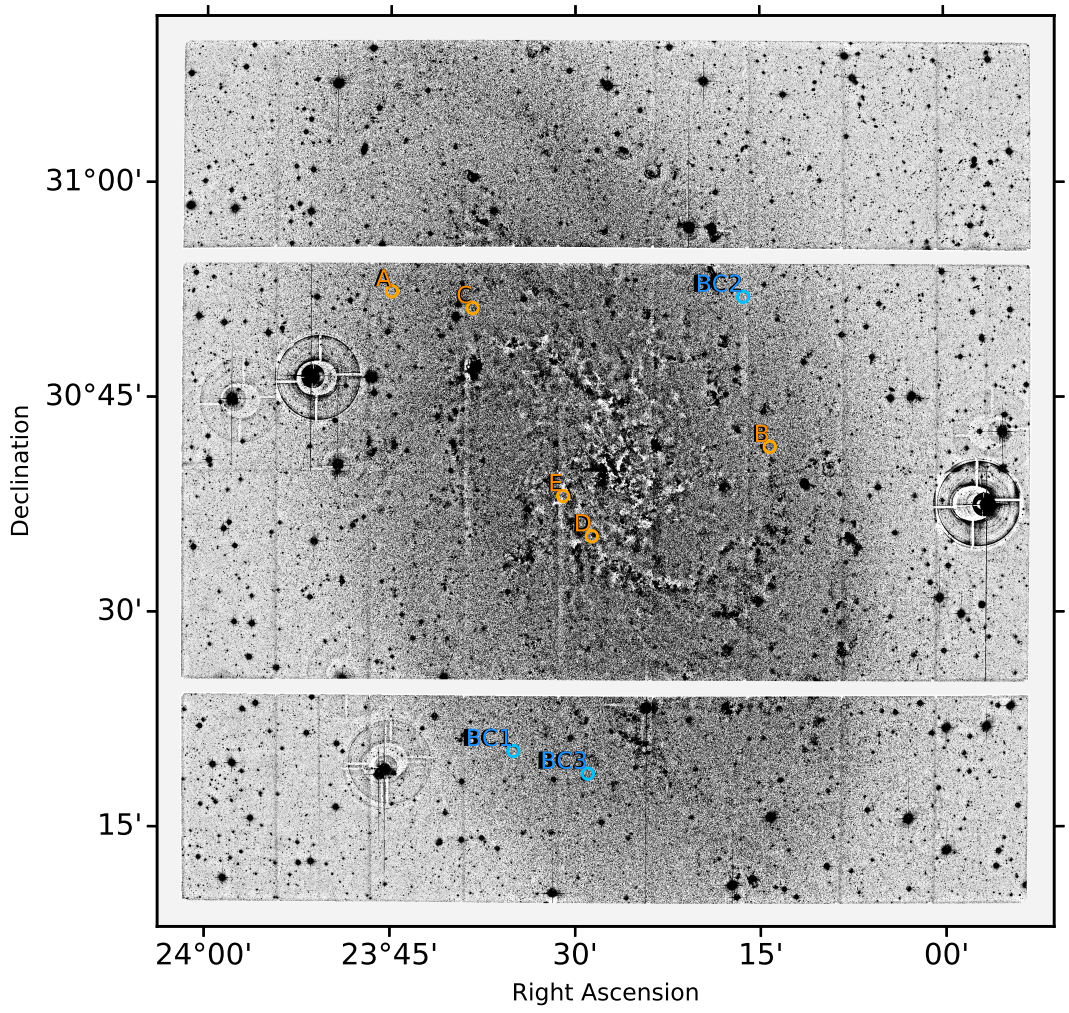

Figure 3.5: Positions of Beat Cepheids in M33

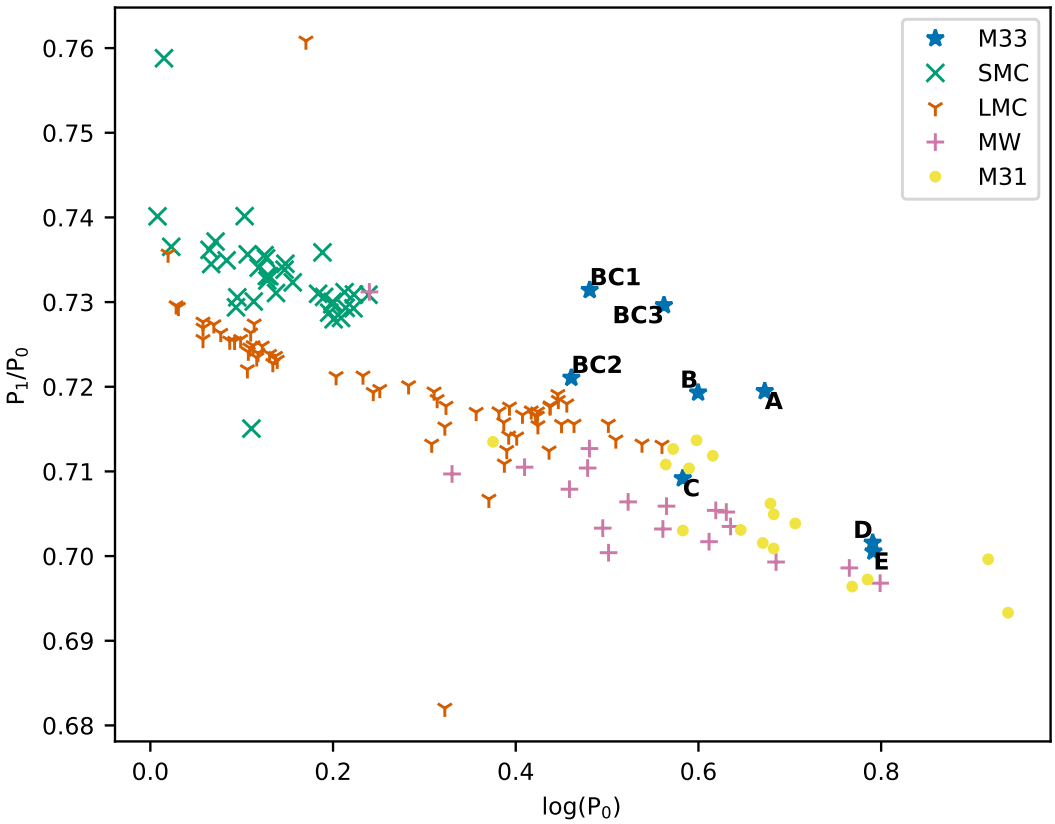

Figure 3.6: Petersen Diagram for M33 compared with other galaxies.

methods, a relation between beat Cepheid period ratio and metallicity can be determined.

3.2.2 Petersen Diagram

As discussed in section 1.3.1, a Petersen diagram plots the ratio of the fist overtone and fundamental periods (P_1/P_0) of a beat Cepheid against the logarithm of the fundamental period ($\log(P_0)$). By plotting beat Cepheids found in M33 with beat Cepheids of known metallicity in the Milky Way (Z=0.020), LMC (Z=0.008) and SMC (Z=0.004) on a Petersen diagram comparisons can be made to determine the metallicity of the M33 beat Cepheids as in Figure 1.9. A Petersen diagram with the 3 new beat Cepheids discovered in this work is presented here as Figure 3.6.

3.2.3 Beat Cepheid Metallicities

The equivalent metallicities of the beat Cepheid period ratios are determined using equations from Sziládi et al. (2007), Equation 3.1, and Kovtyukh et al. (2016), Equation 3.2. Sziládi et al. (2007) and Kovtyukh et al. (2016) used high resolution spectroscopy to determine the metallicities of Galactic beat Cepheids. Kovtyukh et al. (2016) found [Fe/H] abundances higher than reported by Sziládi et al. (2007). Kovtyukh et al. (2016) reasoned this was due to Sziládi et al. (2007) using set grid points for values of effective temperature and gravity in their stellar models whereas Kovtyukh et al. (2016) interpolated between grid point values within the models. This has lead to determining a shallower gradient from the Kovtyukh et al. (2016) relation than from the Sziládi et al. (2007) relation. The metallicities of the beat Cepheids found in M33 as a function of period ratio from both the Sziládi et al. (2007) and Kovtyukh et al. (2016) relations are presented in Figure 3.7 along with the same for beat Cepheids in the SMC, LMC, Milky Way and M31.

$$\frac{P_1}{P_0} = -0.0143 \log P_0 - 0.0265[Fe/H] + 0.7101 \tag{3.1}$$

$$\frac{P_1}{P_0} = -0.0239 \log P_0 - 0.0404[Fe/H] + 0.7187 \tag{3.2}$$

From Figure 3.7 we can see that the metallicity range covered by the beat Cepheids found in M33 is approximately 1 dex. If a steep metallicity gradient exists across M33 then this would be expected. The Milky Way and M31 are thought to also show metallicity gradients but metallicity range covered by beat Cepheids in the Milky Way and M31 is less than in M33. This could be because stellar populations in the Milky Way and M31 have a lower range in metallicities than M33 or it could be for observational

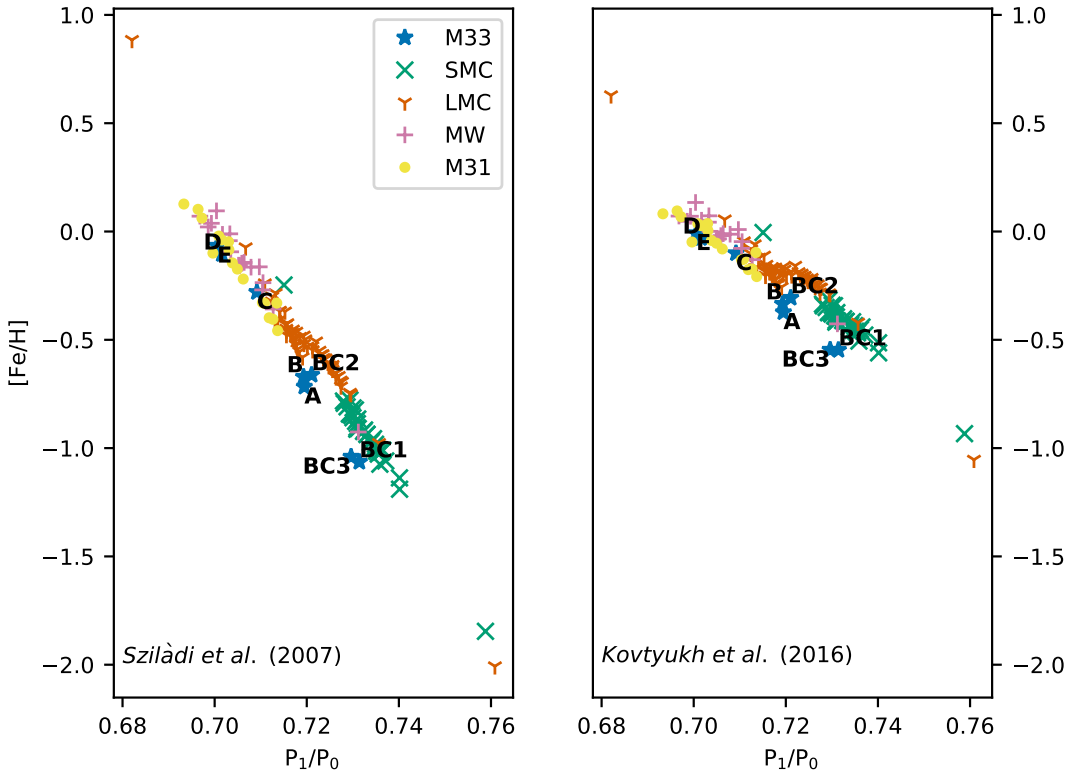

Figure 3.7: [Fe/H] abundances a function of period ration.

reasons as outlined at the beginning of Chapter 2. As in, the fact the large parts of the Milky Way are obscured from our view and that M31 has a high inclination angle means that maybe beat Cepheids have not been found at the same range of radii, from their respective galactic centres, than in M33. The same observational problems do not exist for the Magellanic Clouds, yet, the range in beat Cepheid metallicities, excluding outliers, is approximately 0.5 dex for both the SMC and LMC. There is no evidence however to suggest that there is much of a metallicity gradient across either of the Magellanic Clouds. Therefore, one would expect the metallicity range covered by beat Cepheids to be fairly narrow for both the SMC and LMC.

The galactocentric distances of the beat Cepheids are derived by deprojecting their celestial coordinates with an inclination angle of 53° and a position angle of 22° at a distance of 840 kpc (Scowcroft et al., 2009). The deprojected distances can be found

Table 3.2: Metallicities of Beat Cepheids in M33 from Beaulieu et al. (2006) labelled A - E and from this work labelled BC1 - BC3.

Label	P_1/P_0	Distance (kpc)	[Fe/H] (Sziládi et al., 2007)	[Fe/H] (Kovtyukh et al., 2016)
A	0.7195	5.586	-0.717	-0.373
B	0.7190	4.718	-0.671	-0.334
C	0.7091	3.857	-0.280	-0.101
D	0.7015	1.304	-0.105	-0.031
E	0.7005	1.282	-0.066	-0.008
BC1	0.7314	6.510	-1.064	-0.547
BC2	0.7210	5.897	-0.662	-0.306
BC3	0.7296	5.847	-1.040	-0.546

in Table 3.2 alongside the equivalent metallicities corresponding to the period ratios of the beat Cepheids. Figure 3.8 shows the metallicity gradients derived from M33 beat Cepheids with metallicities determined from the Sziládi et al. (2007) and Kovtyukh et al. (2016) equations.

The [Fe/H] values can be converted to 12+[O/H] using Equation 3.3 from Maciel et al. (2003). Maciel et al. (2003) derived the [Fe/H] to [O/H] from spectra of Galactic disk stars.

$$[Fe/H] = 0.0317 + 1.4168[O/H] \tag{3.3}$$

The metallicity gradients determined in this work as shown in Figure 3.8 are presented as the following equations. Equation 3.4 shows the [Fe/H] gradient with metallicities determined from the Sziládi et al. (2007) equation and equivalent [O/H] gradient, Equation 3.5, converted using the equation from Maciel et al. (2003).

$$\frac{d[Fe/H]}{d\rho} = -0.175\ dex\ kpc^{-1} \tag{3.4}$$

$$\frac{d[O/H]}{d\rho} = -0.124\ dex\ kpc^{-1} \tag{3.5}$$

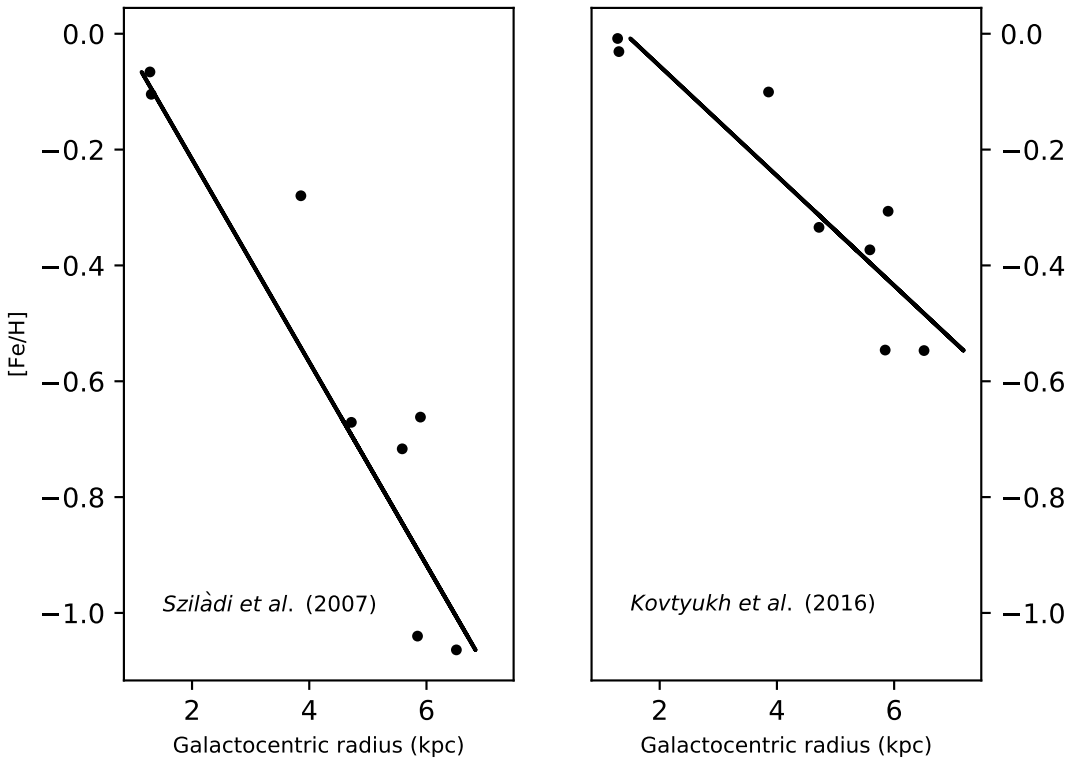

Figure 3.8: [Fe/H] abundances a function of galactocentric radius.

The metallicity gradients determined in this work as shown in Figure 3.8 are presented as the following equations. Equation 3.6 shows the [Fe/H] gradient with metallicities determined from the Kovtyukh et al. (2016) equation and equivalent [O/H] gradient, Equation 3.7, converted using the equation from Maciel et al. (2003).

$$\frac{d[Fe/H]}{d\rho} = -0.095\ dex\ kpc^{-1} \tag{3.6}$$

$$\frac{d[O/H]}{d\rho} = -0.067\ dex\ kpc^{-1} \tag{3.7}$$

As can be seen in Table 3.3 the metallicity gradients found from using Beat Cepheids are steeper than most of the gradients found by recent studies of HII regions with the exception of Garnett et al. (1997). The gradient determined from blue supergiants by

Table 3.3: M33 metallicity gradient estimates.

Metal	Gradient (dex kpc^{-1})	Tracer	Distance (kpc)	Source
12+[O/H]	-0.11	HII regions	840	Garnett et al. (1997)
12+[O/H]	-0.034	HII regions	832	Willner and Nelson-Patel (2002)
12+[O/H]	-0.012	HII regions	832	Crockett et al. (2006)
12+[O/H]	-0.05	HII regions	840	Viironen et al. (2007)
12+[O/H]	-0.027	HII regions	840	Rosolowsky and Simon (2008)
12+[O/H]	-0.033	HII regions	840	Bresolin (2011)
12+[O/H]	-0.024	HII regions	840	Magrini et al. (2016)
12+[O/H]	-0.024	HII regions	878	Lin et al. (2017)
12+[O/H]	-0.031	PNe	840	Magrini et al. (2009)
12+[O/H]	-0.06	Blue supergiants	820	Urbaneja et al. (2005)
[Fe/H]	-0.08	AGB	840	Cioni (2009)
[Fe/H]	-0.07	RGB	916	Kim et al. (2002)
[Fe/H]	-0.06	RGB	867	Tiede et al. (2004)
[Fe/H]	-0.175	Beat Cepheids	840	This work with Sziládi et al. (2007)
[Fe/H]	-0.095	Beat Cepheids	840	This work with Kovtyukh et al. (2016)
12+[O/H]	-0.124	Beat Cepheids	840	This work with Sziládi et al. (2007)
12+[O/H]	-0.067	Beat Cepheids	840	This work with Kovtyukh et al. (2016)

Urbaneja et al. (2005) is in line with the gradient determined using the Kovtyukh et al. (2016) relation but not as steep as the gradient using the Sziládi et al. (2007) relation.

The slope of the metallicity gradient of a galaxy is dependent on age of the tracers used (Genovali et al., 2014). Beasley et al. (2015) measured the metallicity of stellar clusters within the disc of M33 and binned them into age groups. They found that the M33 disc metallicity gradient is steepest when measured with the oldest clusters and flattens with younger clusters. HII regions are younger than the beat Cepheids used for our gradient so it is not necessarily unexpected that we would measure a steeper gradient than from spectroscopy of HII regions. The metallicity gradient measured from blue supergiants by Urbaneja et al. (2005) is similar to ours which is not surprising as they also used individual stars to trace metallicity. Large spiral galaxies tend to show metallicity gradients like M33 (Zaritsky et al., 1994). Genovali et al. (2014) used high resolution high SNR spectroscopy to measure the iron abundances of 42

Galactic Cepheids. From these, they measured a metallicity gradient of 0.06 ± 0.002 dex kpc^{-1} across the thin disk of the Milky Way. The Milky Way metallicity gradient measured from Galactic Cepheids is similar to the metallicity gradients measured from beat Cepheids and blue supergiants for M33. This suggests that the two galaxies are similar in structure with similar histories. Therefore, studying M33 could help us to understand the star formation history of the Milky Way.

3.3 Effect of metallicity on Leavitt Law

Metal-poor Cepheids are fainter than metal-rich Cepheids at a given pulsation period, which has a effect on the zero-point of the Leavitt Law but not the slope (Scowcroft et al., 2009). Metallicity corrections are required to produce an accurate distance modulus from the Leavitt Law. Tsang et al. (submitted) found that using the shallower HII region derived metallicity gradients lead to excessively large metallicity corrections implying that a steeper metallicity gradient exists in M33 such as the one found by Urbaneja et al. (2005) from blue supergiants or from this work.

Chapter 4

LMC Cepheid Period-Age Relation

4.1 Stellar Cluster in the Large Magellanic Cloud

4.1.1 Observations

As explained in the introduction (Chapter 1), there exists a period-age (PA) relation for Cepheid variable stars. To determine this observationally we used data for 8 young massive clusters in the LMC. Young stellar clusters in the Magellanic Clouds are key for the calibration of the Cepheid PA relation as they are host to a large number of Cepheids. The Magellanic Clouds have been extensively covered by microlensing experiments such as OGLE (Udalski et al., 2015) finding thousands of Cepheids. Also, stellar clusters in nearby galaxies can be observed across the entirety of a galaxy, this allows for the understanding of their spatial distribution within the host galaxy (Kharchenko et al., 2012). Differentiating which stars are cluster members from field stars also becomes more difficult when looking within the Milky Way (Schmeja et al., 2014), this means that Magellanic Cloud clusters have more well-defined main-sequences and so are easier to age using isochrones. As well as that, the

number of Cepheids per cluster observed in our own galaxy is far fewer than for Magellanic Cloud clusters and because clusters have a non-negligible period range then the mean Cepheid period for Galactic clusters will be off. On top of this, the LMC contains many Cepheid rich young clusters making it ideal for the calibration of the Cepheids PA relation (Efremov, 2003). NGC 1866 in particular, plays host to many Cepheids and has long been used to investigate Cepheid properties (Lemasle et al., 2017) and test pulsation models (Bono and Marconi, 1997).

Our observations cover $\sim$45 epochs per cluster with both V and I Bessell filters. The observations were taken using the 2 m Faulkes Telescope South[1] at the Siding Spring node of the Las Cumbres Observatory in New South Wales, Australia. The data covers 2 observing runs, the first taking place from October 2013 until February 2014 supplying $\sim$15 observations with an exposure time of 15 s and used the Merope Camera. The second ran from October 2015 until February 2016 supplying $\sim$30 observations with an exposure time of 30 seconds and used the Spectral Camera. Each of the clusters with the full fields of view are shown in Figure 4.1. A full table of the data collected showing the number of images per cluster on each observing night is included as appendix A. As the two datasets are of different exposure times and were taken with different cameras they need to be cross-calibrated which is discussed later in this chapter. Of the 8 clusters 6 were suitable to be used for this work. The cluster NGC 1831 is too old to host Cepheids and we did not find any Cepheids in cluster NGC 1856.

[1]Initial capital and operational funding for the Faulkes Telescope South was provided by The Dill Faulkes Educational Trust. Faulkes Telescope South is now operated by Las Cumbres Observatory as a component of the Las Cumbres Observatory Global Telescope Network.

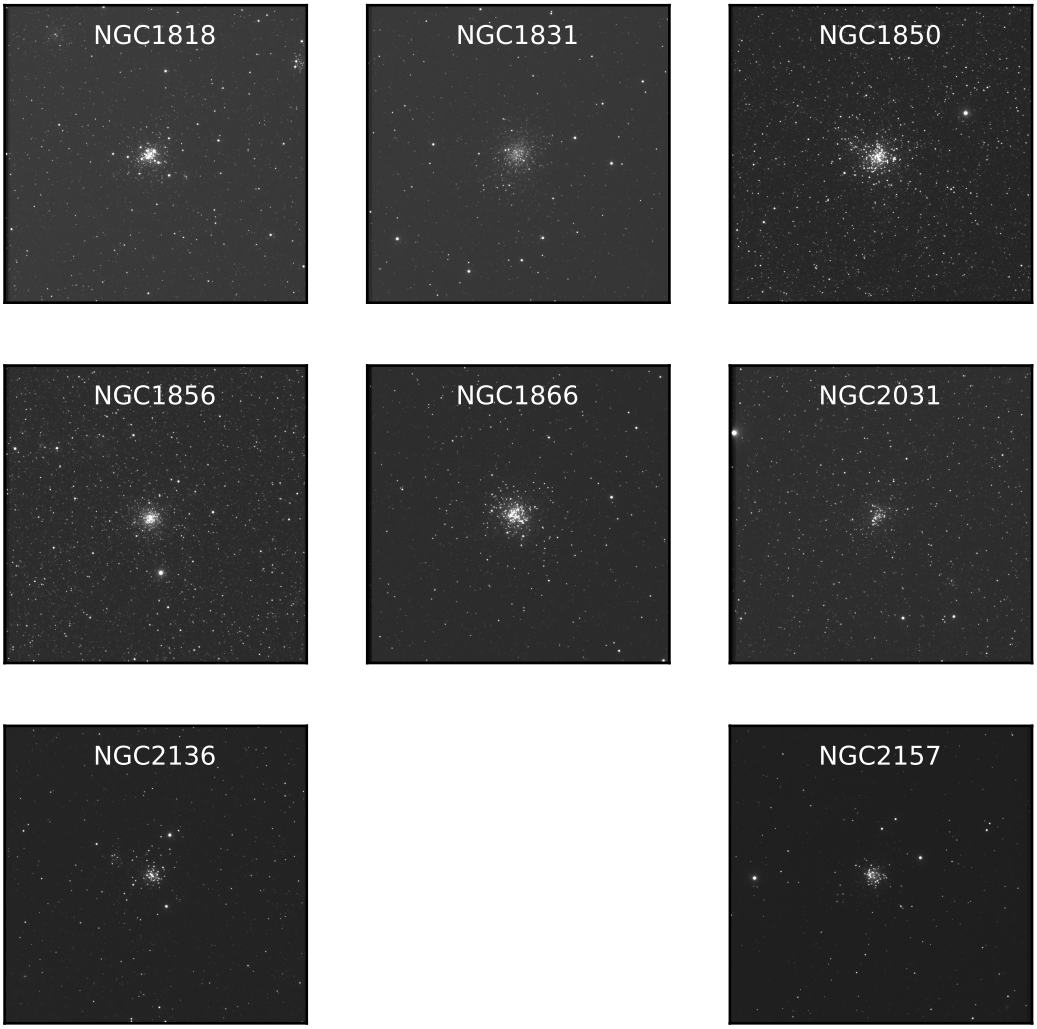

Figure 4.1: The full fields of view for each of the LMC clusters in this dataset.

4.1.2 Measuring the Ages of Clusters

The ages for each of the clusters were taken from literature as shown in Table 4.1 with the exception of NGC 2031 as the most recent age estimation we came across was from Mould et al. (1993) so we enlisted the help of another student to obtain a more accurate value. The age was determined from Isochrone fitting and comparison with other clusters by Silvia Martocchia using HST photometry. As can be seen if Figure 4.2 the MS turn-off magnitude for NGC 2031 is brighter than that of NGC 1856 meaning it is safe to say it is younger. In fact, the MS turn-off magnitude for NGC 1856 is $\sim$17.5 and $\sim$17.0 for NGC 2031, if compared to the younger NGC 1866 whose MS turn-off occurs at $\sim$16.5 the age of NGC 2031 can be estimated to be somewhere between these two other clusters. This leads to NGC 2031 being assigned an age of $\sim$230 Myrs with the error estimated to be $\pm$30 Myrs from the measured magnitude difference across the MS at the turn-off.

The ages of the other clusters were taken from various sources. The age of NGC 1818 was determined by Ahumada et al. (2019) who compared the cluster's spectrum to that of LMC cluster templates presented in Santos et al. (1995). The ages of the remaining clusters were determined using isochrone fitting (see section 1.4.2). For NGC 1831, NGC 2136 & NGC 2157 see Niederhofer et al. (2015). For NGC 1850 & 1866 see Milone et al. (2018). For NGC 1856 see Bastian and Silva-Villa (2013).

The age of each of the clusters is presented in Table 4.1 as well as the number of Cepheids that we selected from each cluster and the range of Cepheid periods found in each cluster. The method of period determination and my selection criteria will be discussed later in this chapter. Figure 4.3 shows the range of periods of the four clusters that contain multiple fundamental mode Cepheids.

The ages of the clusters in our sample has an affect the zero-point of the empirical PA

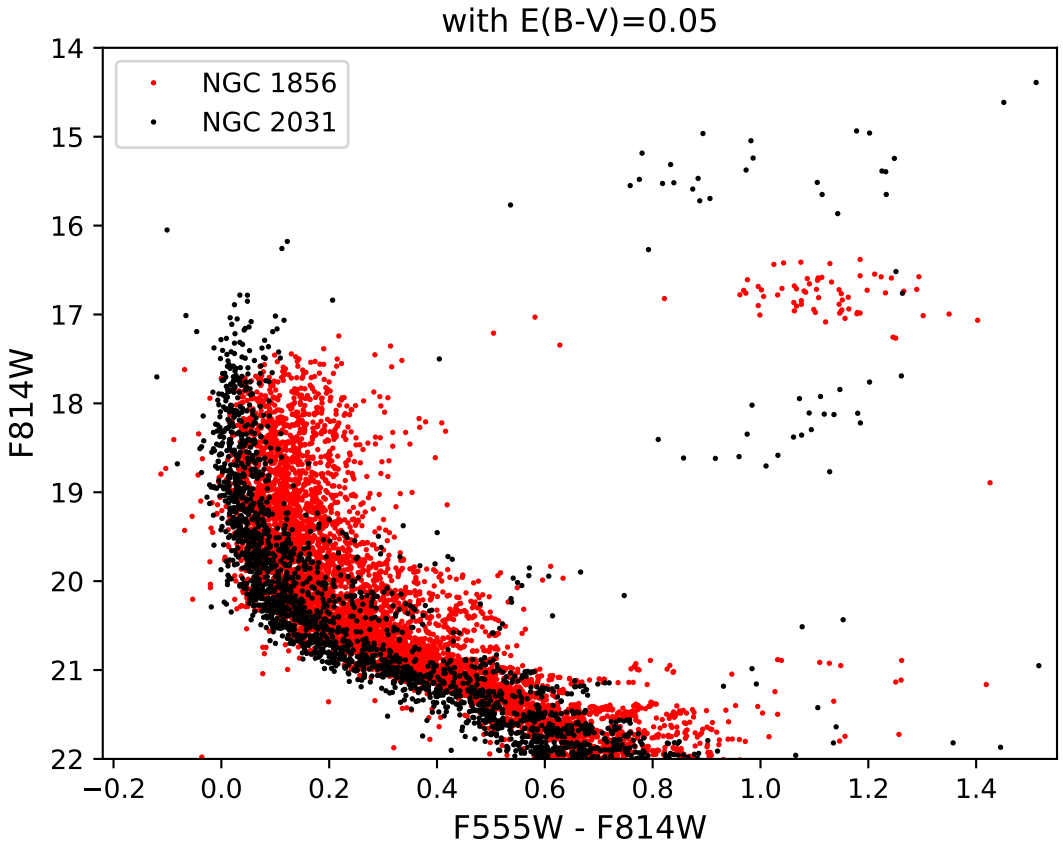

Figure 4.2: Comparison of the CMDs of NGC 2031 to NGC 1856 from HST photometry. Produced by Silvia Matocchia.

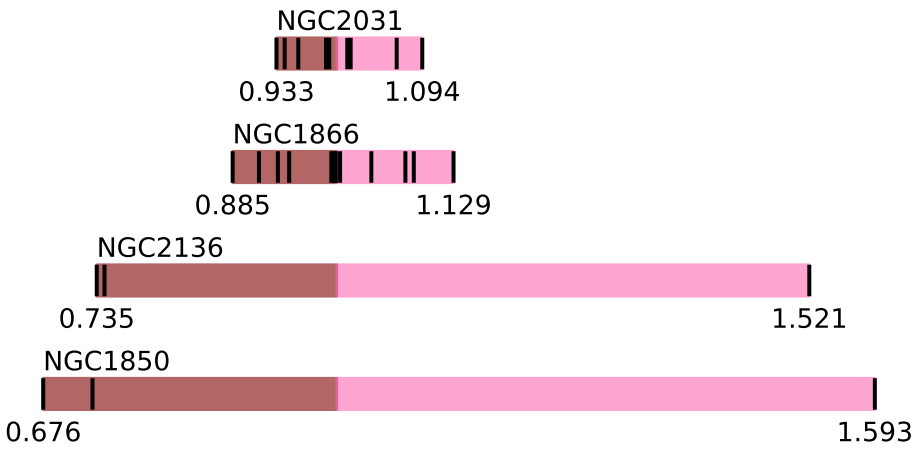

Figure 4.3: Figure showing the period ranges of four of the clusters normalised to the mean, with higher and lower period populations separated.

Table 4.1: The age, number of Cepheids, period range and the half-light radius (r_h) for each cluster.

Cluster	Age (Myrs)	No. of Cepheids	Period range (days)	r_h (arcsec)
NGC 1818	30±15[a]	1	40	24.0[f]
NGC 1831	924±126[b]	0	-	
NGC 1850	80±17[c]	2+1*	7.92 - 18.66	38.9[f]
NGC 1856	280±50[d]	0	-	
NGC 1866	200±75[c]	11+2*	2.71 - 3.45	49.7[g]
NGC 2031	230±30[e]	7+2*	2.8 - 3.28	59.6[g]
NGC 2136	125±50[b]	2+1*	4.41 - 9.13	14.8[f]
NGC 2157	100±30[b]	1+1*	5.15-7.72	26.3[f]

* Overtone pulsator
[a] Ahumada et al. (2019)
[b] Niederhofer et al. (2015)
[c] Milone et al. (2018)
[d] Bastian and Silva-Villa (2013)
[e] This work
[f] Pasquato and Bertin (2010)
[g] Noyola and Gebhardt (2007)

relation. Therefore, we are relying on the authors of the papers referenced in 4.1 to have thoroughly investigated all factors and provide accurate cluster ages. The age of each cluster is derived from some variant of the method of isochrone fitting. There are no uncertainties provided for the isochrones as they are built from stellar evolution models based upon theory. The error of the cluster age comes from cluster parameters that affect which isochrone fits the cluster the best on the CMD, chiefly, the distance modulus, reddening and metallicity. In the case of NGC 2157, Niederhofer et al. (2015) report an age of 100±30 Myr using models fitted to HST photometry of the cluster by Fischer et al. (1998). They used a distance modulus of μ = 18.5, the data was corrected for a reddening value of $E(B-V)$ = 0.1 and the models used were for a stellar population of the adopted LMC metallicity of z = 0.008. In Figure 4.4 we investigate how altering these parameters would affect the age one would determine. Plot A in Figure 4.4 shows a CMD of NGC 2157 using the Fischer et al. (1998) photometry with μ = 18.5 and Geneva `SYCLIST` stellar isochrones (Georgy et al., 2013b)

of different ages overplotted. The isochrones are for a metallicity of z = 0.006 as this is the closest to LMC metallicity that they provide and for a stellar population with an average rotation rate of ω = 0.5. As we can see the isochrone with an age of 100 Myr fits the MS turn-off of the cluster the best. For plot B the we reduced the distance modulus to μ = 18.0, this makes the cluster seem older with the MS turn-off falling between isochrones of $\sim$125-150 Myr. Increasing the distance modulus would make the cluster seem younger. Fischer et al. (1998) applied the reddening correction using values outlined in Holtzman et al. (1995). For plot C we changed the reddening to $E(B-V)$ = 0.05 and altered the extinction and colour correction in accordance with Holtzman et al. (1995). This makes the stars in NGC 2157 redder and the absolute magnitudes fainter with the $\sim$125 Myr isochrone now providing the best fit for the MS turn-off. Increasing the value of $E(B-V)$ would have the opposite effect. In plot D we investigate the effect metallicity has on isochrones, the higher the metallicity the brighter the 'hook' in the isochrone indicating the transition from Hydorgen burning in the core to the shell. Increasing metallicity also makes the RGB redder and fainter. From this we can see how using an incorrect metallicity could cause a misjudgement in determining a cluster's age.

4.1.3 Data Reduction

The images were initially processed through the `ORAC-DR` pipeline which performs bad-pixel masking, bias and dark subtraction, and flat-field corrections. To align the images we used `IRAF` to match stellar coordinates, compute the coordinate transforms and finally register the images.

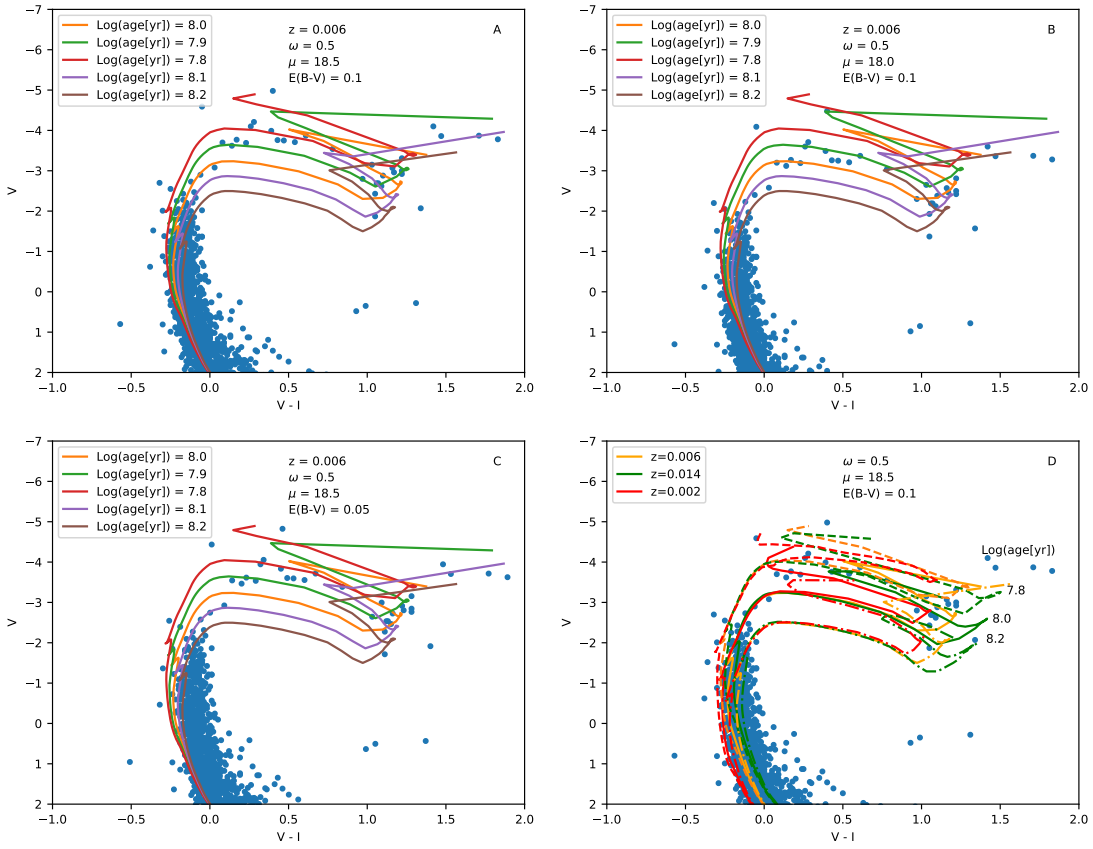

Figure 4.4: CMDs of NGC 2157 using Fischer et al. (1998) photometry to investigate how altering cluster parameters affects isochrone age. Plot A shows a CMD with μ = 18.5 and Geneva SYCLIST stellar isochrones (Georgy et al., 2013b) of 5 different ages overplotted. Plot B is the same but with the distance modulus reduced to μ = 18.0. Plot C is the same but with the reddening changed to $E(B-V) = 0.05$ and the extinction and colour correction altered in accordance with Holtzman et al. (1995). Plot D is the same as plot A but with isochrones of 3 different metallicities at 3 different ages.

Table 4.2: Non-default HOTPANTS (Becker, 2015) parameters used for image subtraction.

[-r rkernel]	11	convolution kernel half width
[-nrx xregion]	1	number of image regions in x dimension
[-nry yregion]	1	number of image regions in y dimension
[-nsx xstamp]	20	number of each region's stamps in x dimension
[-nsy ystamp]	20	number of each region's stamps in y dimension
[-ko kernelorder]	2	spatial order of kernel variation within region
[-bgo bgorder]	2	spatial order of background variation within region

4.2 Image Subtraction

In order to find the variable stars and produce light curves we used image subtraction. Therefore, we created template images to get reference frames with high a signal-to-noise ratio. The templates were produced by selecting images from nights with the best seeing and averaging them together. The images from each epoch are then subtracted in turn from its corresponding template producing a series of subtracted frames with light and dark spots indicating objects that have fluctuated in magnitude. We used the image subtraction software HOTPANTS (Becker, 2015) which is based on the ISIS image subtraction package (Alard and Lupton, 1998; Alard, 2000). An example of a template image, single epoch image and resulting subtracted frames is shown in Figure 4.5. For further details in image subtraction see 2.5 and the HOTPANTS (Becker, 2015) parameters that were changed from default values for the image subtraction are presented in Table 4.2.

4.3 Light Curves

4.3.1 Calibration

Now that we have flux difference light curves for each of the variable objects and the positions and periods of all the Cepheids we need to cross-calibrate the two datasets in

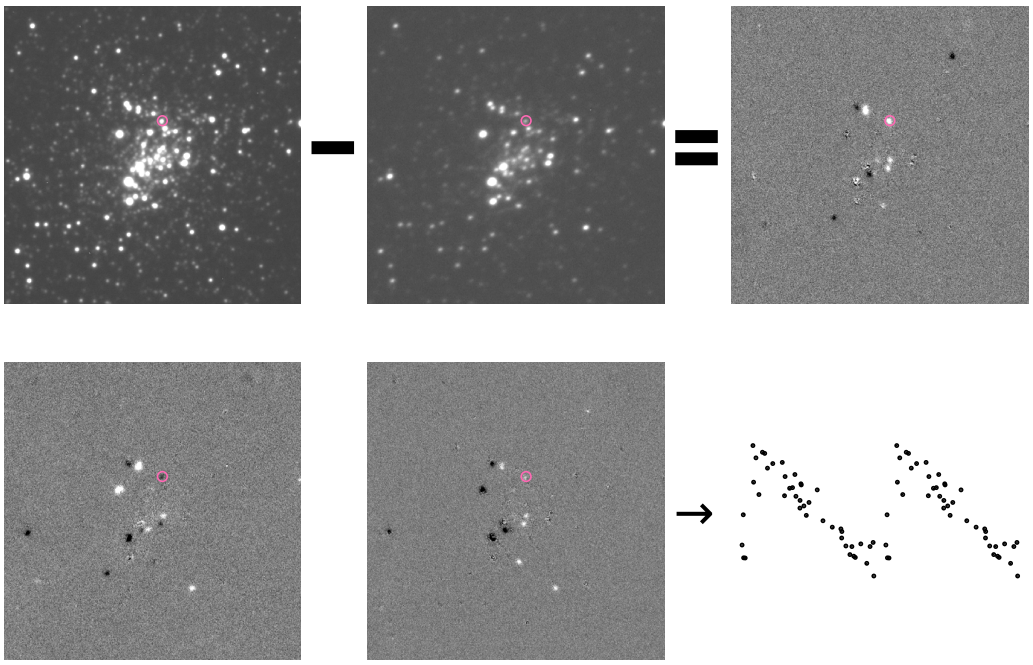

Figure 4.5: Image subtraction on LMC clusters

Table 4.3: Non-default `IRAF` `PHOT` parameters used for photometry.

FWHMPSF	4.
SIGMA	3.6
EPADU	8.14
READNOISE	11.18
ANNULUS	15.
DANNULUS	10.
SMAXITER	10
SNREJECT	50

order to get magnitude light curves on the same scale. The more recent dataset includes a larger number of images as well as a longer exposure time therefore producing templates with a greater depth of view. For this reason we used the photometry on the stars in the templates produced from the second observing run to produce a catalogue. The `PHOT` parameters that were changed from default values within `IRAF` are presented in Table 4.3. The photometry of the stars from the templates of the first observing run were then matched to the catalogue with transformation equations being produced including a magnitude offset and a colour term.

Table 4.4: Parameters of LMC cluster photometry where mI=I+I1+I2(V-I) & mV=V+V1+V2(V-I)

Cluster	No. of stars	I1	I2	V1	V2
NGC 1818	262	0.712±0.002	0.011±0.002	1.153±0.003	0.021±0.003
NGC 1850	239	-0.308±0.003	0.003±0.002	-0.815±0.003	0.013±0.002
NGC 1866	263	0.594±0.002	0.007±0.003	1.639±0.002	0.013±0.004
NGC 2031	303	0.364±0.005	0.008±0.003	0.085±0.005	0.008±0.003
NGC 2136	281	0.169±0.003	-0.001±0.003	0.573±0.003	0.007±0.004
NGC 2157	248	-0.205±0.005	0.010±0.003	-1.054±0.005	0.027±0.003

$$mI = -2.5 \log F + I1 + I2(V - I) \tag{4.1}$$

$$mV = -2.5 \log F + V1 + V2(V - I) \tag{4.2}$$

Where the F is the Flux of the star as measured by `IRAF` for the I-band in Equation 4.1 and the V-band in Equation 4.2. I1 & V1 are the offsets calculated by `IRAF` when the parameters are fitted in the I-band and V-band respectively. I2 & V2 are the coefficients of the colour correction calculated by `IRAF` when the parameters are fitted in the I-band and V-band respectively. The values of I1, I2, V1 and V2 are presented in Table 4.4.

4.3.2 Period Search

To find Cepheids in the data we co-added the absolute values of all of the subtracted frames for each field so that all of the variable objects appeared as bright points in the images. We then used `SExtrator` to find sources. Now that the variable sources have been identified flux difference light curves can be obtained by performing aperture photometry on the subtracted frames. Using a Phase Dispersion Minimisation (PDM) method as decribed by Stellingwerf (1978) on each of the light curves gave me a period

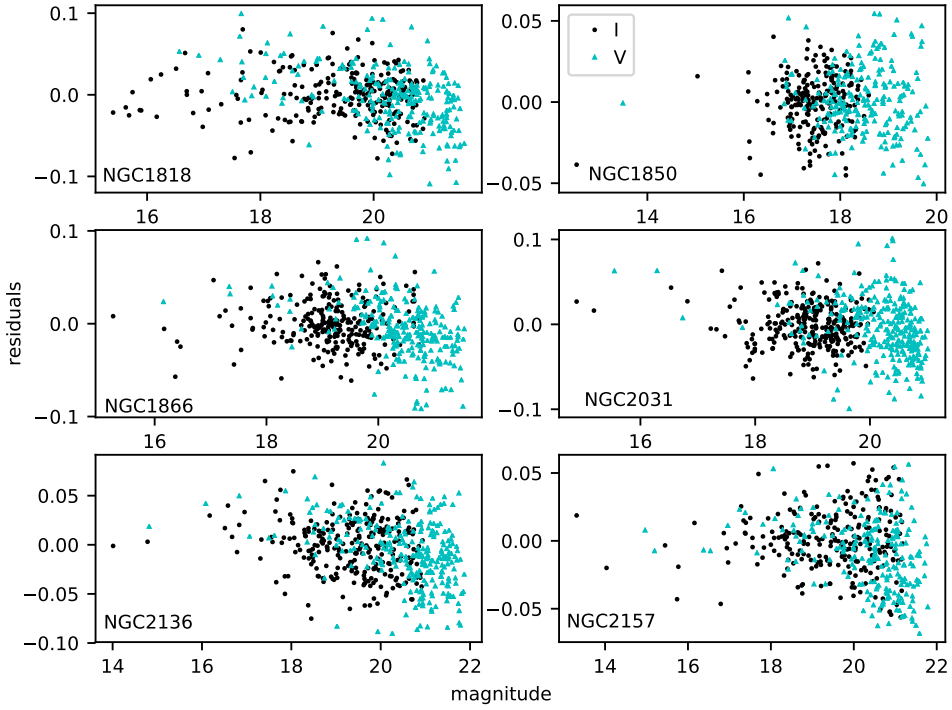

Figure 4.6: Residuals of cross-calibration of the two datasets for each of the LMC clusters.

for each object. We then folded each light curve by each period and checked them by eye to see which were true variable stars and which were not. The periods of each of the Cepheids we found were then compared to known Cepheids which also served to highlight any new Cepheids that we found.

4.4 Cluster Membership

We found many variable objects in each of the fields we have but we only want Cepheids and only those that we can be confident are cluster members. The number of sources detected in the co-added absolute values of the subtracted frames for each cluster are presented in Table 4.5. The first rejection of stars was done by determining which Cepheids lie within the half light radius for each cluster. The half light radii of

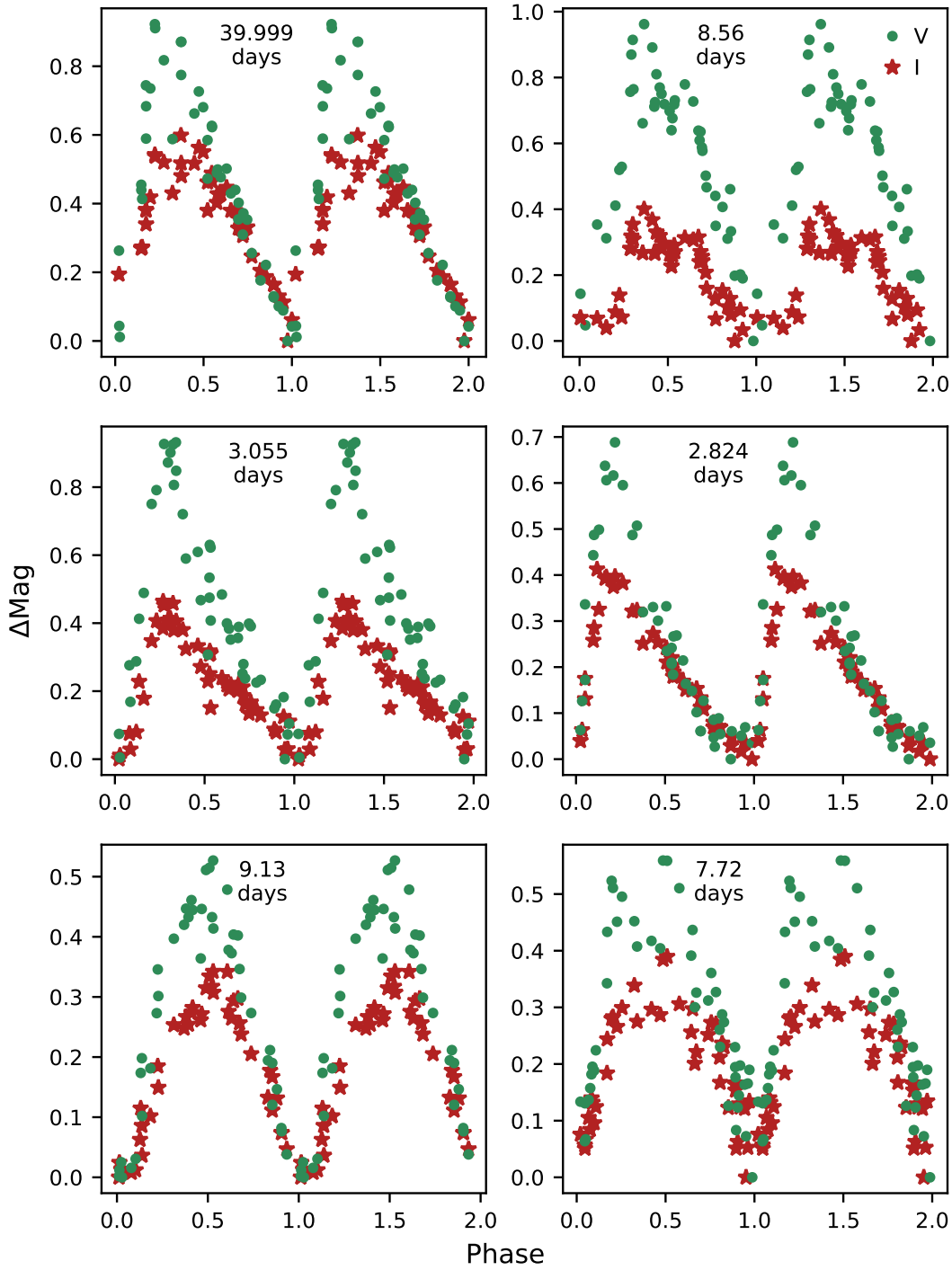

Figure 4.7: Magnitude difference light curves for a sample of 6 LMC Cepheids. The green circles represent the V-band and the red stars are in the I-band.

Table 4.5: The number of sources detected in the co-added absolute values of the subtracted frames for each cluster.

Cluster	No. of detections
NGC 1818	218
NGC 1850	154
NGC 1866	119
NGC 2031	188
NGC 2136	314
NGC 2157	348

each cluster is given in Table 4.1. Figure 4.8 shows the positions of the Cepheids in each cluster as well as the boundary of the cluster's half-light radius.

The second rejection was done by using the proper motions of the stars in each cluster determined by the $Gaia$ mission ($Gaia$ Collaboration et al., 2016, 2018; Lindegren et al., 2018). We took into account the proper motions of all of the stars within the half-light radius for each of the clusters. We then rejected any Cepheids whose proper motion was more the one sigma from the mean of the stars in each cluster. Figures 4.9 to 4.14 show this for each cluster. The resultant list of Cepheids used for my Period-Age relation is presented in Table 4.6 along with each star's coordinates and their designation in previous publications. The periods of any overtone pulsators have been fundamentalised using Equation 4.3 from Alcock et al. (1995), where P_1 is the period of the first overtone Cepheid and P_0 is the corresponding fundamental period.

$$\frac{P_1}{P_0} = 0.733 - 0.034 \log P_1, \; 0.1 < \log P_1 < 0.7 \tag{4.3}$$

4.5 Period-Age Relation

For each of the clusters we calculated the mean period for all of the fundamental mode Cepheids and the fundamentalised periods of the first overtone Cepheids. We used

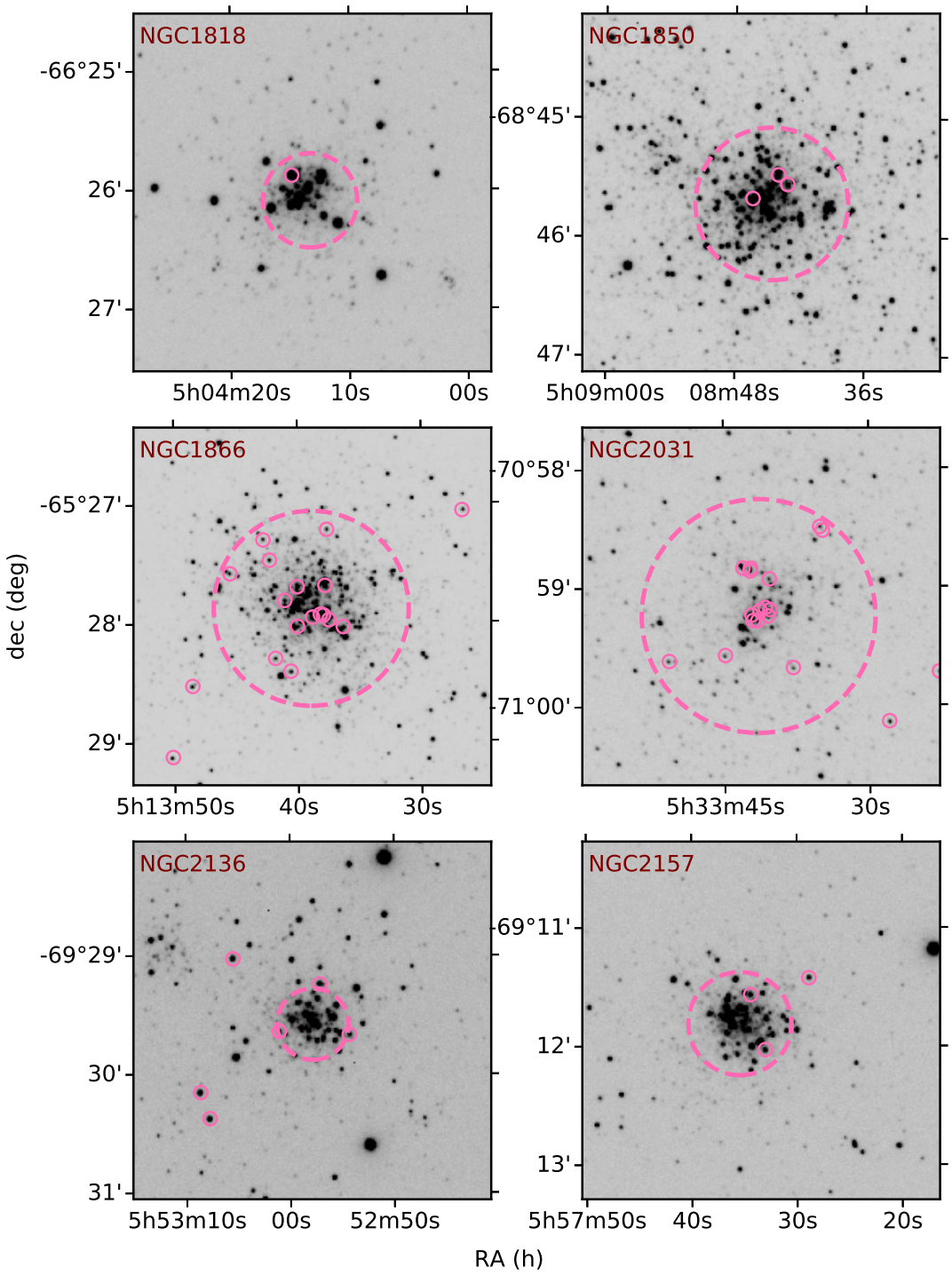

Figure 4.8: Position of Cepheids (highlighted by pink circles) in LMC Clusters with pink dashed rings highlighting the half-light radius of each cluster. The Cepheids lying outside of the half-light radii have been discounted.

Table 4.6: LMC Cepheid coordinates

Cluster	RA (J2000.0) (hms)	Dec (J2000.0) (dms)	P (days)	Cepheid
NGC 1818	05 04 14.92	-66 25 52.8	39.999	New
NGC 1850	05 08 43.97	-68 45 27.9	18.6639	OGLE
-	05 08 43.11	-68 45 33.0	8.55965	OGLE
-	05 08 46.25	-68 45 39.6	5.56533, 7.92288*	OGLE
NGC 1866	05 13 42.31	-65 27 30.0	3.45234	V7[a]
-	05 13 41.10	-65 27 50.3	3.05501	We 2[b]
-	05 13 40.58	-65 28 26.1	3.04019	We 8[b]
-	05 13 40.02	-65 27 43.4	2.85999	We 4[b]
-	05 13 40.05	-65 28 03.4	3.04855	We 3[b]
-	05 13 38.83	-65 27 59.2	3.05388	We 11[b]
-	05 13 38.20	-65 27 56.9	3.17515	We 5[b]
-	05 13 37.94	-65 27 57.8	2.898	WS 5[c]
-	05 13 37.66	-65 27 14.5	3.3183	V4[a]
-	05 13 37.52	-65 28 00.2	3.28999	We 6[b]
-	05 13 36.33	-65 28 03.7	3.06979	WS 9[c]
-	05 13 42.81	-65 27 19.6	2.00715, 2.79619*	V8[b]
-	05 13 41.84	-65 28 19.5	1.9448, 2.7075*	V6[b]
NGC 2031	05 33 42.43	-70 58 52.8	2.97151	V14[a]
-	05 33 42.41	-70 58 51.3	3.19436	OGLE
-	05 33 42.18	-70 59 18.1	3.04226	OGLE
-	05 33 41.68	-70 59 17.9	3.27879	V8[a]
-	05 33 40.58	-70 59 15.7	3.03111	V6[a]
-	05 33 40.48	-70 58 56.7	2.96081	V9[a]
-	05 33 38.03	-70 59 41.7	2.82426	V11[a]
-	05 33 42.29	-70 59 15.0	2.05851, 2.86926*	OGLE
-	05 33 41.45	-70 59 12.5	2.00784, 2.79717*	OGLE
NGC 2136	05 53 01.21	-69 29 38.0	4.41422	OGLE
-	05 53 57.28	-69 29 14.3	9.1301	OGLE
-	05 52 54.42	-69 29 39.7	3.17456, 4.46552*	OGLE
NGC 2157	05 57 33.13	-69 12 01.7	7.71987	V2[a]
-	05 57 34.49	-69 11 33.7	3.64837, 5.1472*	V3[a]

* Fundamentalised period of overtone pulsation using 4.3

[a] As designated in Mateo (1992)

[b] As designated in Welch et al. (1991)

[c] As designated in Welch and Stetson (1993)

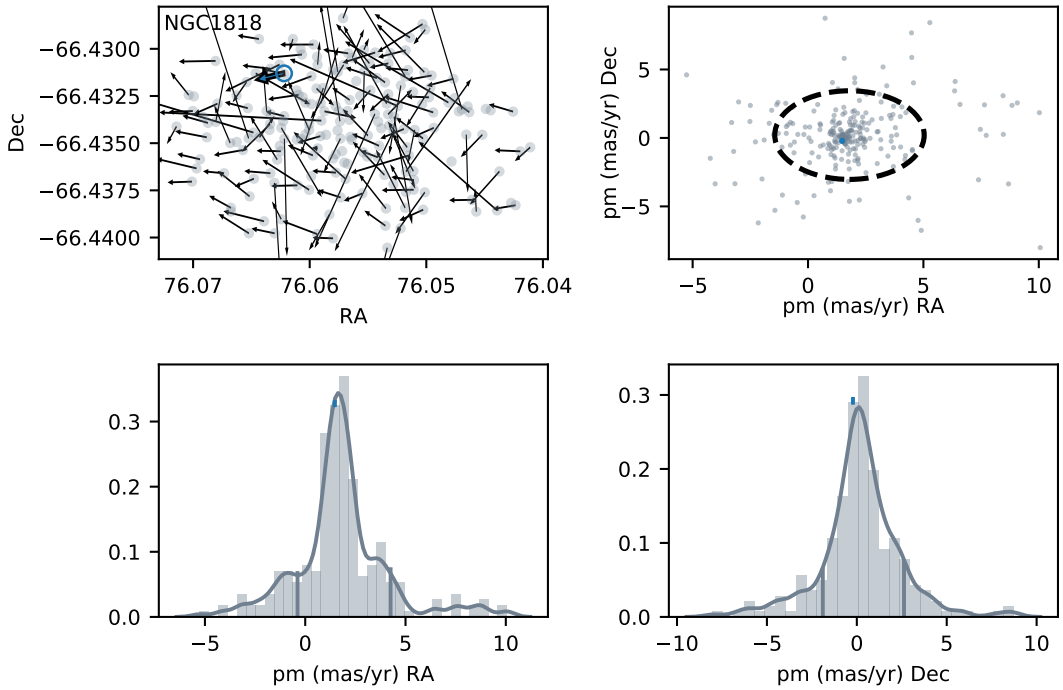

Figure 4.9: *Gaia* proper motions of stars inside the half-light radius of NGC 1818. The dashed black ring in the top right panel indicates 1 sigma from the mean proper motion. The vertical grey lines in the in the bottom two panels also show one sigma from the mean for the proper motions in both RA and Dec. Cepheids lying outside these limits have been discounted.

the mean periods to apply a least squares fit in order to derive the PA relation which is weighted by the errors on the cluster ages. We derived one equation using the six clusters in my dataset that host Cepheids. However, two of the clusters only include a single fundamental mode Cepheid each and so we derived a second PA relation using the four clusters that are home to multiple fundamental mode Cepheids.

The four clusters that have multiple fundamental mode Cepheids show a range of the periods that increases with the age of the host cluster as can be seen in Table 4.1 and Figure 4.3. A possible cause for this is discussed in the next section. Therefore, we have also included two further PA relations, one using just the higher period Cepheids and another only using the lower period Cepheids. The PA relations that we have derived are presented in Table 4.7 along with the recent modeled PA relation at LMC metallicity and average progenitor rotation rate of ω=0.5 by Anderson et al. (2016), and

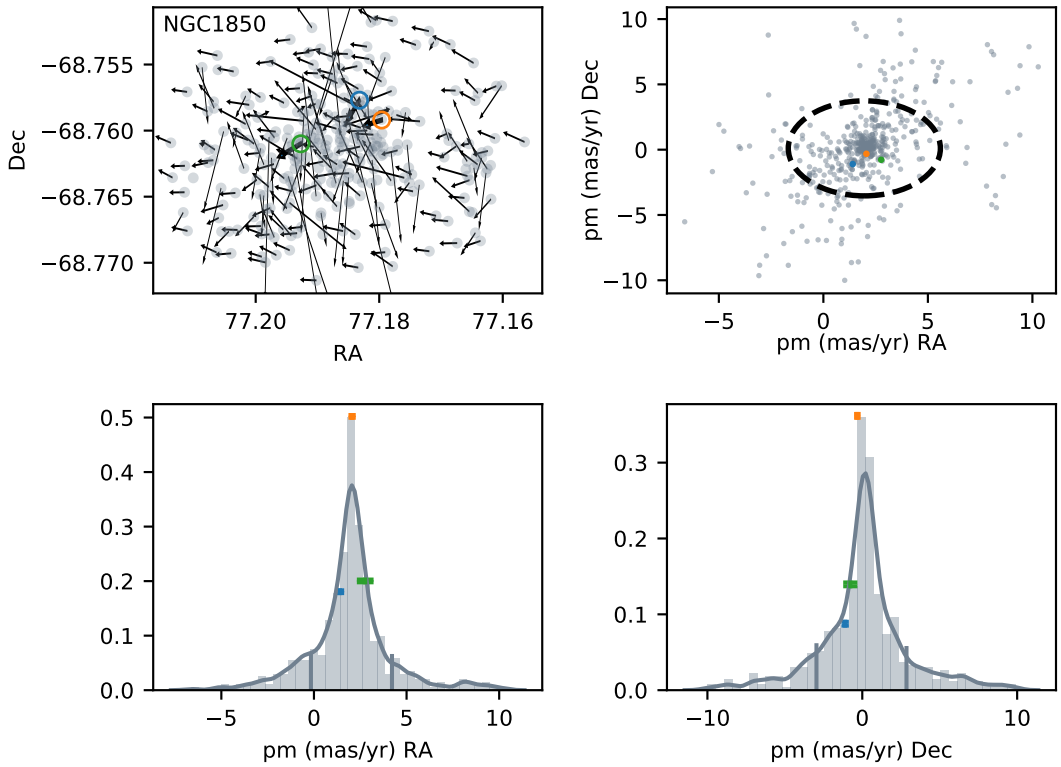

Figure 4.10: *Gaia* proper motions of stars in and around NGC 1850. See Figure 4.9 for details.

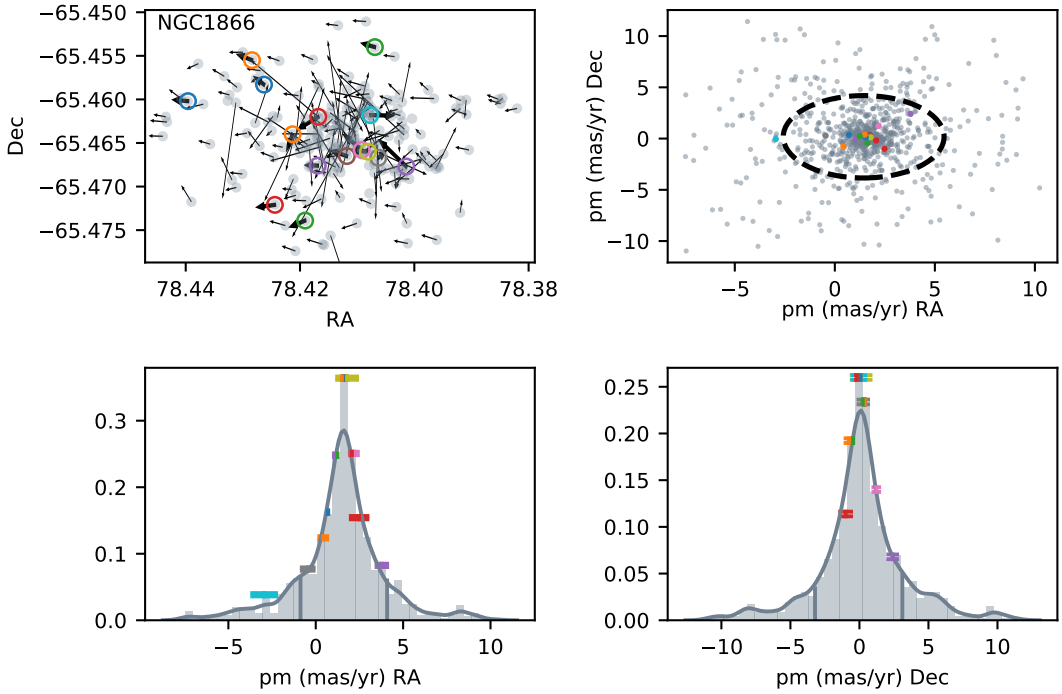

Figure 4.11: *Gaia* proper motions of stars in and around NGC 1866. See Figure 4.9 for details.

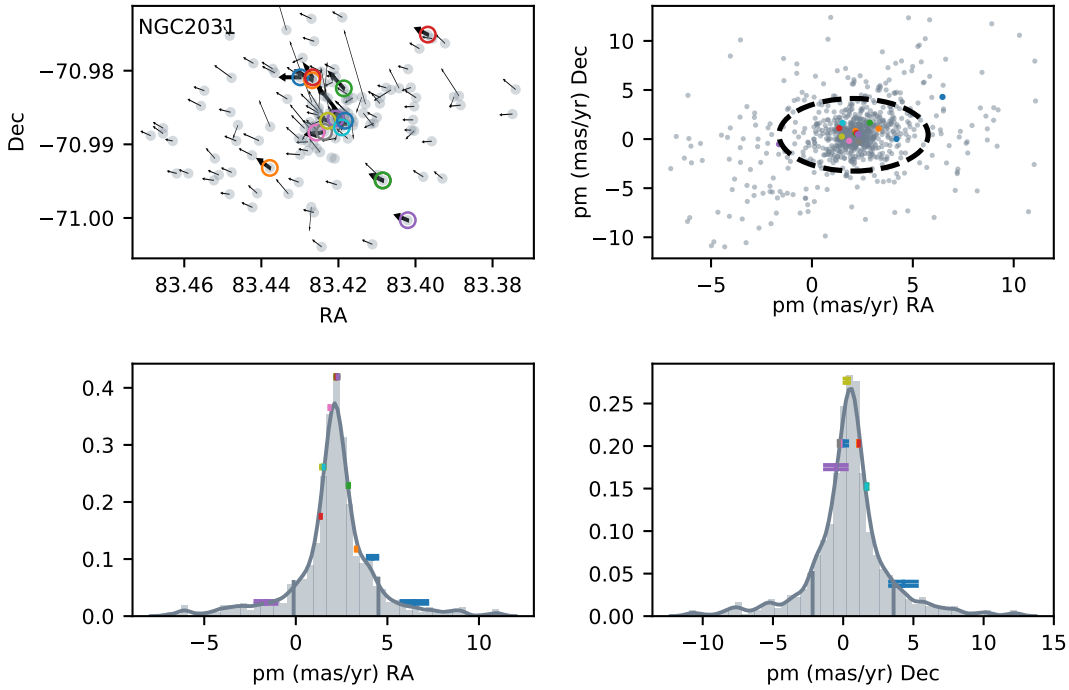

Figure 4.12: *Gaia* proper motions of stars in and around NGC 2031. See Figure 4.9 for details.

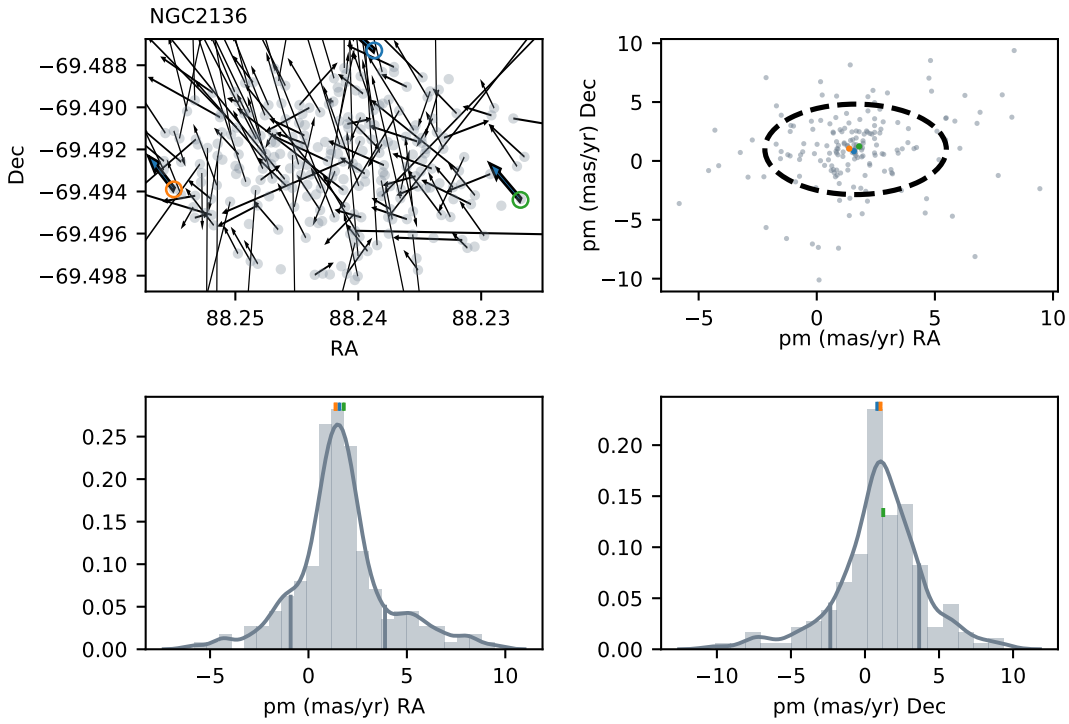

Figure 4.13: *Gaia* proper motions of stars in and around NGC 2136. See Figure 4.9 for details.

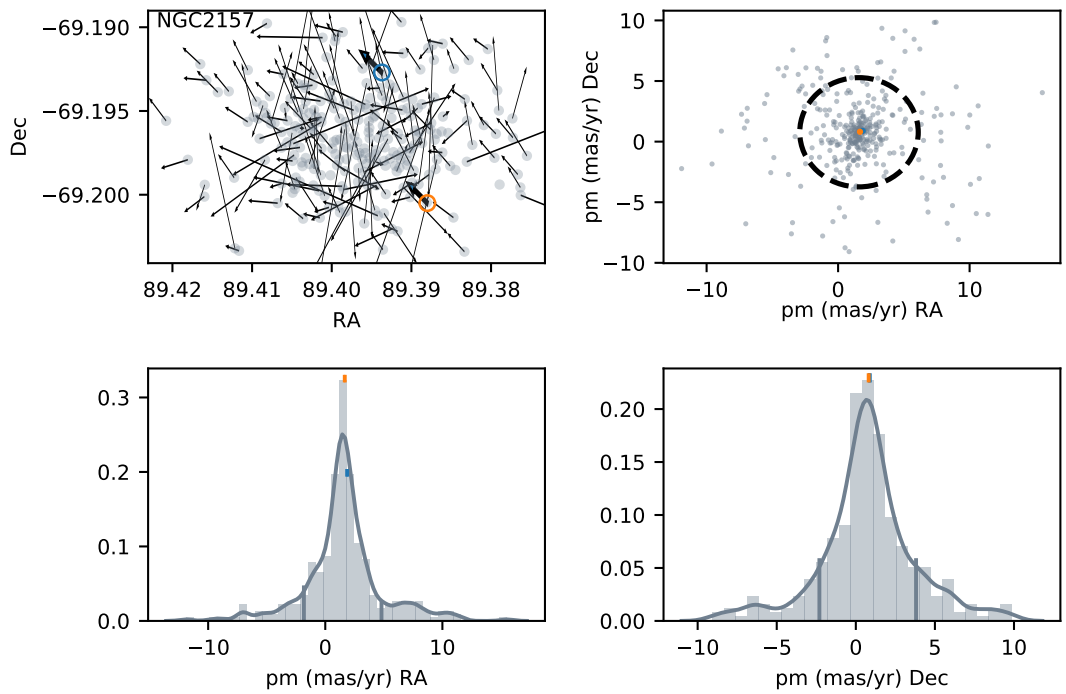

Figure 4.14: *Gaia* proper motions of stars in and around NGC 2157. See Figure 4.9 for details.

the previous empirical Cepheid PA relation derived from LMC clusters by Efremov (2003).

The error on cluster isochrones affects the zero-point of the Cepheid PA relation, whereas, uncertainty on the slope is affected by the period range of cluster Cepheids. As we can see in Table 4.7, the gradient of the PA relation can be significantly altered by using either the low or high period Cepheid population as the observed period range is larger for the younger clusters. Cepheid lifetimes are much longer for lower mass stars which explains why there are many more Cepheids in the older clusters NGC 1866 and NGC 2031 compared to the other clusters in our sample. Therefore, the mean periods for these two older clusters is more trustworthy the the mean periods of Cepheids in the younger clusters. Stellar models have shown that for lower mass, older, Cepheids the third crossing of the instability strip is the longest. For higher mass Cepheids, the second and third crossing timescales are very similar and the proportion of time spent on the first crossing compared to the second and third is increased (An-

Table 4.7: Period-Age relations $\log t = \alpha \log P + \beta$. Also included are the degrees of freedom, F-statistic and the probability that the fit happened by chance.

	α	β	df	F-stat	P-value
Mean from 6 clusters	-0.772±0.055	8.703±0.046	4	197.5	<0.001
Mean from 4 clusters	-0.758±0.054	8.707±0.040	2	193.6	0.005
Higher Periods	-0.577±0.036	8.640±0.031	2	253.7	0.004
Lower Periods	-0.994±0.110	8.801±0.071	2	81.3	0.012
Anderson et al. (2016)	-0.665	8.628			
Efremov (2003)	-0.683	8.531			

derson et al., 2014). Therefore, it is more likely that Cepheids in younger clusters will be found at different instability strip crossings, leading to an increased range of periods. The increased period range will affect the mean period and therefore the slope of the PA relation.

Figure 4.15 shows our PA relation compared with those of Efremov (2003) and the modeled relation of Anderson et al. (2016). Efremov's relation shows a shallower gradient than ours with a difference of 0.2 dex in age at the shorter period end but a similar age prediction at the longer period end of the relation. We think there are two main reasons for this, the first being that the age estimates of the clusters are not as accurate as they are today. For example, earlier in this Chapter, we discussed how from literature the most recent age estimation for NGC 2031 came from Mould et al. (1993) at ∼140 Myr whereas Silvia Martocchia found the age to be ∼230 Myr. Another factor could be that the youngest cluster that Efremov used was ∼50 Myr containing a single Cepheid with a period of ∼20 days whereas we have discovered a ∼40 day period Cepheid in the younger cluster NGC 1818. These two factors, that of increasing the ages of the clusters at the short period end and find a long period Cepheid at a much younger age than Efremov (2003), have caused the larger gradient of our PA relation derived from LMC clusters.

Using models Anderson et al. (2016) found a gradient for the PA relation for Cepheids

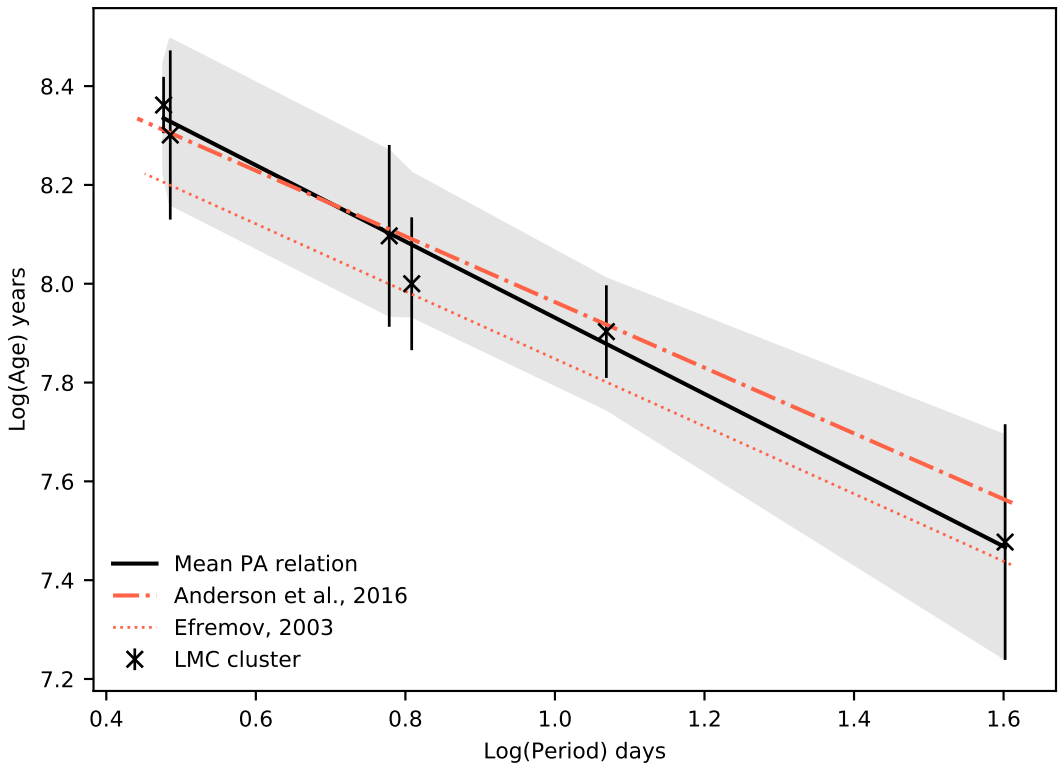

Figure 4.15: Mean empirical period-age relation derived from Cepheids LMC clusters from this work compared with the one of Efremov (2003) and recent modelled relations by Anderson et al. (2016).

at LMC metallicity similar to that of Efremov (2003) but with a higher zero point. The possible period ranges for $9M_{\odot}$ stars entering the IS in the models used by Anderson et al. (2016) at LMC metallicity are $\sim$10-20 days for a progenitor rotation rate of zero, $\sim$15-55 days for ω=0.5 and $\sim$30-80 days for ω=0.9. With such a large range of potential periods for the highest mass (youngest) Cepheids it is possible that the when deriving the PA relation Anderson et al. (2016) underestimated the period values at the young end leading to the disparity with our empirical relation.

4.5.1 Rotation effects on PA relation

The large discrepancy between the shortest and longest periods in some of the clusters, especially NGC 1850, poses an interesting conundrum. If these Cepheids are all cluster

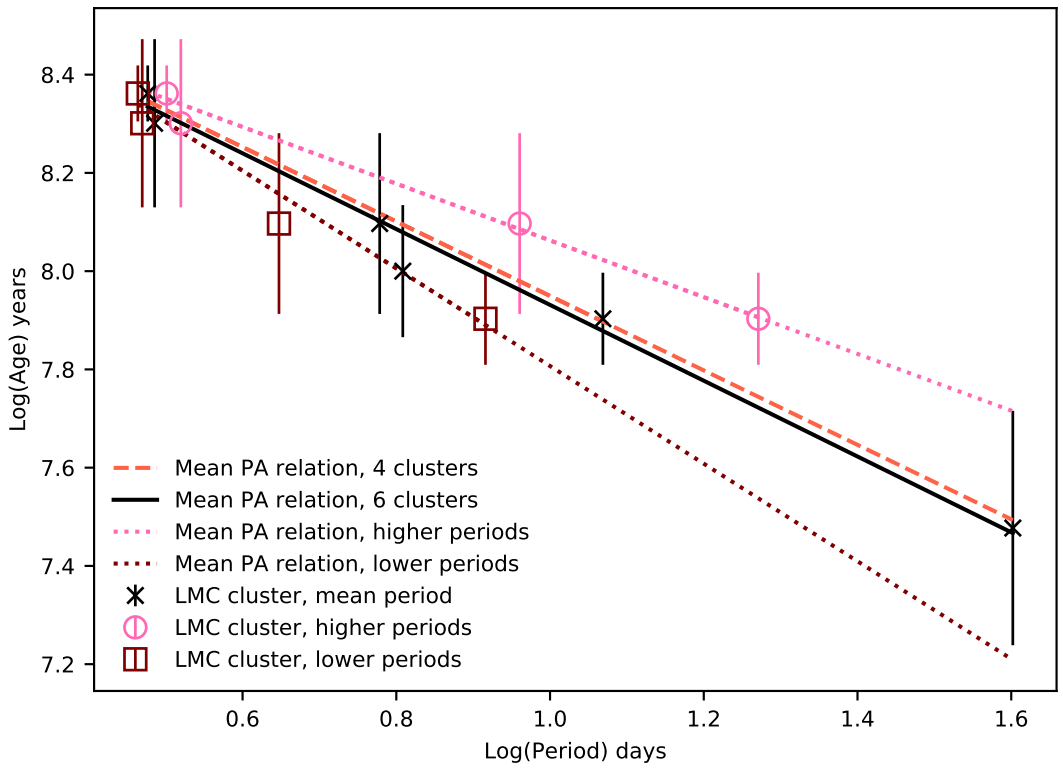

Figure 4.16: Mean empirical period-age relations derived from Cepheids LMC clusters for four different scenarios. Mean relation from all Cepheids in all clusters, mean relation from all Cepheids minus two of the clusters, mean relation from only higher period Cepheids and mean relation from lower period Cepheids.

members then what could cause such a large range of periods. As clusters NGC 1818 and NGC 2157 only each include a single Cepheid pulsating in the fundamental mode we have discounted those two clusters in the this part of the analysis.

We split the Cepheid populations in the four clusters with multiple fundamental mode Cepheids into higher and lower periods and produced PA relations for each case. The PA relations for the highest periods and lowest periods are shown in Figure 4.16 along with the mean PA relation for the four clusters in this case compared with the PA relation derived from all six clusters. When removing the two clusters which only contain a single fundamental mode Cepheid each the mean PA relation is almost identical to the PA relation derived from all of the clusters. The PA relations derived from just taking into account the longest period Cepheids in each cluster or the shortest period

Cepheids exhibit a strong relation as shown in Table 4.7 and Figure 4.16. Therefore, whatever is causing the large spread of Cepheid periods in a single cluster affects the clusters consistently with the increasing ages of the clusters in this sample.

One potential avenue to explore this phenomenon is by looking at the progenitor rotation rates of the Cepheids. Rotation causes a star's MS lifetime to increase. At a given mass the faster the rotation the longer a star spends on the MS. This means that in a simple stellar population if there exists a range of rotation rates then the faster rotating stars will take longer to evolve to the IS than low or non-rotating stars of the same mass. The increased MS lifetime is caused by the mixing process supplying the core with fresh Hydrogen during the core Hydrogen burning phase. Therefore, at a given age there will exist larger range of different mass stars across the IS due to the star's different progenitor rotation rates than if all of the stars had the same rotation rate on the MS. This leads to there being a larger range of periods for the Cepheid population than would be expected if all of the stars had the same initial rotation rates.

The question then becomes whether the observed range of periods in the clusters can be explained by stellar rotation. Figures 4.17 and 4.18 show how different rotation rates applied to the Geneva `SYCLIST` stellar isochrones (Georgy et al., 2013b) affect the stars' later evolution through the IS. The dashed grey lines traveling diagonally across the figures show lines of constant period which are akin to the lines of constant radius across the HR diagram and have been calculated from period-radius relations derived by Anderson et al. (2016). Models of a single rotation rate do not cover the observed periods ranges in these cases instead models from at least two different stellar rotation rates are needed to recreate the Cepheid period spread for these clusters.

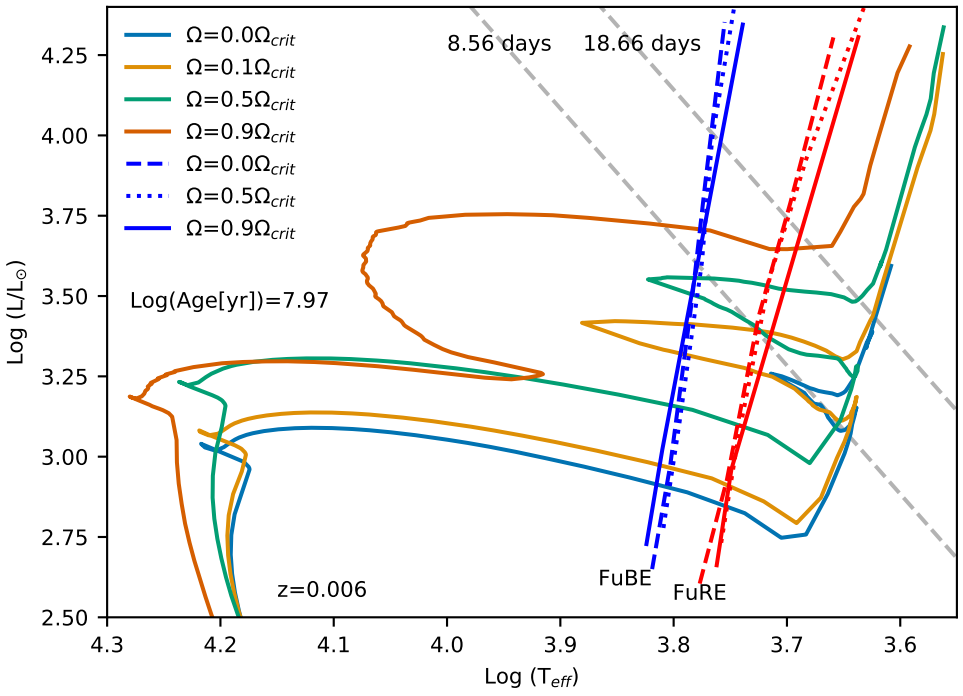

Figure 4.17: NGC 1850 age Geneva Isochrones of different rotation rates showing how progenitor rotation rates affect Cepheid periods potentially causing the spread of observed periods in stellar Clusters. Instability strip limits from Anderson et al. (2016).

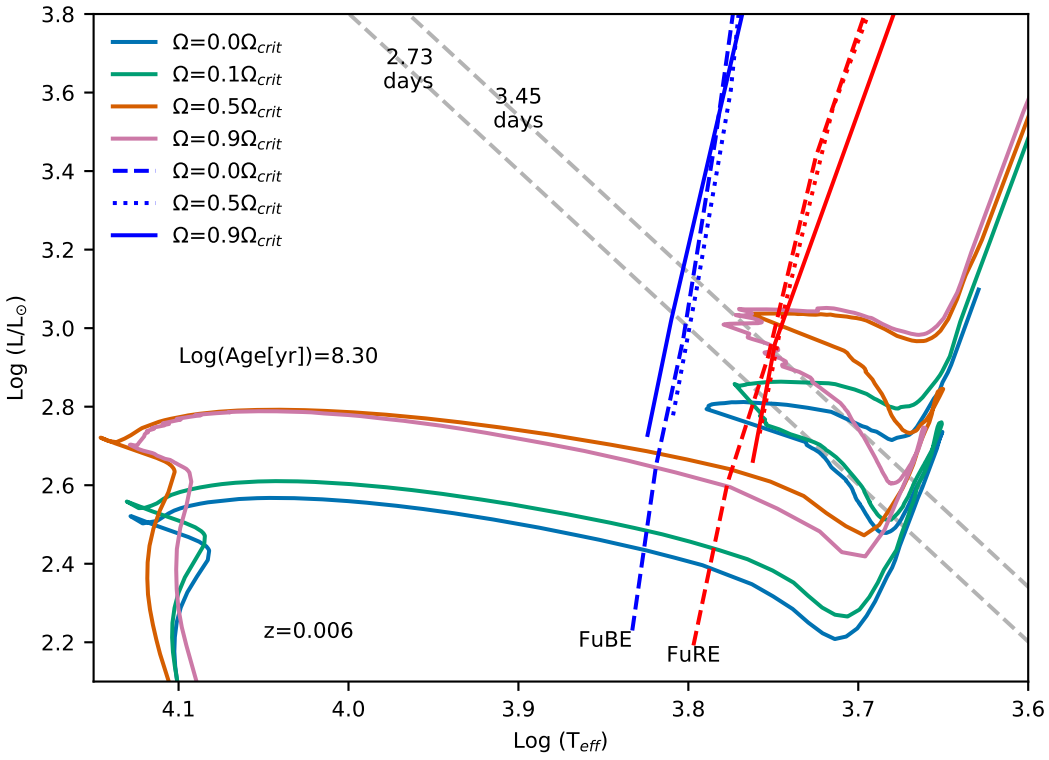

Figure 4.18: NGC 1866 age Isochrones of different rotation rates showing how progenitor rotation rates affect Cepheid periods potentially causing the spread of observed periods in stellar Clusters. Instability strip limits from Anderson et al. (2016).

Chapter 5

Discussion & Future Work

5.1 M33 Data

5.1.1 Summary of Data Calibration

Hartman et al. (2006) conducted a variability survey on the Triangulum galaxy, also known as M33, using the CFHT on 27 nights over 17 months beginning August 2003 in which they identified over 36000 variable objects producing a catalogue of variable point sources. Further data was taken using the INT covering 13 nights spread between 3 observing runs over 19 months beginning February 2008 producing $\sim$45 epochs in total. To cover the entire galaxy four pointings of the wide field camera were used. To calculate response of the CCDs at the INT, images taken of the SDSS field Stripe 82 which were calibrated using dr12 standard star catalogues. PSF fitting photometry was performed by Kevin Tsang to produce transformation Equation 2.2. The fit was inverted to produce a calibrated catalogue of stars from the INT images.

Template images were built from the INT data to be used as the reference frames

for image subtraction as well as for photometric calibration. The images in each set that had the best seeing as well as the least elongated or skewed stars were identified and then averaged together to produce the templates. Image subtraction methods were used to locate variable sources which involves the pixels of one image being subtracted from another leaving behind any objects that have changed in brightness. The images taken on different nights were then individually subtracted from the template using `HOTPANTS` (Becker, 2015) which is based on `ISIS` (Alard and Lupton, 1998; Alard, 2000).

Variable sources were identified by using `SExtractor` (Bertin and Arnouts, 1996) on the absolute versions of the subtracted images. Aperture photometry was performed on each of the subtracted images in `IRAF` to obtain the flux difference from the template for each and every epoch. The flux light curves were converted to magnitude light curves using the transformation equations produced by Kevin Tsang. The now magnitude calibrated light curves were merged with the CFHT light curves and matched by the WCS information. The mean magnitudes of the light curves are taken and used to work out the magnitude offset for each object between the two datasets. However, a substantial proportion of the cross-calibrated light curves show a discrepancy in their amplitudes.

5.1.2 Conclusions

To test possible causes of the amplitude discrepancy, any mismatching of the stars between the CFHT and INT data was checked. However, the WCS transformations between the two templates match well as shown with no obvious indication that there is any discrepancy in the coordinates. There also does not seem to be any correlation of amplitude difference with position in M33 or with the pixels coordinates on the CCD

chips.

A workaround was devised to get past this amplitude discrepancy. The ratio of the amplitude differences were calculated for each light curve and used to scale the amplitudes of the INT light curves so that they matched the CFHT light curves.

5.1.3 Further Research

Investigations into how much flux needs to be removed or added to the data for each of the Cepheid variable stars to account for amplitude differences between the light curves of the INT and CFHT data needs to be done. The photometry and image subtraction could then be done on smaller regions around where large amplitude differences are found to see if it related crowding or companion stars.

The INT data is not of the highest quality with many of the nights suffering from poor seeing. This manifested itself as large amounts of scatter in many of the lights curves. It is possible that all that is required is higher quality data and that it was not possible to get a high enough signal-to-noise ratio at the magnitude level of beat Cepheids at the INT. Some preliminary work was done to compare light curves from the CFHT data with data taken by the WIYN 3.5m telescope atop the Kitt Peak National Observatory for the work of Scowcroft et al. (2009). The WIYN data is of similar quality to that of the CFHT data and the light curves matched well not showing the same amplitude problem. However, the WIYN data covers just two relatively small regions of M33 meaning it was only possible to compare a limited sample of Cepheids.

5.2 Beat Cepheids in M33

5.2.1 Summary

An AoV routine was used on all of the merged INT and CFHT light curves for the stars that are present in the candidate Cepheid list using VARTOOLS (Hartman and Bakos, 2016). The period value represented by the top peak from the pre-whitened periodogram was taken to be the strongest period. The top 3 periods were extracted from the whitened periodogram of the second pass and those that gave a period ratio of between 0.66 and 0.78 were kept. Of the 3019 candidate Cepheids 3 Cepheids, other than the 5 found by Beaulieu et al. (2006), showed promise to be beat Cepheids.

By plotting beat Cepheids found in M33 with beat Cepheids of known metallicity in the Milky Way (Z=0.020), LMC (Z=0.008) and SMC (Z=0.004) on a Petersen diagram comparisons can be made to determine their metallicity. The equivalent metallicities of the beat Cepheid period ratios were determined using equations from Sziládi et al. (2007) and Kovtyukh et al. (2016) who used high resolution spectroscopy to determine the metallicities of Galactic beat Cepheids. The galactocentric distances of the beat Cepheids are derived by deprojecting their celestial coordinates with an inclination angle of 53° and a position angle of 22° at a distance of 840 kpc.

5.2.2 Conclusions

The metallicity gradient determined in this work, $\frac{d[O/H]}{d\rho} = -0.124$ dex kpc^{-1} or $\frac{d[O/H]}{d\rho} = -0.067$ dex kpc^{-1} are steeper than most of the gradients found by recent studies of HII regions $\frac{d[O/H]}{d\rho} = -0.034 - -0.012$ dex kpc^{-1}. However, it is more in line with the older work of Garnett et al. (1997) at $\frac{d[O/H]}{d\rho} = -0.11$ dex kpc^{-1}.

Tsang et al. (submitted) found that using the shallower HII region derived metallicity gradients lead to excessively large metallicity corrections implying that a steeper metallicity gradient exists in M33 such as the one found by Urbaneja et al. (2005) from blue supergiants, $\frac{d[O/H]}{d\rho} = -0.06$ dex kpc^{-1}, or from this work.

A possible reason for the discrepancy in metallicity measures between methods could be that the metallicity gradient derived here is obtained from a small sample of beat Cepheids. However, the relation between period ratios and metallicity is well described by pulsation theory and not subject to the same potential systematic errors that can plague spectroscopic methods. The robustness of the method of using beat Cepheids to measure metallicity is shown by the fact that the location of beat Cepheids in different galaxies, i.e. the Milky Way, SMC and LMC, on the Petersen diagram is dependant on the metallicity of their host galaxy.

5.2.3 Further Research

With the new generation of telescopes such as the LSST, the E-ELT or the JWST, we are entering a new era of high-precision astronomy. As shown in Chapter 2, the accuracy of the calibration significantly decreases at magnitudes fainter $\sim$20.5 in the r'-band. LSST will be able observe to r'-band magnitudes down to $\sim$24.7 (Ivezić et al., 2019) meaning the brightest Cepheids could be observed out to 8Mpc and $\sim$3Mpc for beat Cepheids of typical magnitude. As M33 is well within this distance, $<$1Mpc, we will get much more accurate observations of M33 Cepheids and therefore find numbers of beat Cepheids closer to what we expect to see. This will lead to an M33 metallicity gradient of much greater accuracy. We will also be able to do the same for other galaxies within 3Mpc in which we are not currently able to observe the fainter beat Cepheids.

The metallicity of the Cepheids in M33 could be checked using high resolution spectroscopy to measure the metallicity gradient and compared with that found by beat Cepheids and other methods. However, this is not currently possible as we cannot currently achieve the required signal-to-noise ratio but maybe it will be possible in the future.

5.3 Cepheid Period-Age Relation

5.3.1 Summary

There exists a period-age relation for Cepheid variable stars. Observations were taken of 8 LMC stellar cluster using the 2 m Faulkes Telescope South at the Siding Spring node of the Las Cumbres Observatory. The data covers 2 observing runs, the first taking place from October 2013 until February 2014 supplying $\sim$15 observations with an exposure time of 15 s and used the Merope Camera. The second ran from October 2015 until February 2016 supplying $\sim$30 observations with an exposure time of 30 seconds and used the Spectral Camera. Of the 8 clusters 6 were suitable to be used for this work.

The Ages for each of the clusters were taken from literature with the exception of NGC 2031 where the age was determined from Isochrone fitting and comparison with other clusters by Silvia Martocchia using HST photometry.

In order to find the variable stars and produce light curves image subtraction was implemented using the software `HOTPANTS` (Becker, 2015) which is based on the `ISIS` image subtraction package (Alard and Lupton, 1998; Alard, 2000). The templates for subtraction were produced by selecting images from nights with the best seeing and

averaging them together. The images from each epoch are then subtracted in turn from its corresponding template producing a series of subtracted frames. To find Cepheids `SExtractor` was run on images of co-added absolute values of all of the subtracted frames for each field.

Many Cepheids in the field of each cluster were found but they were not necessarily all cluster members. The first rejection of stars was done by determining which Cepheids lie within the half light radius for each cluster. The second rejection was done by using the proper motions of the stars in each cluster determined by the $Gaia$ mission ($Gaia$ Collaboration et al., 2016, 2018; Lindegren et al., 2018). Any Cepheids whose proper motion was more the one sigma from the mean of the stars in each cluster were rejected.

5.3.2 Conclusions

The mean periods of the Cepheids in each cluster were used to apply a least squares fit in order to derive the PA relation. One equation was derived using the 6 suitable clusters in the dataset. However, two of the clusters only include a single fundamental mode Cepheid each and so a second PA relation was derived using the four clusters that are home to multiple fundamental mode Cepheids.

The four clusters that have multiple fundamental mode Cepheids show a range of the periods that increases with the age of the host cluster. Therefore, two further PA relations were derived, one using just the higher period Cepheids and another only using the lower period Cepheids. The PA relations as derived in Chapter 4 are presented here again in Table 5.1 along with the recent modeled PA relation at LMC metallicity and average progenitor rotation rate of ω=0.5 by Anderson et al. (2016), and the previous empirical Cepheid PA relation derived from LMC clusters by Efremov (2003).

Table 5.1: Period-Age relations $\log t = \alpha \log P + \beta$. Same as Table 4.7 in Chapter 4

	α	β
Mean from 6 clusters	-0.772±0.055	8.703±0.046
Mean from 4 clusters	-0.758±0.054	8.707±0.040
Higher Periods	-0.577±0.036	8.640±0.031
Lower Periods	-0.994±0.110	8.801±0.071
Anderson et al. (2016)	-0.665	8.628
Efremov (2003)	-0.683	8.531

Efremov's relation shows a shallower gradient than ours with a difference of 0.2 dex in age at the shorter period end but a similar age prediction at the longer period end of the relation. This is caused by the increase of the ages of the clusters at the short period end and finding a long period Cepheid at a much younger age than Efremov (2003), have caused the larger gradient of my PA relation derived from LMC clusters.

The large discrepancy between the shortest and longest periods in some of the clusters poses an interesting conundrum. Rotation causes a star's MS lifetime to increase. At a given mass the faster the rotation the longer a star spends on the MS. This means that in a simple stellar population if there exists a range of rotation rates then the faster rotating stars will take longer to evolve to the IS than low or non-rotating stars of the same mass. Models of a single rotation rate do not cover the observed periods ranges in these cases instead models from at least two different stellar rotation rates are needed to recreate the Cepheid period spread for these clusters.

5.3.3 Further Research

Using the PA relations derived here one could produce an age map of the LMC known Cepheids available in the OGLE collection of variable stars. Therefore, it is possible to trace the recent star formation history of the LMC from the period distribution of its Cepheids (Alcock et al., 1999). This would be possible for the age range in which

Cepheids can exist, $\lesssim$40 Myr for the longest period Cepheids up $\sim$250 Myr for the shortest period Cepheids and everything in between. The methods applied here could also be reproduced to determine Cepheid PA relations from clusters in the Milky Way and SMC. Anderson et al. (2016) predicts different Cepheid PA relations at different metallicities. Therefore, one could expect that PA relations derived from stellar clusters of galaxies with various metallicities would not be the same.

Appendix A

LMC Data

Table A.1: Number of images per cluster for each observing night

	NGC1818		NGC1831		NGC1850		NGC1856		NGC1866		NGC2031		NGC2136		NGC2157	
Date	I	V	I	V	I	V	I	V	I	V	I	V	I	V	I	V
2013-10-01	0	0	0	0	0	0	0	0	1	1	0	0	0	0	0	0
2013-10-19	0	0	0	0	0	0	1	1	0	0	0	0	0	0	0	0
2013-11-01	1	1	1	1	1	1	1	1	1	1	1	1	1	1	1	1
2013-11-09	0	0	0	0	0	0	0	0	1	1	0	0	0	0	0	0
2013-11-15	1	1	1	1	1	1	1	1	1	1	1	1	1	1	0	0
2013-11-16	0	0	0	0	0	0	0	0	0	0	0	0	0	0	1	1
2013-11-23	1	1	1	1	1	1	1	1	1	1	1	1	1	1	1	1
2013-11-30	1	1	1	1	1	1	1	1	1	1	1	1	1	1	1	1
2013-12-06	1	1	1	1	1	1	1	1	1	1	1	1	1	1	1	1

2013-12-13	1	1	1	1	1	1	1	1	1	1	1	1	1	1	1
2013-12-21	1	1	1	1	1	1	1	1	1	1	1	1	1	1	1
2013-12-27	1	1	1	1	1	1	1	1	1	1	1	1	1	1	1
2014-01-05	1	1	1	1	1	1	1	0	0	0	0	0	0	0	0
2014-01-06	0	0	0	0	0	0	0	1	1	1	1	1	1	1	1
2014-01-10	1	1	1	1	1	1	1	1	1	1	1	1	1	1	1
2014-01-12	1	1	0	0	1	1	1	1	1	0	0	0	0	0	0
2014-01-14	1	1	0	0	1	1	1	1	1	1	1	1	1	1	1
2014-01-21	0	0	0	0	0	0	0	0	0	0	0	0	0	1	1
2014-01-23	0	0	0	0	1	1	1	1	0	0	1	1	1	1	1
2014-01-27	1	1	1	1	1	1	1	1	1	1	1	1	1	1	1
2014-01-28	1	1	1	1	1	1	1	1	1	1	1	1	1	1	1
2014-02-01	1	1	1	1	1	1	1	1	1	1	1	1	1	1	1
2014-02-08	1	1	1	1	1	1	1	1	1	1	1	1	1	1	1
2014-02-23	0	0	0	0	0	0	1	1	0	0	0	0	0	0	0
2015-10-06	0	0	0	0	1	1	1	1	1	1	1	1	1	0	0
2015-10-07	1	1	1	1	0	0	0	0	0	1	1	1	1	0	0
2015-10-08	0	0	0	0	1	1	1	1	0	0	1	1	1	0	0
2015-10-09	1	1	1	1	0	0	1	1	1	1	0	0	0	1	1
2015-10-10	1	1	1	1	0	0	0	0	0	0	0	1	1	1	1
2015-10-11	1	1	0	0	0	0	1	1	1	1	1	0	0	1	1
2015-10-24	1	1	2	1	1	1	1	1	1	1	1	1	1	1	1
2015-10-27	0	0	0	0	1	1	1	1	0	0	0	0	0	0	0
2015-10-29	0	0	0	0	0	0	0	0	1	1	0	0	1	1	0	0
2015-10-30	1	1	1	1	0	0	0	0	0	0	1	1	0	0	1	1
2015-11-01	0	0	0	0	0	0	1	1	0	0	0	0	0	0	0	0
2015-11-03	0	0	1	1	1	1	0	0	1	1	0	0	0	0	0	0
2015-11-07	0	0	0	0	1	1	0	0	0	0	0	0	0	0	0	0

2015-12-01	0	0	0	0	0	0	0	0	0	0	0	0	0	1	0
2015-12-02	0	0	0	0	0	0	0	0	0	0	0	0	0	0	1
2015-12-04	1	1	1	1	1	1	1	1	1	1	1	1	1	0	0
2015-12-10	1	1	1	1	1	1	1	1	1	1	1	1	1	1	1
2015-12-15	0	0	0	0	1	1	0	0	0	0	0	0	0	0	0
2015-12-19	0	0	0	0	0	0	0	1	1	0	0	1	1	1	1
2015-12-20	1	1	0	0	0	0	1	1	1	1	1	1	2	1	1
2015-12-25	1	1	0	0	0	0	0	0	0	0	0	0	0	0	0
2015-12-26	1	1	0	0	0	0	0	0	0	1	1	1	1	1	1
2015-12-28	0	0	0	0	0	0	0	1	1	0	0	0	0	0	0
2015-12-30	0	0	0	0	0	0	0	1	1	1	1	1	1	1	1
2015-12-31	1	1	0	0	0	0	1	1	0	0	0	0	0	0	0
2016-01-01	1	1	0	0	0	0	1	1	1	1	1	1	1	1	1
2016-01-08	1	1	0	0	0	0	0	0	0	0	0	0	0	1	1
2016-01-09	1	1	1	1	1	1	1	1	1	1	1	1	1	1	1
2016-01-10	1	1	1	1	1	1	1	1	1	1	1	1	1	1	1
2016-01-11	0	0	0	0	1	1	1	1	1	1	1	1	1	1	1
2016-01-12	1	1	2	2	1	1	1	1	1	1	1	1	1	1	1
2016-01-14	1	1	1	1	1	1	1	0	0	1	1	1	1	1	1
2016-01-15	0	0	0	0	0	0	0	1	1	0	0	0	0	0	0
2016-01-18	1	1	1	1	1	1	0	2	2	2	1	1	1	1	1
2016-01-19	1	1	1	1	1	1	0	2	1	1	1	1	1	1	1
2016-01-20	1	1	1	1	1	1	0	2	1	1	1	1	1	1	1
2016-01-21	1	1	1	1	1	1	0	2	1	1	1	2	2	0	1
2016-01-22	0	0	0	0	0	0	0	0	0	0	1	1	0	0	1	0
2016-01-27	2	2	2	2	2	2	2	2	2	2	2	2	2	2	2
2016-01-29	0	0	0	0	1	1	0	0	0	0	0	0	1	1	0	0
2016-01-30	0	0	0	0	0	0	0	0	0	0	0	0	1	1	1	1

2016-01-31	1	1	1	1	1	1	1	1	1	1	1	1	1	1	1
2016-02-01	1	1	0	0	1	1	2	2	1	1	2	2	1	1	1	1
2016-02-02	2	2	1	1	0	0	0	0	1	1	1	1	1	1	1	1
2016-02-07	0	0	0	0	0	0	0	0	0	0	1	1	0	0	0	0
2016-02-10	0	0	1	2	0	0	1	1	1	1	1	1	1	1	1	1
2016-02-11	1	1	1	1	2	2	1	1	1	1	2	2	2	2	2	2
2016-02-17	1	1	0	0	1	1	2	2	1	1	1	1	2	2	2	2
2016-02-19	0	0	0	0	0	0	0	0	0	0	1	1	1	1	2	2
2016-02-21	1	1	1	1	2	2	2	2	2	2	1	1	1	1	1	1

Appendix B

Astrometric Solutions

CTYPE1 = ‘RA—TAN-SIP’ / TAN (gnomic) projection + SIP distortions
CTYPE2 = ‘DEC–TAN-SIP’ / TAN (gnomic) projection + SIP distortions
EQUINOX = 2000.0 / Equatorial coordinates definition (yr)
LONPOLE = 180.0 / no comment
LATPOLE = 0.0 / no comment
CRVAL1 = 339.993476555 / RA of reference point
CRVAL2 = -0.182345112321 / DEC of reference point
CRPIX1 = 897.692962722 / X reference pixel
CRPIX2 = 2101.80139878 / Y reference pixel
CUNIT1 = ‘deg ’ / X pixel scale units
CUNIT2 = ‘deg ’ / Y pixel scale units
CD1_1 = -1.42631876294E-06 / Transformation matrix
CD1_2 = -9.21061297676E-05 / no comment
CD2_1 = -9.21228170745E-05 / no comment
CD2_2 = 1.24533286537E-06 / no comment
IMAGEW = 2048 / Image width, in pixels.
IMAGEH = 4096 / Image height, in pixels.
A_ORDER = 2 / Polynomial order, axis 1
A_0_2 = -6.94851627342E-07 / no comment
A_1_1 = 1.11522341035E-06 / no comment
A_2_0 = -1.73980485103E-06 / no comment
B_ORDER = 2 / Polynomial order, axis 2
B_0_2 = 1.3973258662E-06 / no comment
B_1_1 = -8.73535263928E-07 / no comment
B_2_0 = 5.63709534756E-07 / no comment
AP_ORDER= 2 / Inv polynomial order, axis 1
AP_0_1 = -9.94935043145E-06 / no comment
AP_0_2 = 6.95551801661E-07 / no comment

AP_1_0 = 1.40078123895E-05 / no comment
AP_1_1 = -1.11780676932E-06 / no comment
AP_2_0 = 1.74057212421E-06 / no comment
BP_ORDER= 2 / Inv polynomial order, axis 2
BP_0_1 = 1.38832040856E-05 / no comment
BP_0_2 = -1.3982642172E-06 / no comment
BP_1_0 = -9.83238310444E-06 / no comment
BP_1_1 = 8.75389007572E-07 / no comment
BP_2_0 = -5.63071840054E-07 / no comment

Bibliography

Andrea V. Ahumada, Luis R. Vega-Neme, Juan J. Clariá, and Javier H. Minniti. Spectroscopic Fundamental Parameters of 16 Young Large Magellanic Cloud Star Clusters. *PASP*, 131(996):024101, Feb 2019. doi: 10.1088/1538-3873/aae660.

Shadab Alam, Franco D. Albareti, Carlos Allende Prieto, F. Anders, Scott F. Anderson, Timothy Anderton, Brett H. Andrews, Eric Armengaud, Éric Aubourg, Stephen Bailey, Sarbani Basu, Julian E. Bautista, Rachael L. Beaton, Timothy C. Beers, Chad F. Bender, Andreas A. Berlind, Florian Beutler, Vaishali Bhardwaj, Jonathan C. Bird, Dmitry Bizyaev, Cullen H. Blake, Michael R. Blanton, Michael Blomqvist, John J. Bochanski, Adam S. Bolton, Jo Bovy, A. Shelden Bradley, W. N. Brandt, D. E. Brauer, J. Brinkmann, Peter J. Brown, Joel R. Brownstein, Angela Burden, Etienne Burtin, Nicolás G. Busca, Zheng Cai, Diego Capozzi, Aurelio Carnero Rosell, Michael A. Carr, Ricardo Carrera, K. C. Chambers, William James Chaplin, Yen-Chi Chen, Cristina Chiappini, S. Drew Chojnowski, Chia-Hsun Chuang, Nicolas Clerc, Johan Comparat, Kevin Covey, Rupert A. C. Croft, Antonio J. Cuesta, Katia Cunha, Luiz N. da Costa, Nicola Da Rio, James R. A. Davenport, Kyle S. Dawson, Nathan De Lee, Timothée Delubac, Rohit Deshpande, Saurav Dhital, Letícia Dutra-Ferreira, Tom Dwelly, Anne Ealet, Garrett L. Ebelke, Edward M. Edmondson, Daniel J. Eisenstein, Tristan Ellsworth, Yvonne Elsworth, Courtney R. Epstein, Michael Eracleous, Stephanie Escoffier, Massimiliano Esposito, Michael L. Evans, Xiaohui Fan, Emma Fernández-Alvar, Diane Feuillet, Nurten Filiz Ak, Hayley Finley, Alexis Finoguenov, Kevin Flaherty, Scott W. Fleming, Andreu Font-Ribera, Jonathan Foster, Peter M. Frinchaboy, J. G. Galbraith-Frew, Rafael A. García, D. A. García-Hernández, Ana E. García Pérez, Patrick Gaulme, Jian Ge, R. Génova-Santos, A. Georgakakis, Luan Ghezzi, Bruce A. Gillespie, Léo Girardi, Daniel Goddard, Satya Gontcho A. Gontcho, Jonay I. González Hernández, Eva K. Grebel, Paul J. Green, Jan Niklas Grieb, Nolan Grieves, James E. Gunn, Hong Guo, Paul Harding, Sten Hasselquist, Suzanne L. Hawley, Michael Hayden, Fred R. Hearty, Saskia Hekker, Shirley Ho, David W. Hogg, Kelly Holley-Bockelmann, Jon A. Holtzman, Klaus Honscheid, Daniel Huber, Joseph Huehnerhoff, Inese I. Ivans, Linhua Jiang, Jennifer A. Johnson, Karen Kinemuchi, David Kirkby, Francisco Kitaura, Mark A. Klaene, Gillian R. Knapp, Jean-Paul Kneib, Xavier P. Koenig, Charles R. Lam, Ting-Wen Lan, Dustin Lang, Pierre Laurent, Jean-Marc Le Goff, Alexie Leauthaud, Khee-Gan Lee, Young Sun Lee, Timothy C. Licquia, Jian Liu, Daniel C. Long, Martín López-Corredoira, Diego Lorenzo-Oliveira, Sara Lucatello, Britt Lundgren, Robert H. Lupton, III Mack, Claude E., Suvrath Ma-

hadevan, Marcio A. G. Maia, Steven R. Majewski, Elena Malanushenko, Viktor Malanushenko, A. Manchado, Marc Manera, Qingqing Mao, Claudia Maraston, Robert C. Marchwinski, Daniel Margala, Sarah L. Martell, Marie Martig, Karen L. Masters, Savita Mathur, Cameron K. McBride, Peregrine M. McGehee, Ian D. McGreer, Richard G. McMahon, Brice Ménard, Marie-Luise Menzel, Andrea Merloni, Szabolcs Mészáros, Adam A. Miller, Jordi Miralda-Escudé, Hironao Miyatake, Antonio D. Montero-Dorta, Surhud More, Eric Morganson, Xan Morice-Atkinson, Heather L. Morrison, Benôit Mosser, Demitri Muna, Adam D. Myers, Kirpal Nand ra, Jeffrey A. Newman, Mark Neyrinck, Duy Cuong Nguyen, Robert C. Nichol, David L. Nidever, Pasquier Noterdaeme, Sebastián E. Nuza, Julia E. O'Connell, Robert W. O'Connell, Ross O'Connell, Ricardo L. C. Ogando, Matthew D. Olmstead, Audrey E. Oravetz, Daniel J. Oravetz, Keisuke Osumi, Russell Owen, Deborah L. Padgett, Nikhil Padmanabhan, Martin Paegert, Nathalie Palanque-Delabrouille, Kaike Pan, John K. Parejko, Isabelle Pâris, Changbom Park, Petchara Pattarakijwanich, M. Pellejero-Ibanez, Joshua Pepper, Will J. Percival, Ismael Pérez-Fournon, Ignasi Ṕrez-Ra'fols, Patrick Petitjean, Matthew M. Pieri, Marc H. Pinsonneault, Gustavo F. Porto de Mello, Francisco Prada, Abhishek Prakash, Adrian M. Price-Whelan, Pavlos Protopapas, M. Jordan Raddick, Mubdi Rahman, Beth A. Reid, James Rich, Hans-Walter Rix, Annie C. Robin, Constance M. Rockosi, Thaíse S. Rodrigues, Sergio Rodríguez-Torres, Natalie A. Roe, Ashley J. Ross, Nicholas P. Ross, Graziano Rossi, John J. Ruan, J. A. Rubiño-Martín, Eli S. Rykoff, Salvador Salazar-Albornoz, Mara Salvato, Lado Samushia, Ariel G. Sánchez, Basílio Santiago, Conor Sayres, Ricardo P. Schiavon, David J. Schlegel, Sarah J. Schmidt, Donald P. Schneider, Mathias Schultheis, Axel D. Schwope, C. G. Scóccola, Caroline Scott, Kris Sellgren, Hee-Jong Seo, Aldo Serenelli, Neville Shane, Yue Shen, Matthew Shetrone, Yiping Shu, V. Silva Aguirre, Thirupathi Sivarani, M. F. Skrutskie, Anže Slosar, Verne V. Smith, Flávia Sobreira, Diogo Souto, Keivan G. Stassun, Matthias Steinmetz, Dennis Stello, Michael A. Strauss, Alina Streblyanska, Nao Suzuki, Molly E. C. Swanson, Jonathan C. Tan, Jamie Tayar, Ryan C. Terrien, Aniruddha R. Thakar, Daniel Thomas, Neil Thomas, Benjamin A. Thompson, Jeremy L. Tinker, Rita Tojeiro, Nicholas W. Troup, Mariana Vargas-Magaña, Jose A. Vazquez, Licia Verde, Matteo Viel, Nicole P. Vogt, David A. Wake, Ji Wang, Benjamin A. Weaver, David H. Weinberg, Benjamin J. Weiner, Martin White, John C. Wilson, John P. Wisniewski, W. M. Wood-Vasey, Christophe Ye'che, Donald G. York, Nadia L. Zakamska, O. Zamora, Gail Zasowski, Idit Zehavi, Gong-Bo Zhao, Zheng Zheng, Xu Zhou, Zhimin Zhou, Hu Zou, and Guangtun Zhu. The Eleventh and Twelfth Data Releases of the Sloan Digital Sky Survey: Final Data from SDSS-III. *ApJS*, 219(1):12, July 2015. doi: 10.1088/0067-0049/219/1/12.

C. Alard. Image subtraction using a space-varying kernel. *A&AS*, 144:363–370, Jun 2000. doi: 10.1051/aas:2000214.

C. Alard and Robert H. Lupton. A Method for Optimal Image Subtraction. *ApJ*, 503 (1):325–331, Aug 1998. doi: 10.1086/305984.

C. Alcock, R. A. Allsman, T. S. Axelrod, D. P. Bennett, K. H. Cook, K. C. Freeman,

K. Griest, S. L. Marshall, B. A. Peterson, M. R. Pratt, P. J. Quinn, J. Reimann, A. W. Rodgers, C. W. Stubbs, W. Sutherland, and D. L. Welch. The MACHO Project LMC Variable Star Inventory.I.Beat Cepheids-Conclusive Evidence for the Excitation of the Second Overtone in Classical Cepheids. *AJ*, 109:1653, April 1995. doi: 10.1086/117392.

C. Alcock, R. A. Allsman, D. R. Alves, T. S. Axelrod, A. C. Becker, D. P. Bennett, D. F. Bersier, K. H. Cook, K. C. Freeman, K. Griest, J. A. Guern, M. Lehner, S. L. Marshall, D. Minniti, B. A. Peterson, M. R. Pratt, P. J. Quinn, A. W. Rodgers, C. W. Stubbs, W. Sutherland , A. Tomaney, T. Vandehei, and D. L. Welch. The MACHO Project LMC Variable Star Inventory. VIII. The Recent Star Formation History of the Large Magellanic Cloud from the Cepheid Period Distribution. *AJ*, 117(2):920–926, Feb 1999. doi: 10.1086/300736.

R. I. Anderson, H. Saio, S. Ekström, C. Georgy, and G. Meynet. On the effect of rotation on populations of classical Cepheids. II. Pulsation analysis for metallicities 0.014, 0.006, and 0.002. *A&A*, 591:A8, June 2016. doi: 10.1051/0004-6361/201528031.

Richard I. Anderson, Sylvia Ekström, Cyril Georgy, Georges Meynet, Nami Mowlavi, and Laurent Eyer. On the effect of rotation on populations of classical Cepheids. I. Predictions at solar metallicity. *A&A*, 564:A100, April 2014. doi: 10.1051/0004-6361/201322988.

E. Athanassoula and Rachael Lynn Beaton. Unravelling the mystery of the M31 bar. *MNRAS*, 370(3):1499–1512, August 2006. doi: 10.1111/j.1365-2966.2006.10567.x.

W. Baade. Über eine Möglichkeit, die Pulsationstheorie der δ Cephei-Veränderlichen zu prüten. *Astronomische Nachrichten*, 228:359, October 1926. doi: 10.1002/asna.19262282003.

N. Baker and R. Kippenhahn. The Pulsations of Models of δ Cephei Stars. With 17 Figures in the Text. *Zeitschrift fur Astrophysik*, 54:114, January 1962.

Norman Baker and Rudolf Kippenhahn. The Pulsations of Models of Delta Cephei Stars. II. *ApJ*, 142:868, October 1965. doi: 10.1086/148359.

N. Bastian and E. Silva-Villa. Constraints on possible age spreads within young massive clusters in the large Magellanic cloud. *MNRAS*, 431:L122–L126, Apr 2013. doi: 10.1093/mnrasl/slt024.

Michael A. Beasley, Izaskun San Roman, Carme Gallart, Ata Sarajedini, and Antonio Aparicio. Evidence for temporal evolution in the M33 disc as traced by its star clusters. *MNRAS*, 451(4):3400–3418, August 2015. doi: 10.1093/mnras/stv943.

J. P. Beaulieu, J. Robert Buchler, J. B. Marquette, J. D. Hartman, and A. Schwarzenberg-Czerny. Detection of Beat Cepheids in M33 and Their Use as a Probe of the M33 Metallicity Distribution. *ApJ*, 653:L101–L104, December 2006. doi: 10.1086/510453.

Andrew Becker. HOTPANTS: High Order Transform of PSF ANd Template Subtraction. Astrophysics Source Code Library, April 2015.

E. Bertin and S. Arnouts. SExtractor: Software for source extraction. *Astronomy and Astrophysics Supplement Series*, 117:393–404, June 1996. doi: 10.1051/aas:1996164.

F. W. Bessel. On the parallax of 61 Cygni. *MNRAS*, 4:152–161, November 1838. doi: 10.1093/mnras/4.17.152.

G. Bono, M. Marconi, S. Cassisi, F. Caputo, W. Gieren, and G. Pietrzynski. Classical Cepheid Pulsation Models. X. The Period-Age Relation. *ApJ*, 621:966–977, March 2005. doi: 10.1086/427744.

Giuseppe Bono and Marcella Marconi. Cepheids in NGC 1866: a test for pulsational models. *MNRAS*, 290(2):353–359, September 1997. doi: 10.1093/mnras/290.2.353.

Giuseppe Bono, Filippina Caputo, Vittorio Castellani, and Marcella Marconi. Theoretical Models for Classical Cepheids. II. Period-Luminosity, Period-Color, and Period-Luminosity-Color Relations. *ApJ*, 512(2):711–723, February 1999. doi: 10.1086/306815.

Giuseppe Bono, Filippina Caputo, Santi Cassisi, Marcella Marconi, Luciano Piersanti, and Amedeo Tornambè. Intermediate-Mass Star Models with Different Helium and Metal Contents. *ApJ*, 543:955–971, November 2000. doi: 10.1086/317156.

Fabio Bresolin. The Abundance Scatter in M33 from H II Regions: Is There Any Evidence for Azimuthal Metallicity Variations? *ApJ*, 730(2):129, Apr 2011. doi: 10.1088/0004-637X/730/2/129.

J. Robert Buchler. Beat Cepheids as Probes of Stellar and Galactic Metallicity. II. Opacities with the AGS Mixture. *ApJ*, 680:1412–1416, June 2008. doi: 10.1086/588547.

J. Robert Buchler and Róbert Szabó. Beat Cepheids as Probes of Stellar and Galactic Metallicity. *ApJ*, 660:723–731, May 2007. doi: 10.1086/513071.

F. Caputo, M. Marconi, I. Musella, and P. Santolamazza. Theoretical models for classical Cepheids. VII. Metallicity effects on the Cepheid distance scale. *A&A*, 359:1059–1067, July 2000.

F. Caputo, V. Castellani, S. Degl'Innocenti, G. Fiorentino, and M. Marconi. Bright metal-poor variables: Why "Anomalous" Cepheids? *A&A*, 424:927–934, September 2004. doi: 10.1051/0004-6361:20040307.

Jørgen Christensen-Dalsgaard. Asteroseismology. *Ap&SS*, 261:1–12, January 1998. doi: 10.1023/A:1002067301259.

M. R. L. Cioni. The metallicity gradient as a tracer of history and structure: the Magellanic Clouds and M33 galaxies. *A&A*, 506(3):1137–1146, Nov 2009. doi: 10.1051/0004-6361/200912138.

E. Corbelli, S. Verley, B. G. Elmegreen, and C. Giovanardi. The cluster birthline in M 33. *A&A*, 495(2):479–490, February 2009. doi: 10.1051/0004-6361:200811086.

Nathan R. Crockett, Donald R. Garnett, Philip Massey, and George Jacoby. Neon and Oxygen Abundances in M33. *ApJ*, 637(2):741–751, Feb 2006. doi: 10.1086/498424.

Richard de Grijs. *An Introduction to Distance Measurement in Astronomy*. Wiley-Blackwell Acad. Publ., 2011.

R. G. Deupree. The theoretical red edge of the RR Lyrae gap. IV. Convective steady-state models. *ApJ*, 215:620–623, July 1977. doi: 10.1086/155396.

J. Devor. Solutions for 10,000 Eclipsing Binaries in the Bulge Fields of OGLE II Using DEBiL. *ApJ*, 628:411–425, July 2005. doi: 10.1086/431170.

G. P. Di Benedetto. Improved Calibration of Cosmic Distance Scale by Cepheid Pulsation Parallaxes. *ApJ*, 486:60–74, September 1997. doi: 10.1086/304496.

A. S. Eddington. The pulsation theory of Cepheid variables. *The Observatory*, 40: 290–293, August 1917.

A. S. Eddington. The problem of the Cepheid variables. *MNRAS*, 79:2, November 1918.

Yu. N. Efremov. The period-age relation for Cepheids. *Soviet Ast.*, 22:161, April 1978.

Yu. N. Efremov. Cepheids in LMC Clusters and the Period-Age Relation. *Astronomy Reports*, 47:1000–1012, December 2003. doi: 10.1134/1.1633613.

ESA. The HIPPARCOS and TYCHO catalogues. Astrometric and photometric star catalogues derived from the ESA HIPPARCOS Space Astrometry Mission. 1200, January 1997.

M. W. Feast and R. M. Catchpole. The Cepheid period-luminosity zero-point from HIPPARCOS trigonometrical parallaxes. *MNRAS*, 286:L1–L5, March 1997. doi: 10.1093/mnras/286.1.L1.

Philippe Fischer, Carlton Pryor, Stephen Murray, Mario Mateo, and Tom Richtler. Mass Segregation in Young Large Magellanic Cloud Clusters. I. NGC 2157. *AJ*, 115(2):592–604, February 1998. doi: 10.1086/300212.

Wendy L. Freedman. Correction: Cosmology at a crossroads. *Nature Astronomy*, 1: 0169, June 2017. doi: 10.1038/s41550-017-0169.

Gaia Collaboration, T. Prusti, J. H. J. de Bruijne, A. G. A. Brown, A. Vallenari, C. Babusiaux, C. A. L. Bailer-Jones, U. Bastian, M. Biermann, D. W. Evans, and et al. The Gaia mission. *A&A*, 595:A1, November 2016. doi: 10.1051/0004-6361/201629272.

Gaia Collaboration, A. G. A. Brown, A. Vallenari, T. Prusti, J. H. J. de Bruijne, C. Babusiaux, C. A. L. Bailer-Jones, M. Biermann, D. W. Evans, L. Eyer, and et al. Gaia Data Release 2. Summary of the contents and survey properties. *A&A*, 616: A1, August 2018. doi: 10.1051/0004-6361/201833051.

A. Gallenne, P. Kervella, A. Mérand, G. Pietrzyński, W. Gieren, N. Nardetto, and B. Trahin. Observational calibration of the projection factor of Cepheids. IV. Period-projection factor relation of Galactic and Magellanic Cloud Cepheids. *A&A*, 608: A18, Nov 2017. doi: 10.1051/0004-6361/201731589.

D. R. Garnett, G. A. Shields, E. D. Skillman, S. P. Sagan, and R. J. Dufour. Interstellar Abundance Gradients in NGC 2403: Comparison to M33. *ApJ*, 489:63–86, November 1997. doi: 10.1086/304775.

K. Genovali, B. Lemasle, G. Bono, M. Romaniello, M. Fabrizio, I. Ferraro, G. Iannicola, C. D. Laney, M. Nonino, M. Bergemann, R. Buonanno, P. François, L. Inno, R. P. Kudritzki, N. Matsunaga, S. Pedicelli, F. Primas, and F. Thévenin. On the fine structure of the Cepheid metallicity gradient in the Galactic thin disk. *A&A*, 566: A37, June 2014. doi: 10.1051/0004-6361/201323198.

C. Georgy, S. Ekström, P. Eggenberger, G. Meynet, L. Haemmerlé, A. Maeder, A. Granada, J. H. Groh, R. Hirschi, N. Mowlavi, N. Yusof, C. Charbonnel, T. Decressin, and F. Barblan. Grids of stellar models with rotation. III. Models from 0.8 to 120 $M_{\odot}$ at a metallicity Z = 0.002. *A&A*, 558:A103, October 2013a. doi: 10.1051/0004-6361/201322178.

C. Georgy, S. Ekström, A. Granada, G. Meynet, N. Mowlavi, P. Eggenberger, and A. Maeder. Populations of rotating stars. I. Models from 1.7 to 15 $M_{\odot}$ at Z = 0.014, 0.006, and 0.002 with Ω/Ω_{crit} between 0 and 1. *A&A*, 553:A24, May 2013b. doi: 10.1051/0004-6361/201220558.

J. D. Hartman and G. Á. Bakos. VARTOOLS: A program for analyzing astronomical time-series data. *Astronomy and Computing*, 17:1–72, October 2016. doi: 10.1016/j.ascom.2016.05.006.

J. D. Hartman, D. Bersier, K. Z. Stanek, J. P. Beaulieu, J. Kaluzny, J. B. Marquette, P. B. Stetson, and A. Schwarzenberg-Czerny. Deep Canada-France-Hawaii Telescope photometric survey of the entire M33 galaxy - I. Catalogue of 36000 variable point sources. *MNRAS*, 371:1405–1417, September 2006. doi: 10.1111/j.1365-2966.2006.10764.x.

Jon A. Holtzman, Christopher J. Burrows, Stefano Casertano, J. Jeff Hester, John T. Trauger, Alan M. Watson, and Guy Worthey. The Photometric Performance and Calibration of WFPC2. *PASP*, 107:1065, November 1995. doi: 10.1086/133664.

Edwin Hubble. A Relation between Distance and Radial Velocity among Extra-Galactic Nebulae. *Proceedings of the National Academy of Science*, 15:168–173, March 1929. doi: 10.1073/pnas.15.3.168.

Željko Ivezić, Steven M. Kahn, J. Anthony Tyson, Bob Abel, Emily Acosta, Robyn Allsman, David Alonso, Yusra AlSayyad, Scott F. Anderson, John Andrew, James Roger P. Angel, George Z. Angeli, Reza Ansari, Pierre Antilogus, Constanza Araujo, Robert Armstrong, Kirk T. Arndt, Pierre Astier, Éric Aubourg, Nicole Auza, Tim S. Axelrod, Deborah J. Bard, Jeff D. Barr, Aurelian Barrau, James G. Bartlett, Amanda E. Bauer, Brian J. Bauman, Sylvain Baumont, Ellen Bechtol, Keith Bechtol, Andrew C. Becker, Jacek Becla, Cristina Beldica, Steve Bellavia, Federica B. Bianco, Rahul Biswas, Guillaume Blanc, Jonathan Blazek, Roger D. Bland ford, Josh S. Bloom, Joanne Bogart, Tim W. Bond, Michael T. Booth, Anders W. Borgland, Kirk Borne, James F. Bosch, Dominique Boutigny, Craig A. Brackett, Andrew Bradshaw, William Nielsen Brand t, Michael E. Brown, James S. Bullock, Patricia Burchat, David L. Burke, Gianpietro Cagnoli, Daniel Calabrese, Shawn Callahan, Alice L. Callen, Jeffrey L. Carlin, Erin L. Carlson, Srinivasan Chand rasekharan, Glenaver Charles-Emerson, Steve Chesley, Elliott C. Cheu, Hsin-Fang Chiang, James Chiang, Carol Chirino, Derek Chow, David R. Ciardi, Charles F. Claver, Johann Cohen-Tanugi, Joseph J. Cockrum, Rebecca Coles, Andrew J. Connolly, Kem H. Cook, Asantha Cooray, Kevin R. Covey, Chris Cribbs, Wei Cui, Roc Cutri, Philip N. Daly, Scott F. Daniel, Felipe Daruich, Guillaume Daubard, Greg Daues, William Dawson, Francisco Delgado, Alfred Dellapenna, Robert de Peyster, Miguel de Val-Borro, Seth W. Digel, Peter Doherty, Richard Dubois, Gregory P. Dubois-Felsmann, Josef Durech, Frossie Economou, Tim Eifler, Michael Eracleous, Benjamin L. Emmons, Angelo Fausti Neto, Henry Ferguson, Enrique Figueroa, Merlin Fisher-Levine, Warren Focke, Michael D. Foss, James Frank, Michael D. Freemon, Emmanuel Gangler, Eric Gawiser, John C. Geary, Perry Gee, Marla Geha, Charles J. B. Gessner, Robert R. Gibson, D. Kirk Gilmore, Thomas Glanzman, William Glick, Tatiana Goldina, Daniel A. Goldstein, Iain Goodenow, Melissa L. Graham, William J. Gressler, Philippe Gris, Leanne P. Guy, Augustin Guyonnet, Gunther Haller, Ron Harris, Patrick A. Hascall, Justine Haupt, Fabio Hernand ez, Sven Herrmann, Edward Hileman, Joshua Hoblitt, John A. Hodgson, Craig Hogan, James D. Howard, Dajun Huang, Michael E. Huffer, Patrick Ingraham, Walter R. Innes, Suzanne H. Jacoby, Bhuvnesh Jain, Fabrice Jammes, M. James Jee, Tim Jenness, Garrett Jernigan, Darko Jevremović, Kenneth Johns, Anthony S. Johnson, Margaret W. G. Johnson, R. Lynne Jones, Claire Juramy-Gilles, Mario Jurić, Jason S. Kalirai, Nitya J. Kallivayalil, Bryce Kalmbach, Jeffrey P. Kantor, Pierre Karst, Mansi M. Kasliwal, Heather Kelly, Richard Kessler, Veronica Kinnison, David Kirkby, Lloyd Knox, Ivan V. Kotov, Victor L. Krabbendam, K. Simon Krughoff, Petr Kubánek, John Kuczewski, Shri Kulkarni, John Ku, Nadine R. Kurita, Craig S. Lage, Ron Lambert, Travis Lange, J. Brian Langton, Laurent Le Guillou, Deborah Levine, Ming Liang, Kian-Tat Lim, Chris J. Lintott, Kevin E. Long, Margaux Lopez, Paul J. Lotz, Robert H. Lupton, Nate B. Lust, Lauren A. MacArthur, Ashish Mahabal, Rachel Mand elbaum, Thomas W. Markiewicz, Darren S. Marsh, Philip J. Marshall, Stuart Marshall, Morgan May, Robert McKercher, Michelle McQueen, Joshua Meyers, Myriam Migliore, Michelle Miller, David J. Mills, Connor Miraval, Joachim Moeyens, Fred E. Moolekamp, David G. Monet, Marc Moniez, Serge Monkewitz, Christopher Montgomery, Christopher B. Morrison, Fritz Mueller, Gary P. Muller, Freddy Muñoz Arancibia, Douglas R. Neill, Scott P. Newbry, Jean-Yves Nief, An-

drei Nomerotski, Martin Nordby, Paul O'Connor, John Oliver, Scot S. Olivier, Knut Olsen, William O'Mullane, Sandra Ortiz, Shawn Osier, Russell E. Owen, Reynald Pain, Paul E. Palecek, John K. Parejko, James B. Parsons, Nathan M. Pease, J. Matt Peterson, John R. Peterson, Donald L. Petravick, M. E. Libby Petrick, Cathy E. Petry, Francesco Pierfederici, Stephen Pietrowicz, Rob Pike, Philip A. Pinto, Raymond Plante, Stephen Plate, Joel P. Plutchak, Paul A. Price, Michael Prouza, Veljko Radeka, Jayadev Rajagopal, Andrew P. Rasmussen, Nicolas Regnault, Kevin A. Reil, David J. Reiss, Michael A. Reuter, Stephen T. Ridgway, Vincent J. Riot, Steve Ritz, Sean Robinson, William Roby, Aaron Roodman, Wayne Rosing, Cecille Roucelle, Matthew R. Rumore, Stefano Russo, Abhijit Saha, Benoit Sassolas, Terry L. Schalk, Pim Schellart, Rafe H. Schindler, Samuel Schmidt, Donald P. Schneider, Michael D. Schneider, William Schoening, German Schumacher, Megan E. Schwamb, Jacques Sebag, Brian Selvy, Glenn H. Sembroski, Lynn G. Seppala, Andrew Serio, Eduardo Serrano, Richard A. Shaw, Ian Shipsey, Jonathan Sick, Nicole Silvestri, Colin T. Slater, J. Allyn Smith, R. Chris Smith, Shahram Sobhani, Christine Soldahl, Lisa Storrie-Lombardi, Edward Stover, Michael A. Strauss, Rachel A. Street, Christopher W. Stubbs, Ian S. Sullivan, Donald Sweeney, John D. Swinbank, Alexander Szalay, Peter Takacs, Stephen A. Tether, Jon J. Thaler, John Gregg Thayer, Sandrine Thomas, Adam J. Thornton, Vaikunth Thukral, Jeffrey Tice, David E. Trilling, Max Turri, Richard Van Berg, Daniel Vanden Berk, Kurt Vetter, Francoise Virieux, Tomislav Vucina, William Wahl, Lucianne Walkowicz, Brian Walsh, Christopher W. Walter, Daniel L. Wang, Shin-Yawn Wang, Michael Warner, Oliver Wiecha, Beth Willman, Scott E. Winters, David Wittman, Sidney C. Wolff, W. Michael Wood-Vasey, Xiuqin Wu, Bo Xin, Peter Yoachim, and Hu Zhan. LSST: From Science Drivers to Reference Design and Anticipated Data Products. *ApJ*, 873(2):111, Mar 2019. doi: 10.3847/1538-4357/ab042c.

N. V. Kharchenko, A. E. Piskunov, E. Schilbach, S. Röser, and R. D. Scholz. Global survey of star clusters in the Milky Way. I. The pipeline and fundamental parameters in the second quadrant. *A&A*, 543:A156, July 2012. doi: 10.1051/0004-6361/201118708.

Minsun Kim, Eunhyeuk Kim, Myung Gyoon Lee, Ata Sarajedini, and Doug Geisler. Determination of the Distance to M33 Based on the Tip of the Red Giant Branch and the Red Clump. *AJ*, 123(1):244–254, Jan 2002. doi: 10.1086/324639.

R. Kippenhahn and L. Smith. On the ages of delta Cephei stars. *A&A*, 1:142, February 1969.

E. Komatsu, K. M. Smith, J. Dunkley, C. L. Bennett, B. Gold, G. Hinshaw, N. Jarosik, D. Larson, M. R. Nolta, L. Page, D. N. Spergel, M. Halpern, R. S. Hill, A. Kogut, M. Limon, S. S. Meyer, N. Odegard, G. S. Tucker, J. L. Weiland, E. Wollack, and E. L. Wright. Seven-year Wilkinson Microwave Anisotropy Probe (WMAP) Observations: Cosmological Interpretation. *The Astrophysical Journal Supplement Series*, 192:18, February 2011. doi: 10.1088/0067-0049/192/2/18.

V. Kovtyukh, B. Lemasle, F. Chekhonadskikh, G. Bono, N. Matsunaga, A. Yushchenko, R. I. Anderson, S. Belik, R. da Silva, and L. Inno. The chemi-

cal composition of Galactic beat Cepheids. *MNRAS*, 460:2077–2086, August 2016. doi: 10.1093/mnras/stw1113.

Henrietta S. Leavitt. 1777 variables in the Magellanic Clouds. *Annals of Harvard College Observatory*, 60:87–108.3, January 1908.

Henrietta S. Leavitt and Edward C. Pickering. Periods of 25 Variable Stars in the Small Magellanic Cloud. *Harvard College Observatory Circular*, 173:1–3, March 1912.

C. H. Lee, M. Kodric, S. Seitz, A. Riffeser, J. Koppenhoefer, R. Bender, U. Hopp, C. Gössl, J. Snigula, W. S. Burgett, K. C. Chambers, H. Flewelling, K. W. Hodapp, N. Kaiser, R. P. Kudritzki, P. A. Price, J. L. Tonry, and R. J. Wainscoat. Properties of M31. III. Candidate Beat Cepheids from PS1 PAndromeda Data and Their Implication on Metallicity Gradient. *ApJ*, 777:35, November 2013. doi: 10.1088/0004-637X/777/1/35.

Myung Gyoon Lee, Wendy L. Freedman, and Barry F. Madore. The Tip of the Red Giant Branch as a Distance Indicator for Resolved Galaxies. *ApJ*, 417:553, November 1993. doi: 10.1086/173334.

B. Lemasle, M. A. T. Groenewegen, E. K. Grebel, G. Bono, G. Fiorentino, P. François, L. Inno, V. V. Kovtyukh, N. Matsunaga, S. Pedicelli, F. Primas, J. Pritchard, M. Romaniello, and R. da Silva. Detailed chemical composition of classical Cepheids in the LMC cluster NGC 1866 and in the field of the SMC. *A&A*, 608:A85, December 2017. doi: 10.1051/0004-6361/201731370.

Zesen Lin, Ning Hu, Xu Kong, Yulong Gao, Hu Zou, Enci Wang, Fuzhen Cheng, Guanwen Fang, Lin Lin, and Jing Wang. Spectroscopic Observation and Analysis of H II Regions in M33 with MMT: Temperatures and Oxygen Abundances. *ApJ*, 842:97, June 2017. doi: 10.3847/1538-4357/aa6f14.

L. Lindegren, J. Hernández, A. Bombrun, S. Klioner, U. Bastian, M. Ramos-Lerate, A. de Torres, H. Steidelmüller, C. Stephenson, D. Hobbs, U. Lammers, M. Biermann, R. Geyer, T. Hilger, D. Michalik, U. Stampa, P. J. McMillan, J. Castañeda, M. Clotet, G. Comoretto, M. Davidson, C. Fabricius, G. Gracia, N. C. Hambly, A. Hutton, A. Mora, J. Portell, F. van Leeuwen, U. Abbas, A. Abreu, M. Altmann, A. Andrei, E. Anglada, L. Balaguer-Núñez, C. Barache, U. Becciani, S. Bertone, L. Bianchi, S. Bouquillon, G. Bourda, T. Brüsemeister, B. Bucciarelli, D. Busonero, R. Buzzi, R. Cancelliere, T. Carlucci, P. Charlot, N. Cheek, M. Crosta, C. Crowley, J. de Bruijne, F. de Felice, R. Drimmel, P. Esquej, A. Fienga, E. Fraile, M. Gai, N. Garralda, J. J. González-Vidal, R. Guerra, M. Hauser, W. Hofmann, B. Holl, S. Jordan, M. G. Lattanzi, H. Lenhardt, S. Liao, E. Licata, T. Lister, W. Löffler, J. Marchant, J.-M. Martin-Fleitas, R. Messineo, F. Mignard, R. Morbidelli, E. Poggio, A. Riva, N. Rowell, E. Salguero, M. Sarasso, E. Sciacca, H. Siddiqui, R. L. Smart, A. Spagna, I. Steele, F. Taris, J. Torra, A. van Elteren, W. van Reeven, and A. Vecchiato. Gaia Data Release 2. The astrometric solution. *A&A*, 616:A2, August 2018. doi: 10.1051/0004-6361/201832727.

W. J. Maciel, R. D. D. Costa, and M. M. M. Uchida. An estimate of the time variation of the O/H radial gradient from planetary nebulae. *A&A*, 397:667–674, Jan 2003. doi: 10.1051/0004-6361:20021530.

L. M. Macri, K. Z. Stanek, D. Bersier, L. J. Greenhill, and M. J. Reid. A New Cepheid Distance to the Maser-Host Galaxy NGC 4258 and Its Implications for the Hubble Constant. *ApJ*, 652(2):1133–1149, December 2006. doi: 10.1086/508530.

B. F. Madore. The period-luminosity relation. IV. Intrinsic relations and reddenings for the Large Magellanic Cloud Cepheids. *ApJ*, 253:575–579, February 1982. doi: 10.1086/159659.

Barry F. Madore and Wendy L. Freedman. The Cepheid Distance Scale. *PASP*, 103: 933, September 1991. doi: 10.1086/132911.

Barry F. Madore and Wendy L. Freedman. Concerning the Slope of the Cepheid Period-Luminosity Relation. *ApJ*, 696(2):1498–1501, May 2009. doi: 10.1088/0004-637X/696/2/1498.

A. Maeder and G. Meynet. Stellar evolution with rotation. VI. The Eddington and Omega -limits, the rotational mass loss for OB and LBV stars. *A&A*, 361:159–166, September 2000.

Violet A. Mager, Barry F. Madore, and Wendy L. Freedman. The Metallicity Dependence of the Cepheid P - L Relation in M101. *ApJ*, 777(1):79, November 2013. doi: 10.1088/0004-637X/777/1/79.

Laura Magrini, Letizia Stanghellini, and Eva Villaver. The Planetary Nebula Population of M33 and its Metallicity Gradient: A Look Into the Galaxy's Distant Past. *ApJ*, 696(1):729–740, May 2009. doi: 10.1088/0004-637X/696/1/729.

Laura Magrini, Lodovico Coccato, Letizia Stanghellini, Viviana Casasola, and Daniele Galli. Metallicity gradients in local Universe galaxies: Time evolution and effects of radial migration. *A&A*, 588:A91, Apr 2016. doi: 10.1051/0004-6361/201527799.

M. Marconi, I. Musella, and G. Fiorentino. Cepheid Pulsation Models at Varying Metallicity and $\Delta Y/\Delta Z$. *ApJ*, 632(1):590–610, October 2005. doi: 10.1086/432790.

Mario Mateo. Tuning the Cepheid Distance Scale. *PASP*, 104:824, Sep 1992. doi: 10.1086/133061.

A. P. Milone, A. F. Marino, M. Di Criscienzo, F. D'Antona, L. R. Bedin, G. Da Costa, G. Piotto, M. Tailo, A. Dotter, and R. Angeloni. Multiple stellar populations in Magellanic Cloud clusters - VI. A survey of multiple sequences and Be stars in young clusters. *MNRAS*, 477(2):2640–2663, Jun 2018. doi: 10.1093/mnras/sty661.

Pawel Moskalik, J. R. Buchler, and Ariel Marom. Toward a Resolution of the Bump and Beat Cepheid Mass Discrepancies. *ApJ*, 385:685, February 1992. doi: 10.1086/170975.

J. R. Mould, D. A. Xystus, and G. S. Da Costa. The Age of the Large Magellanic Cloud Cluster NGC 2031. *ApJ*, 408:108, May 1993. doi: 10.1086/172573.

F. Niederhofer, M. Hilker, N. Bastian, and E. Silva-Villa. No evidence for significant age spreads in young massive LMC clusters. *A&A*, 575:A62, March 2015. doi: 10.1051/0004-6361/201424455.

E. Noyola and K. Gebhardt. Surface Brightness Profiles for a Sample of LMC, SMC, and Fornax Galaxy Globular Clusters. *AJ*, 134(3):912–925, Sep 2007. doi: 10.1086/520061.

M. Pasquato and G. Bertin. On the fundamental line of galactic and extragalactic globular clusters. *A&A*, 512:A35, Mar 2010. doi: 10.1051/0004-6361/200912947.

J. O. Petersen. Masses of double mode cepheid variables determined by analysis of period ratios. *A&A*, 27:89, August 1973.

M. M. Phillips. The Absolute Magnitudes of Type IA Supernovae. *ApJ*, 413:L105, August 1993. doi: 10.1086/186970.

Adriano Pietrinferni, Santi Cassisi, Maurizio Salaris, and Fiorella Castelli. A Large Stellar Evolution Database for Population Synthesis Studies. I. Scaled Solar Models and Isochrones. *ApJ*, 612:168–190, September 2004. doi: 10.1086/422498.

Adriano Pietrinferni, Santi Cassisi, Maurizio Salaris, and Fiorella Castelli. A Large Stellar Evolution Database for Population Synthesis Studies. II. Stellar Models and Isochrones for an α-enhanced Metal Distribution. *ApJ*, 642:797–812, May 2006. doi: 10.1086/501344.

Planck Collaboration, N. Aghanim, Y. Akrami, M. Ashdown, J. Aumont, C. Baccigalupi, M. Ballardini, A. J. Banday, R. B. Barreiro, N. Bartolo, S. Basak, R. Battye, K. Benabed, J. P. Bernard, M. Bersanelli, P. Bielewicz, J. J. Bock, J. R. Bond, J. Borrill, F. R. Bouchet, F. Boulanger, M. Bucher, C. Burigana, R. C. Butler, E. Calabrese, J. F. Cardoso, J. Carron, A. Challinor, H. C. Chiang, J. Chluba, L. P. L. Colombo, C. Combet, D. Contreras, B. P. Crill, F. Cuttaia, P. de Bernardis, G. de Zotti, J. Delabrouille, J. M. Delouis, E. Di Valentino, J. M. Diego, O. Doré, M. Douspis, A. Ducout, X. Dupac, S. Dusini, G. Efstathiou, F. Elsner, T. A. Enßlin, H. K. Eriksen, Y. Fantaye, M. Farhang, J. Fergusson, R. Fernandez-Cobos, F. Finelli, F. Forastieri, M. Frailis, A. A. Fraisse, E. Franceschi, A. Frolov, S. Galeotta, S. Galli, K. Ganga, R. T. Génova-Santos, M. Gerbino, T. Ghosh, J. González-Nuevo, K. M. Górski, S. Gratton, A. Gruppuso, J. E. Gudmundsson, J. Hamann, W. Handley, F. K. Hansen, D. Herranz, S. R. Hildebrandt, E. Hivon, Z. Huang, A. H. Jaffe, W. C. Jones, A. Karakci, E. Keihänen, R. Keskitalo, K. Kiiveri, J. Kim, T. S. Kisner, L. Knox, N. Krachmalnicoff, M. Kunz, H. Kurki-Suonio, G. Lagache, J. M. Lamarre, A. Lasenby, M. Lattanzi, C. R. Lawrence, M. Le Jeune, P. Lemos, J. Lesgourgues, F. Levrier, A. Lewis, M. Liguori, P. B. Lilje, M. Lilley, V. Lindholm, M. López-Caniego, P. M. Lubin, Y. Z. Ma, J. F. Macías-Pérez, G. Maggio, D. Maino, N. Mandolesi, A. Mangilli, A. Marcos-Caballero, M. Maris, P. G. Martin, M. Martinelli, E. Martínez-González, S. Matarrese, N. Mauri, J. D. McEwen,

P. R. Meinhold, A. Melchiorri, A. Mennella, M. Migliaccio, M. Millea, S. Mitra, M. A. Miville-Deschênes, D. Molinari, L. Montier, G. Morgante, A. Moss, P. Natoli, H. U. Nørgaard-Nielsen, L. Pagano, D. Paoletti, B. Partridge, G. Patanchon, H. V. Peiris, F. Perrotta, V. Pettorino, F. Piacentini, L. Polastri, G. Polenta, J. L. Puget, J. P. Rachen, M. Reinecke, M. Remazeilles, A. Renzi, G. Rocha, C. Rosset, G. Roudier, J. A. Rubiño-Martín, B. Ruiz-Granados, L. Salvati, M. Sandri, M. Savelainen, D. Scott, E. P. S. Shellard, C. Sirignano, G. Sirri, L. D. Spencer, R. Sunyaev, A. S. Suur-Uski, J. A. Tauber, D. Tavagnacco, M. Tenti, L. Toffolatti, M. Tomasi, T. Trombetti, L. Valenziano, J. Valiviita, B. Van Tent, L. Vibert, P. Vielva, F. Villa, N. Vittorio, B. D. Wand elt, I. K. Wehus, M. White, S. D. M. White, A. Zacchei, and A. Zonca. Planck 2018 results. VI. Cosmological parameters. *arXiv e-prints*, art. arXiv:1807.06209, July 2018.

Adam G. Riess, Lucas M. Macri, Samantha L. Hoffmann, Dan Scolnic, Stefano Casertano, Alexei V. Filippenko, Brad E. Tucker, Mark J. Reid, David O. Jones, Jeffrey M. Silverman, Ryan Chornock, Peter Challis, Wenlong Yuan, Peter J. Brown, and Ryan J. Foley. A 2.4% Determination of the Local Value of the Hubble Constant. *ApJ*, 826(1):56, July 2016. doi: 10.3847/0004-637X/826/1/56.

M. Romaniello, F. Primas, M. Mottini, M. Groenewegen, G. Bono, and P. François. The influence of chemical composition on the properties of Cepheid stars. I. Period-Luminosity relation vs. iron abundance. *A&A*, 429:L37–L40, January 2005. doi: 10.1051/0004-6361:200400110.

Erik Rosolowsky and Joshua D. Simon. The M33 Metallicity Project: Resolving the Abundance Gradient Discrepancies in M33. *ApJ*, 675(2):1213–1222, Mar 2008. doi: 10.1086/527407.

Maurizio Salaris and Santi Cassisi. The 'tip' of the red giant branch as a distance indicator: results from evolutionary models. *MNRAS*, 289:406–414, August 1997. doi: 10.1093/mnras/289.2.406.

S. Salmon, J. Montalbán, T. Morel, A. Miglio, M. A. Dupret, and A. Noels. Testing the effects of opacity and the chemical mixture on the excitation of pulsations in B stars of the Magellanic Clouds. *MNRAS*, 422(4):3460–3474, June 2012. doi: 10.1111/j.1365-2966.2012.20857.x.

Allan Sandage, A. Saha, G. A. Tammann, Nino Panagia, and D. Macchetto. The Cepheid Distance to IC 4182: Calibration of M V(max) for SN IA 1937C and the Value of H 0. *ApJ*, 401:L7, December 1992. doi: 10.1086/186657.

J. F. C. Santos, Jr., E. Bica, J. J. Claria, A. E. Piatti, L. A. Girardi, and H. Dottori. Blue-violet spectral evolution of young Magellanic Cloud clusters. *MNRAS*, 276: 1155–1178, October 1995. doi: 10.1093/mnras/276.4.1155.

S. Schmeja, N. V. Kharchenko, A. E. Piskunov, S. Röser, E. Schilbach, D. Froebrich, and R. D. Scholz. Global survey of star clusters in the Milky Way. III. 139 new open clusters at high Galactic latitudes. *A&A*, 568:A51, August 2014. doi: 10.1051/0004-6361/201322720.

A. Schwarzenberg-Czerny. On the advantage of using analysis of variance for period search. *MNRAS*, 241:153–165, November 1989. doi: 10.1093/mnras/241.2.153.

V. Scowcroft, D. Bersier, J. R. Mould, and P. R. Wood. The effect of metallicity on Cepheid magnitudes and the distance to M33. *MNRAS*, 396:1287–1296, July 2009. doi: 10.1111/j.1365-2966.2009.14822.x.

Dava Sobel. Henrietta Leavitt, Cecilia Payne Gaposchkin and the women of Harvard Observatory. In *APS April Meeting Abstracts*, volume 2018 of *APS Meeting Abstracts*, page U07.001, January 2018.

I. Soszyński, R. Poleski, A. Udalski, M. K. Szymański, M. Kubiak, G. Pietrzyński, Ł. Wyrzykowski, O. Szewczyk, and K. Ulaczyk. The Optical Gravitational Lensing Experiment. The OGLE-III Catalog of Variable Stars. VII. Classical Cepheids in the Small Magellanic Cloud. *ACTAA*, 60:17–39, March 2010.

R. F. Stellingwerf. Period determination using phase dispersion minimization. *ApJ*, 224:953–960, Sep 1978. doi: 10.1086/156444.

P. B. Stetson, V. F. Braga, M. Dall'Ora, G. Bono, R. Buonanno, I. Ferraro, G. Iannicola, M. Marengo, and J. Neeley. Optical and Near-Infrared UBVRIJHK Photometry for the RR Lyrae Stars in the Nearby Globular Cluster M4 (NGC 6121). *Publications of the Astronomical Society of the Pacific*, 126:521, June 2014. doi: 10.1086/677195.

Peter B. Stetson. DAOPHOT: A Computer Program for Crowded-Field Stellar Photometry. *Publications of the Astronomical Society of the Pacific*, 99:191, March 1987. doi: 10.1086/131977.

J. Storm, W. Gieren, P. Fouqué, T. G. Barnes, I. Soszyński, G. Pietrzyński, N. Nardetto, and D. Queloz. Calibrating the Cepheid period-luminosity relation from the infrared surface brightness technique. II. The effect of metallicity and the distance to the LMC. *A&A*, 534:A95, October 2011. doi: 10.1051/0004-6361/201117154.

K. Sziládi, J. Vinkó, E. Poretti, L. Szabados, and M. Kun. New homogeneous iron abundances of double-mode Cepheids from high-resolution echelle spectroscopy. *A&A*, 473(2):579–587, Oct 2007. doi: 10.1051/0004-6361:20077539.

The $Planck$ Collaboration. The Scientific Programme of Planck. *arXiv e-prints*, art. astro-ph/0604069, Apr 2006.

Glenn P. Tiede, Ata Sarajedini, and Michael K. Barker. The Stellar Populations in the Outer Regions of M33. I. Metallicity Distribution Function. *AJ*, 128(1):224–236, Jul 2004. doi: 10.1086/421369.

John Tonry and Donald P. Schneider. A New Technique for Measuring Extragalactic Distances. *AJ*, 96:807, September 1988. doi: 10.1086/114847.

R. B. Tully and J. R. Fisher. A new method of determining distances to galaxies. *A&A*, 500:105–117, June 2009.

A. Udalski, M. K. Szymański, and G. Szymański. OGLE-IV: Fourth Phase of the Optical Gravitational Lensing Experiment. *ACTAA*, 65(1):1–38, March 2015.

M. A. Urbaneja, A. Herrero, R. P. Kudritzki, F. Najarro, S. J. Smartt, J. Puls, D. J. Lennon, and L. J. Corral. Blue Luminous Stars in Nearby Galaxies: Quantitative Spectral Analysis of M33 B-Type Supergiant Stars. *ApJ*, 635(1):311–335, Dec 2005. doi: 10.1086/497528.

K. Viironen, G. Delgado-Inglada, A. Mampaso, L. Magrini, and R. L. M. Corradi. The S2N2 metallicity calibrator and the abundance gradient of M33. *MNRAS*, 381(4): 1719–1726, Nov 2007. doi: 10.1111/j.1365-2966.2007.12357.x.

Douglas L. Welch and Peter B. Stetson. Robust Variable Star Detection Techniques Suitable for Automated searches: New Results for NGC 1866. *AJ*, 105:1813, May 1993. doi: 10.1086/116556.

Douglas L. Welch, Mario Mateo, Patrick Cote, Philippe Fischer, and Barry F. Madore. The Variable Stars of NGC 1866. *AJ*, 101:490, Feb 1991. doi: 10.1086/115700.

A. J. Wesselink. The observations of brightness, colour and radial velocity of δ Cephei and the pulsation hypothesis (Errata: 10 258, 310). *Bulletin of the Astronomical Institutes of the Netherlands*, 10:91, January 1946.

S. P. Willner and K. Nelson-Patel. Neon Abundances in the H II Regions of M33. *ApJ*, 568(2):679–688, Apr 2002. doi: 10.1086/339032.

Dennis Zaritsky, Jr. Kennicutt, Robert C., and John P. Huchra. H II Regions and the Abundance Properties of Spiral Galaxies. *ApJ*, 420:87, January 1994. doi: 10.1086/173544.

Ya. B. Zeldovich and R. A. Sunyaev. The Interaction of Matter and Radiation in a Hot-Model Universe. *Ap&SS*, 4:301–316, July 1969. doi: 10.1007/BF00661821.